공학박사 학위논문

Numerical Investigation and Surrogate Modeling of Aerodynamic Jet Interaction for Continuous Type Side-Jet Controlled Rocket

연속형 측추력기를 사용하는 로켓의 공력 제트 간섭력 수치분석 및 대체 모델링

2017 년 8 월

서울대학교 대학원

기계항공공학부

강 경 태

Abstract

Numerical Investigation and Surrogate Modeling of Aerodynamic Jet Interaction for Continuous Type Side-Jet Controlled Rocket

Kang Kyoung Tai

Department of Aerospace Engineering

The Graduate School

Seoul National University

The supersonic jet interaction generated by a continuous type side-jet thruster of the missile was considered. Firstly, the jet interaction flow field was investigated using numerical simulations. The simulation was made use of the three-dimensional unstructured-based computational fluid dynamics (CFD) solver. The numerical simulation method was validated through comparison with wind tunnel test results. Flow fields investigation and jet interaction effects for various flow conditions, jet magnitude, and jet direction conditions were performed. Secondly, the jet interaction aerodynamic database based on CFD data was developed and assessed. The generation of the jet interaction aerodynamic database for the continuous type side-jet requires a large amount of simulation data owing to the complex nature of jet interaction. To reduce the required

number of simulations, seven jet operating conditions were selected using geometrical symmetry at first; then, three-dimensional numerical simulations were conducted to build the jet interaction aerodynamic database in the reduced design space. Two modeling approaches were used in developing the jet interaction aerodynamic database. One is CFD-based modeling with a full factorial sampling, and the other is surrogate modeling, based on the Latin hypercube sampling and Kriging method, for the interim database. The resulting two aerodynamic databases were assessed through comparison with flight test results. Based on the comparison, both models showed a suitable representation of the aerodynamic coefficients within 10% error during the jet operation period. This assessment confirms that the jet interaction aerodynamic database for missiles with continuous type side-jet thrusters can be constructed using the CFD-based modeling approach. The surrogate model was found to perform well compared with the CFD-based model within an acceptable error level.

Keywords: side-jet, continuous type side-jet, jet controlled missile, aerodynamic database, aerodynamic coefficients, jet interaction, CFD, surrogate modeling

Student Number: 2012-30166

Contents

List of Tables

List of Figures

Chapter 1

Introduction

1.1 Research Background

1.1.1 Side-jet control of missile

Modern guided missiles that require target interception ability often use a side-jet thruster as a control device to enhance maneuverability within a short time because of its fast response time characteristics compared to the conventional aerodynamic control devices. Generally, the side-jet control is effective in the low dynamic pressure region, such as the launch phase, and the terminal guidance phase at high altitude above the stratosphere. But it is also applicable to high maneuvering missiles operating in low atmosphere regions to enhance the maneuverability and response of aerodynamic control.

Despite these advantages, there is one major disadvantage in applying the side-jet control: the jet interaction effect associated with the jet control system. When the side-jet controller is operating in endo-atmospheric flight, there is a strong aerodynamic jet interaction between the jet flow and free-stream. This strong interaction creates interference forces and moments acting on the missile frame. Thus, the total force is a combination of the thrust force

Figure 1.1: Schlieren photograph of side-jet interaction flow field

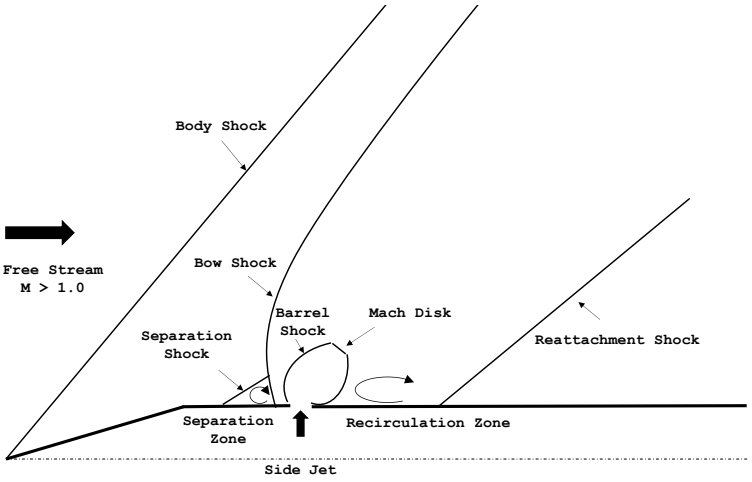

Figure 1.2: Schematics of side-jet interaction

and the jet interaction force. The schlieren image and a flow field schematic of a typical side-jet control is shown in Fig. 1.1 and Fig 1.2. The jet plume, which causes a strong bow shock, acts as an obstacle to the external flow. An adverse pressure gradient upstream of the jet generates a separation of the

boundary layer and separation shock. The surface pressure at this region is higher than ambient pressure. An expanded and separated axial flow by the jet plume forms a recirculation region behind the jet that causes a low-pressure region on the surface. These integrated high and low pressure regions generate jet interaction forces and moments [1, 2]. The forces induced by aerodynamic interference could frequently be acting in different directions from that of the jet reaction force. Therefore, an accurate estimation of the jet interaction effect is critical in developing a reliable design for precise control of missile with a side-jet thruster. For this purpose, a six-degrees-of-freedom (6-DOF) jet interaction aerodynamic database should be constructed during the system development.

1.1.2 Continuous type side-jet

Two types of side-jet control of missile can be considered according to their control method, the moment control type and the force control type. For moment control, the side-jet thruster is located in ahead of or in rear of the center of gravity(c.g.) arising force and moment in the pitch axis. The later type has the side-jet thruster that is located near the c.g. arising the acceleration directly. The moment control type widely uses the multiple small impulse type jet thruster similar to PAC-3. The longer duration continuous type jet similar to SM-3 or terminal high altitude area defense (THAAD) is suitable for the force control type [3, 4].

The continuous type side-jet control is performed using four nozzles which are located in diametrically opposite directions in two orthogonal planes. Each nozzle has its own switching device to control nozzle thrust. The combinations of the switching units of the nozzles enable thrust vectoring. This type of

side-jet control ensures omni-directional control with short response time and large reaction control forces. Jet interaction of the continuous side-jet thruster is considered in this research. The jet interaction mechanism of the continuous type side-jet thruster is the same as for the conventional side-jet thruster, as explained previously. However the continuous type side-jet controller has a bigger jet nozzle than the conventional side-jet thruster and causes a more complex aerodynamic jet interaction between the side-jet and the supersonic free-stream, due to the operation of multiple nozzles. So, the aerodynamic interference database has to be more complicated.

1.1.3 Jet interaction aerodynamic database

The 6-DOF aerodynamic database of the vehicle is required in developing the missile system for mission simulation and analysis. The main objective of constructing the database is to provide aerodynamic data to the development of the guidance, navigation, and control systems for the vehicle [5]. For the continuous type side-jet thruster controlled missile, jet interaction aerodynamic database should also be constructed for precise jet control. Traditionally, the aerodynamic databases for stability and control analysis over the flight are filled by usage of look-up tables from wind tunnel test campaigns [5–7]. Constructing aerodynamic database of jet interaction with a wind tunnel test is difficult because of difficulties in achieving similitude between a wind tunnel test and actual flight conditions and because of requiring large amount of data to cover all operating ranges. So aerodynamic database of jet interaction was developed by using an unstructured based CFD (Computational Fluid Dynamics) simulation results in this study. The numerical simulation method was validated

through the comparison with limited wind tunnel test results for the validation. The resulting aerodynamic database was assessed through the comparison to flight test results.

1.2 Literature Review and Scope of Works

Through extensive research over the last 50 years, analytical and computational analysis, as well as wind tunnel and flight test, has been done associated with these aerodynamic interference effects. The understanding of the phenomena that occur with respect to the reaction control of missiles has matured [1,2]. But it is still difficult to predict precisely the aerodynamic jet interferences in order to evaluate jet thruster effectiveness, because of the difficulties in achieving similitude between a wind tunnel test and actual flight conditions [8–11]. With the advances in CFD technology and high performance computing, the CFD technique has come to play an important part in predicting jet interferences of lateral jets. In the last few decades, many research showed the capability of CFD simulation in the prediction of jet interaction phenomena [11–15]. Chamberlain et al. [16] reported the success achieved in the design and testing of a THAAD interceptor through extensive utilization of CFD for the jet interaction problem [16]. However, most studies have been confined to impulse type small single side-jet applications. Study of the continuous type side-jet has not been published and the construction of a jet interaction database using only CFD simulation data has not been reported.

In this study, a numerical investigation of the jet interference effects for a missile equipped with a continuous type side-jet thruster is presented. Three-

dimensional flow fields are simulated by using an unstructured-based CFD solver. The accuracy of the applied numerical method was evaluated by comparison with wind tunnel test results. Flow field investigation with respect to the jet interaction parameters was conducted for various flow conditions, jet pressure ratios and jet direction conditions.

With the understanding of jet interaction phenomena of the continuous type side-jet through the numerical investigation, the jet interaction aerodynamic database was constructed based on numerical simulations. The development process of the jet interaction aerodynamic database based on computational results and its system level assessment are presented in this study. The primary focus of this study is on building the jet interaction aerodynamic database of the continuous type side-jet using CFD data efficiently with minimum computational cost. First, seven jet conditions were selected to reduce the number of simulations in building the aerodynamic database. Then, extensive CFD simulations of jet interaction flow field for the continuous type side-jet controlled missile were conducted in the reduced design space, and a CFD-based modeling with the full factorial sampling was applied to develop the jet interaction aerodynamic database.

Although the CFD-based modeling can provide the jet interaction database efficiently within sufficient accuracy, there is a gap between the initial design stage and the delivery time in the system development cycle because of its high computational cost. To bridge this gap, a surrogate modeling approach was applied to supply an interim approximated database. Surrogate modeling is increasingly being used to construct the CFD database in the aerospace community, due to its ability to reduce the resource requirements for design explo-

ration [17–19]. With effective sampling and interpolation methods, a surrogate model can reduce the number of simulations required to construct the aerodynamic database to a specified accuracy. In this study, the Latin hypercube sampling (LHS) method was used to sample the training data, and the Kriging method was selected as an approximation model for the surrogate modeling. The resulting two aerodynamic databases were evaluated through comparison with flight test results.

1.3 Objective of Research

The objective of the present study is two-fold: one is to investigate jet interaction phenomena of continuous type side-jet with numerical approach. The unstructured grids based Reynolds–Averaged Navier–Stokes (RANS) solver is used for the simulation and extensive validations are presented to show the accuracy of applied methods. The other one is to efficiently construct jet interaction aerodynamic database of continuous type side-jet using CFD data. The CFD-based modeling with a full factorial sampling and the surrogate modeling approach are used in developing the jet interaction aerodynamic database. The both models are assessed through the comparison with the flight test results.

1.4 Outline

The rest of present thesis is organized as follows.

In chapter 2, the applied numerical methods for jet interaction analysis will be introduced. The unstructured grids based Reynolds–Averaged Navier–Stokes (RANS) compressible solver and discretization methods are described.

In chapter 3, the continuous type side-jet controlled missile system is introduced and numerical investigation is carried out. This chapter includes detailed flow features of jet interaction and jet interaction characteristics according to change in jet interaction parameter. The validation of numerical results with wind tunnel test result also will be presented.

In chapter 4, the development process of the jet interaction aerodynamic database based on computational results is presented. The detailed surrogate modeling methods and its evaluation are described.

In chapter 5, the assessment of constructed jet interaction databases through post-flight test analysis is presented. Applied post-flight test method is introduced and analysis results are presented.

Finally, conclusion and future works are given in Chapter 6.

Chapter 2

Numerical Method

For the simulation of supersonic jet flow, the unstructured grids based Reynolds–Averaged Navier–Stokes (RANS) compressible solver was employed. The solver is based on a cell vertex centered finite volume technique to solve the governing equations. The control volumes are formed by a median-dual grid obtained from the control surfaces for each edge. This chapter describes applied discretization method and turbulence model for turbulence closure.

2.1 Governing Equations

The compressible Reynolds–Averaged Navier–Stokes (RANS) equations written in a Cartesian frame of reference [20], can be expressed as

$$\frac{\partial \boldsymbol{U}}{\partial t} + \nabla \cdot \boldsymbol{F_c} - \nabla \cdot \boldsymbol{F_v} = \boldsymbol{Q} \tag{2.1}$$

where $\boldsymbol{U} = (\rho, \rho u_1, \rho u_2, \rho u_3, \rho E)^T$ is the conservative variables, $\boldsymbol{F_c}$ and $\boldsymbol{F_v}$ are respectively the convective and viscous flux matrices and $\boldsymbol{Q}$ is the source term. On integrated form for a control volume Ω, the same equations become

$$\int_\Omega \frac{\partial \boldsymbol{U}}{\partial t} d\Omega + \oint_{\partial\Omega} (\boldsymbol{F_c} - \boldsymbol{F_v}) dS = \int_\Omega \boldsymbol{Q} d\Omega \tag{2.2}$$

Then, the time derivative of the conservative variables can be cast in the form

$$\int_{\Omega} \frac{\partial \boldsymbol{U}}{\partial t} d\Omega = \Omega \frac{\partial \boldsymbol{U}}{\partial t} \tag{2.3}$$

Herewith, Eq. 2.2 becomes

$$\frac{\partial \boldsymbol{U}}{\partial t} = -\frac{1}{\Omega} \left[\oint_{\partial\Omega} (\boldsymbol{F_c} - \boldsymbol{F_v}) dS - \int_{\Omega} \boldsymbol{Q} d\Omega \right] \tag{2.4}$$

The surface integral on the right-hand side of Eq. 2.4 is approximated by a sum of the fluxes passing through the faces of the control volume. If we consider a particular volume Ω_I, we obtain the following equation.

$$\frac{d\boldsymbol{U}}{dt} = -\frac{1}{\Omega_I} \left[\sum_{m=1}^{N_F} (\boldsymbol{F_c} - \boldsymbol{F_v})_m \Delta S_m - (\boldsymbol{Q}\Omega)_I \right] \tag{2.5}$$

In the above equation, N_F denotes the number of the faces of the control volume Ω_I, and the variable ΔS_m stands for the area of the face m, respectively. The flux matrices resolve into Cartesian components

$$\begin{aligned} \boldsymbol{F_c} &= f_{c_1} n_x + f_{c_2} n_y + f_{c_3} n_z, \\ \boldsymbol{F_v} &= f_{v_1} n_x + f_{v_2} n_y + f_{v_3} n_z, \end{aligned} \tag{2.6}$$

where

$$f_{c_i} = \begin{pmatrix} \rho u_i \\ p\delta_{1i} + \rho u_i u_1 \\ p\delta_{2i} + \rho u_i u_2 \\ p\delta_{3i} + \rho u_i u_3 \\ \rho H u_i \end{pmatrix}, \quad f_{v_i} = \begin{pmatrix} 0 \\ \tau_{i1} \\ \tau_{i2} \\ \tau_{i3} \\ q_i + u_j \tau_{ij} \end{pmatrix} \tag{2.7}$$

and where the shorthand notation, i, is used to denote derivatives with respect to x_i. The stress tensor τ can be written as

$$\tau_{ij} = \mu \left[\frac{\partial u_i}{\partial x_j} + \frac{\partial u_j}{\partial x_i} - \frac{2}{3} (\nabla u) \delta_{ij} \right] \tag{2.8}$$

where μ is the dynamic viscosity and the heat flux q_i is written as

$$q_i = k\frac{\partial T}{\partial x_i}. \tag{2.9}$$

The thermal conductivity is given by

$$k = c_p\frac{\mu}{Pr} \tag{2.10}$$

where μ is the viscosity and Pr is the constant Prandtl number ($Pr = 0.72$ for air). The total energy per unit mass E of a fluid is obtained by adding its internal energy per unit mass, e, to its kinetic energy $|\bar{u}|^2/2$

$$E = e + \frac{|\bar{u}|^2}{2} \tag{2.11}$$

The total enthalpy is can be expressed with the total energy and the pressure

$$H = h + \frac{|\bar{u}|^2}{2} = E + \frac{p}{\rho} \tag{2.12}$$

2.2 Gas Modeling

Two different gas models were used to simulate jet interaction flow.

2.2.1 Calorically perfect gas

Assuming that the working fluid behaves like a calorically perfect gas, the equation of state assumes the form

$$p = \rho RT \tag{2.13}$$

where R denotes the specific gas constant for the perfect gas. The enthalpy and the internal energy can be defined as

$$h = c_pT, \quad e = c_vT \tag{2.14}$$

The ratio of specific heats γ is the ratio of the heat capacity at constant pressure c_p to heat capacity at constant volume c_v as following

$$\gamma = \frac{c_p}{c_v}. \tag{2.15}$$

When the gas is the calorically perfect the internal energy of the gas is proportional to the temperature and thus the ratio of specific heat, γ, is constant. The relation between R and c_p is given by

$$R = \frac{\gamma - 1}{\gamma} c_p. \tag{2.16}$$

The static pressure is obtained from the conservative variables through the following relation

$$p = (\gamma - 1)\rho \left[E - \frac{|\bar{u}|^2}{2} \right]. \tag{2.17}$$

2.2.2 Thermally perfect gas, Multiple gases

In order to simulate the behavior of the mixing of several thermally perfect gases, the Navier-Stokes equations have to be augmented by $(N-1)$ additional transport equations for the N species [21]. The equation is solved for each gas and its fraction of the total density, its mass fraction specie Y_i, $0 \leq Y_i \leq 1$. These equations, formulated in the form of equation Eq. 2.5, look like:

$$\int_\Omega \frac{\partial \rho Y_i}{\partial t} d\Omega + \sum (\rho Y_i u \cdot n) \Delta S + \sum (\mu/\sigma) \frac{\partial Y_i}{\partial n} \Delta S = 0 \tag{2.18}$$

where σ is the Schmidt number. The total density will satisfy

$$\sum_{i=1}^{N} Y_i \rho_i = \rho \tag{2.19}$$

The internal energy and the effective gas constant are mass fraction weighted sums

$$e(T) = \sum_{i}^{N} Y_i e_i(T), \quad R(T) = \sum_{i}^{N} Y_i R_i(T) \tag{2.20}$$

2.3 Spatial Discretization

The finite volume discretization is obtained by applying the integral formulation of the governing equations in Eq. 2.1 to the control volume surrounding the unknown at node

$$\frac{\partial}{\partial t}(U_0 \mathcal{V}_0) + \sum_{k=1}^{m_0} F_{c_{0k}} n_{0k} S_{0k} + \sum_{k=1}^{m_0} F_{v_{0k}} n_{0k} S_{0k} = Q_0 \mathcal{V}_0, \tag{2.21}$$

where m_0 is the number of neighbors to node ν_0 [20, 22]. The surfaces S_{0k} enclose the control volume for node ν_0 and form the dual grid illustrated in Fig. 2.1 in 2D for a given triangulation. The convective flux vectors $F_{c_{0k}}$ and viscous flux vector $F_{v_{0k}}$ are computed on the face consisting of nodes ν_0 and ν_k where S_{0k} is given, the source term Q_0 is computed directly at the node.

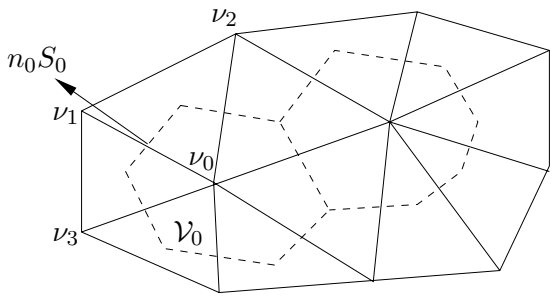

Figure 2.1: The median dual grid in 2D [22]

2.3.1 Convective fluxes

The convective flux $F_{c_{0k}}$ calculated with the flux difference splitting scheme of Roe on unstructured grid [23].

Upwind Schemes

The Roe's flux difference splitting scheme is adopted. The flux difference splitting schemes evaluate the convective fluxes at the face of the control volume from the left and right state by solving the Riemann problem which was introduced by Godunov [24]. In order to reduce the computational costs of Godunov scheme, Roe's method is applied. Roe's upwind scheme is based on the decomposition of the flux difference over a face of the control volume into a sum of wave contributions. The convective fluxes are evaluated at the faces of a control volume faces according to the formula

$$F_{c_{01}} = \frac{1}{2}\left[(F_c(U_1) + F_c(U_0)) - |\tilde{A}_{Roe}|\,(U_1 - U_0)\right]. \tag{2.22}$$

In the above equation Eq. 2.22, $\tilde{A}_{Roe}$ denotes the Roe matrix which is computed as

$$\tilde{A}_{Roe} = \frac{1}{2}R\tilde{\Lambda}R^{-1}\,(U_1 - U_0) = \frac{1}{2}R\tilde{\Lambda}L^{-1}\,(V_1 - V_0) = \frac{1}{2}R\tilde{\Lambda}dW_{01}, \tag{2.23}$$

where U and V denote the conservative and the primitive variables respectively. The characteristic variables are denoted by $dW_{01} = L^{-1}(V_1 - V_0) = R^{-1}(U_1 - U_0)$. The tensor R is the right eigenvector matrix to the flux Jacobian,

$$\frac{\partial F_c}{\partial q} = R\Lambda R^{-1}, \tag{2.24}$$

where the diagonal tensor Λ contains the eigenvalues. A similar expression can be obtained for the tensor L belonging to the primitive variables.

The diagonal matrix $\tilde{\Lambda}$ is obtained as

$$\tilde{\Lambda} = |\Lambda^*|(I - \Psi), \tag{2.25}$$

where Ψ is a diagonal matrix with limiters for second order accuracy. For a Roe flux difference splitting scheme the components of R, L, Λ must be computed from the Roe averaged variables

$$\begin{aligned} \rho_{01} &= \sqrt{\rho_0}\sqrt{\rho_1}, \\ u_{01} &= \frac{u_0\sqrt{\rho_0} + u_1\sqrt{\rho_1}}{\sqrt{\rho_0} + \sqrt{\rho_1}}, \\ H_{01} &= \frac{H_0\sqrt{\rho_0} + H_1\sqrt{\rho_1}}{\sqrt{\rho_0} + \sqrt{\rho_1}}, \\ c_{01}^2 &= (\gamma - 1)\left[H_{01} - |u_{01}|^2/2\right]. \end{aligned} \tag{2.26}$$

The diagonal matrix Λ^* in Eq. 2.25 contains the eigenvalues adjusted with an entropy fix to prevent the eigenvalues to become zero and produce unphysical solutions. The following Harten's entropy fix is used for each of the eigenvalues

$$|\lambda_i|^* = \begin{cases} \dfrac{\lambda_i^2 + \delta^2}{2\delta}, & \text{if} \quad |\lambda_i| \leq \delta, \\ |\lambda_i|, & \text{if} \quad |\lambda_i| > \delta, \end{cases} \tag{2.27}$$

where δ is a small value, which can be conveniently set equal to some fraction of the local speed of sound [25, 26].

Solution reconstruction

To achieve second order accuracy of the convective flux calculation. Barth and Jespersen's [27] reconstruction method is employed. It is assumed that the

solution is piecewise linearly distributed over the control volume.

$$U_{face} = U_{vertex} + \nabla U_{vertex} \cdot \Delta r, \tag{2.28}$$

where ∇U is the gradient of U and Δr represents the distance vector.

Evaluation of the gradients

Gradients of all primitive variables are needed to compute the characteristics in the nodes. Here the Green-Gauss approach is applied. The gradient in a node is computed by evaluating the surface integral of the gradient theorem

$$\nabla v_0 \approx \frac{1}{\mathcal{V}_0} \oint_{\partial \mathcal{V}_0} vn\, S \equiv \frac{1}{\mathcal{V}_0} \sum_{k=1}^{m_0} \frac{1}{2}(v_k + v_0) n_{0k} S_{0k}, \tag{2.29}$$

where v denotes a component of the primitive variables. The node valued characteristics dW_0 and dW_1 are obtained as

$$\begin{aligned} dW_0 &= L_0(\nabla V_0 \cdot (x_1 - x_0)), \\ dW_1 &= L_1(\nabla V_1 \cdot (x_1 - x_0)), \end{aligned} \tag{2.30}$$

in addition to the face value dW_{01} in Eq. 2.23.

The minmod limiter is applied and the limiter is computed according to the sign of the eigenvalues of the flux Jacobian,

$$\psi\, dw_{01} = \begin{cases} \text{minmod}(dw_0, dw_{01}), & \lambda_i \geq 0, \\ \text{minmod}(dw_{01}, dw_1), & \lambda_i < 0. \end{cases} \tag{2.31}$$

2.3.2 Viscous fluxes

In order to evaluate the viscous flux $F_{v_{0k}}$ in Eq. 2.21 compact discretization of the fully viscous approximation is used.

The viscous stresses for the momentum equations can be divided as

$$\tau_{ij} n_j = (\tau_{ij} n_j)_{\mathrm{tl}} + (\tau_{ij} n_j)_{\tan}, \tag{2.32}$$

where $(\tau_{ij} n_j)_{\mathrm{tl}}$ contains only normal derivatives and leads to a thin-layer discretization if only this term is considered. A fully viscous approximation is obtained if also the remaining part of the viscous terms $(\tau_{ij} n_j)_{\tan}$ are added. The components of the normal are here denoted $n = (n_x, n_y, n_z) = (n_1, n_2, n_3)$. The thin-layer part can then be formulated as,

$$(\tau_{ij} n_j)_{\mathrm{tl}} = \mu \left(\frac{\partial u_i}{\partial n} + \frac{1}{3} \left(\frac{\partial u_j}{\partial n} n_j \right) n_i \right). \tag{2.33}$$

The normal derivatives in Eq. 2.33 can be approximated on the edges as

$$\frac{\partial \varphi_{01}}{\partial n} = \frac{\varphi_1 - \varphi_0}{|x_1 - x_0|}, \tag{2.34}$$

with the notation from Fig. 2.1 and where the normal is directed from node ν_0 to node ν_1. With this formulation only two points are involved in computing the normal gradients at the edges and hence automatically leads to a compact second derivative.

By recalling the identity of the Laplace's equation

$$\int_\Omega \Delta\phi \, dV = \oint_{\partial\Omega} \frac{\partial \phi}{\partial n} \, dS, \tag{2.35}$$

the following approximation of the Laplace's equation at node is ν_0 obtained as

$$\Delta\varphi_0 \approx \frac{1}{\mathcal{V}_0} \sum_{k=1}^{m_0} S_{0k} \frac{\varphi_k - \varphi_0}{|x_k - x_0|}. \tag{2.36}$$

The remaining parts of the viscous terms contain gradients which may be added using the Green–Gauss formulation in Eq. 2.29 and thus a fully viscous approach can be obtained.

2.4 Temporal Discretization

The iterative scheme used to converge the discrete residuals to zero is an explicit q-stage Runge–Kutta scheme [28]. The equation

$$\mathcal{V}\frac{dU}{dt} = R(U), \tag{2.37}$$

can be written

$$\begin{aligned} u^1 &= u^n + \alpha_1 \Delta t \mathcal{V}^{-1} R(u^n), \\ u^2 &= u^n + \alpha_2 \Delta t \mathcal{V}^{-1} R(u^1), \\ &... \\ u^q &= u^n + \Delta t \mathcal{V}^{-1} R(u^{q-1}), \\ u^{n+1} &= u^q. \end{aligned} \tag{2.38}$$

The α_i represents the stage coefficients which codetermine the stability area and the order of accuracy of the Runge–Kutta scheme. They can be chosen in such a way that they suit the problem to be solved.

The local time step is computed for each node ν_0 according to

$$\Delta t_0 = \min\left(\mathrm{CFL}_{invicid}\frac{\mathcal{V}_0}{\lambda_0}, \mathrm{CFL}_{viscous}\frac{\mathcal{V}_0}{\lambda_{V_0}}\right), \tag{2.39}$$

where $\mathcal{V}_0$ is the volume, λ_0 is the integrated convective spectral radius and λ_{V_0} is corresponding viscous spectral radius.

2.5 Turbulence Modeling

The $k-\omega$ Shear Stress Transport (SST) turbulence model of Menter [29, 30] is applied for the turbulence closure. The SST model seeks to combine the positive features of the $k-\epsilon$ model and the $k-\omega$ model of Wilcox [31]. It

is well known that the $k-\omega$ SST model is superior to the $k-\epsilon$ approach in adverse pressure flows and in compressible flows.

The $k-\omega$ SST model is given by the following formulations. The transport equations for the turbulent kinetic energy and the specific dissipation of turbulence read in differential form

$$\begin{aligned}\frac{\partial \rho k}{\partial t}+\frac{\partial(\rho v_j k)}{\partial x_j} &= \frac{\partial}{\partial x_j}\left[(\mu+\sigma_k\mu_t)\frac{\partial k}{\partial x_j}\right]+\tau_{ij}^F S_{ij}-\beta^*\rho\omega k,\\ \frac{\partial \rho\omega}{\partial t}+\frac{\partial(\rho v_j \omega)}{\partial x_j} &= \frac{\partial}{\partial x_j}\left[(\mu+\sigma_\omega\mu_t)\frac{\partial \omega}{\partial x_j}\right]+\frac{C_\omega\rho}{\mu_t}\tau_{ij}^F S_{ij}\\ &\quad -\beta\rho\omega^2+2(1-f_1)\frac{\rho\sigma_{\omega 2}}{\omega}\frac{\partial k}{\partial x_j}\frac{\partial \omega}{\partial x_j}.\end{aligned} \tag{2.40}$$

The right-hand side terms in Eq. 2.40 represent conservative diffusion, eddy-viscosity production and dissipation. The last term in ω-equation describes the cross diffusion. The turbulent eddy viscosity is computed from

$$\mu_t=\frac{\rho a_1 k}{\max(a_1\omega,\Omega f_2)}. \tag{2.41}$$

Each of constants is blended of an inner (1) and outer (2) constant

$$\phi=f_1\phi_1+(1-f_1)\phi_2, \tag{2.42}$$

where ϕ_1 is constant 1 and ϕ_2 represents constant 2. Additional functions are given by:

$$\begin{aligned} f_1 &= tanh(arg_1^4),\\ arg_1 &= \min\left[\max\left(\frac{\sqrt{k}}{\beta^*\omega d}.\frac{500\mu}{\rho\omega d^2}\right),\frac{4\rho\sigma_{\omega 2}k}{CD_{k\omega}d^2}\right],\\ CD_{k\omega} &= \max\left(2\frac{\rho\sigma_{\omega 2}}{\omega}\frac{\partial k}{\partial x_j}\frac{\partial \omega}{\partial x_j},10^{-20}\right),\\ f_2 &= tanh(arg_2^2),\\ arg_2 &= \max\left(\frac{2\sqrt{k}}{\beta^*\omega d},\frac{500\mu}{\rho\omega d^2}\right).\end{aligned} \tag{2.43}$$

The coefficients are given by:

$$\begin{aligned}
\sigma_{k1} = 0.85, \quad \sigma_{\omega 1} = 0.5, \quad \beta_1 = 0.075, \\
C_{\omega 1} = \beta_1/\beta^* - \sigma_{\omega 1} k^2/\sqrt{\beta^*} = 0.533, \\
\sigma_{k2} = 1.0, \quad \sigma_{\omega 2} = 0.856, \quad \beta_2 = 0.0828, \\
C_{\omega 2} = \beta_2/\beta^* - \sigma_{\omega 2} k^2/\sqrt{\beta^*} = 0.440, \\
\beta^* = 0.09, \quad k = 0.41, \quad a_1 = 0.31.
\end{aligned} \tag{2.44}$$

Chapter 3

Numerical Investigation of Continuous Type side-jet

3.1 Configuration and Computational Grid

Numerical simulation of jet interaction has been conducted for continuous type side-jet controlled missile. Detailed configuration of missile system is presented in Fig. 3.1 which consists of ogive nose, canard, side-jet thruster and tail. The missile uses four canard surfaces to provide integrated control forces in normal flight state. In final guidance state, the side-jet thruster is used to get additional steering forces. The length of missile is about 17 calibers(x/D) and side-jet thruster is located at 7 calibers from the nose.

The continuous type side-jet controller consists of four equally-spaced nozzles along the circumferential position. The nozzle shape is rectangular and each nozzle has the their own thrust control devices connected to solid propellant gas generator. They generate jet forces for the desired direction with the combination of four nozzles.

About 15 million tetrahedral mesh cells were constructed for the body-canard-tail configuration missile with side-jet, and 25 prism layers were used for near wall boundary calculation. Fine grids were used in the nose, control

surfaces and jet injection region to capture complex jet interaction flow fields. Fig. 3.2 shows constructed unstructured grid system around the missile. The rectangular-shaped nozzle configuration of the jet thruster was modeled from the throat region and the stagnation inlet boundary condition was applied with the jet chamber conditions.

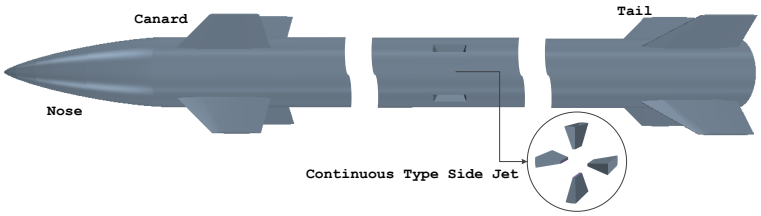

Figure 3.1: Configuration of missile with continuous type side-jet thruster

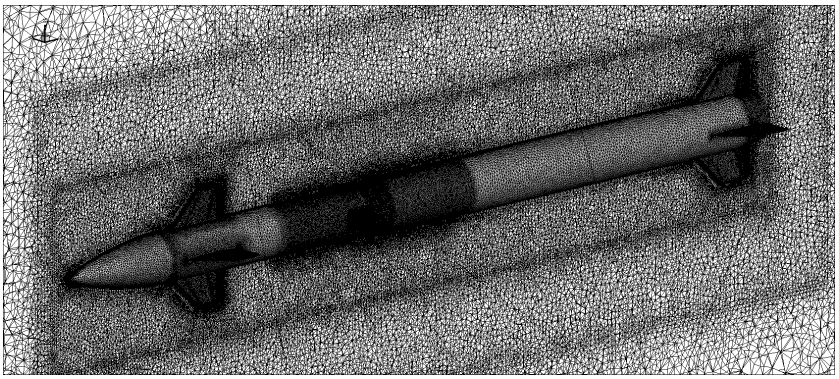

Figure 3.2: Constructed unstructured meshes around the vehicle

3.2 Jet Interaction Parameters and Evaluation

The principle objective in the analysis of jet interaction is to assess the aerodynamic forces induced by the jet. It is common to define the net control force and moment produced by jet control in terms of a parameter referred to as the amplification factor [32]. Two amplification factors are used. One is the force amplification factor K_F. The other is the moment amplification factor K_M. The amplification factors are defined as the ratio of total force and moment produced to the jet thrust. They are defined as

$$\begin{aligned} K_F &= (F_i + F_j)/F_j \\ K_M &= (M_i + M_j)/M_j \end{aligned} \tag{3.1}$$

where F_i and M_i are jet interaction force and moment respectively. The nozzle delivered thrust F_j is calculated as $F_j = F_v + (P_j - P_\infty)A_j$ and the moment induced by the jet thrust is defined as $M_j = F_j l_j$, where l_j is moment arm of nozzle thrust.

The jet amplification factors help understanding jet interaction effects intuitively and it can simply converted to physical values for the fixed jet thrust condition. But for the continuous type side-jet thruster, this approach is not practical. Because the jet thrust can be varying according to the nozzle combination and the jet interaction effect is exist even in the null thrust state. So the difference of aerodynamic coefficients with and without jet flow (Eq.3.2) is used to measure jet interaction effects.

$$\Delta C_{w_{JI}} = C_w(\text{with jet}) - C_w(\text{without jet}) \tag{3.2}$$

In general, the jet interaction effects of missile are function of many parameters including nozzle shape, jet location, jet thrust, missile attitude angle and

free-stream conditions. For the continuous type side-jet controller, the jet interaction effects are can be defined as a function of flight Mach number, altitude, angle of attack, roll angle of missile, magnitude of jet forces and desired jet direction as shown in Eq.3.3. Considering all operation regions of jet thruster, large amount of design spaces are exist in analyzing jet interaction effects. It also means that huge number of aerodynamic data are needed in modeling of jet interaction aerodynamic database.

$$\Delta C_{w_{JI}} = f(M_\infty, H, \alpha_t, \phi, |F|, \theta_j) \tag{3.3}$$

3.3 Jet Direction and Scale of Continuous Type Side-jet

The continuous type side-jet thruster consists of four equally-spaced nozzles along the circumferential position. Each nozzle has a switching device to alter nozzle thrust and a single solid propellant gas generator supplies compressed gas to the nozzle. It generates jet forces for the desired direction with the combination of four nozzles. Fig.3.3 shows the mechanism of thrust vectoring with continuous type side-jet and its possible operating thrust ranges according to the desired jet direction. The pressure of supplying chamber should be sustained constantly for safety reason during the operation. It means that the summation of nozzle thrusts cannot exceed the maximum thrust(T_{max}). Therefore, thrust of each nozzle($N1 \sim N4$) has the following relations in Eq.3.4 with desired thrust(F_d) and jet direction(θ_j). The resultant jet thrust scale can be

defined as normalized value by maximum thrust at each jet direction(Eq. 3.5).

$$
\begin{aligned}
N1 + N2 + N3 + N4 &= T_{max} \\
N1 - N3 &= F_d \times cos\theta_j \\
N2 - N4 &= F_d \times sin\theta_j
\end{aligned}
\tag{3.4}
$$

$$
|F| = F_d / F_{max} \tag{3.5}
$$

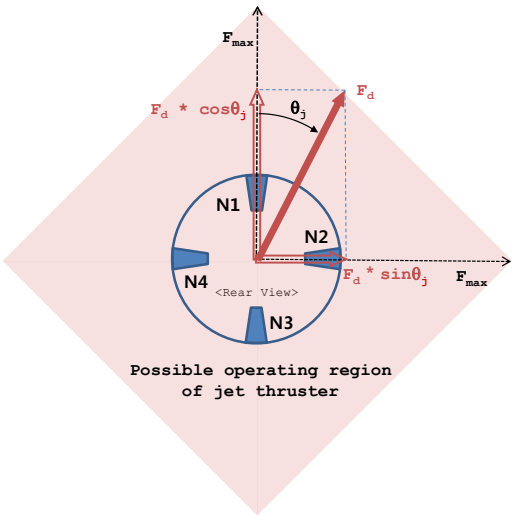

Figure 3.3: Thrust vectoring mechanism and possible operating region of continuous type side-jet

3.4 Simulation Conditions

The numerical method in Chap. 2 is applied for the simulation of continuous type side-jet. The jet gas is modeled as a lumped chemical mixture for the simulation. This implies that the simulation of the specific heat ratio γ_j of 1.24

is the same as the real gas; however, the chemical reaction effect of exhaust gases is not considered.

Considering the operation mechanism of the continuous type side-jet, four jet direction conditions are selected for the numerical simulation and its validation. The selected four jet directions are displayed in Fig. 3.4. The jet direction F0 means null state of zero thrust, the jet direction F1, F3, and F5 are full thrust state at jet direction $\theta_j = 0^o$, 22.5^o, and 45.0^o respectively. The simulation was carried out for theses jet direction conditions at various free-stream conditions. Two free-stream Mach numbers (3.0 and 3.6), angle of attack ranges from 0^o to 28^o and a missile roll angle ranges from 0^o to 360^o are considered.

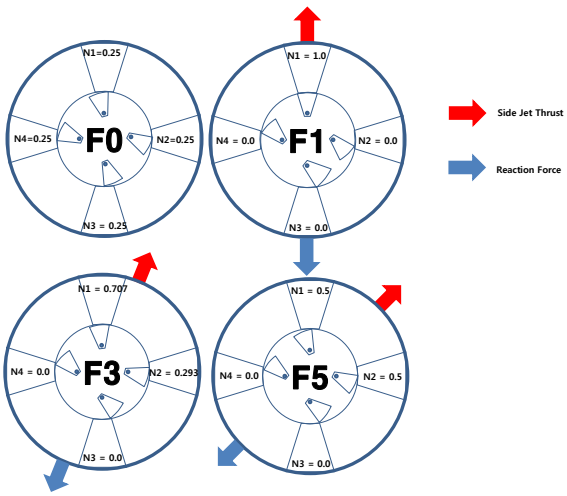

Figure 3.4: Selected jet directions for the simulation (Rear View)

3.5 Wind Tunnel Test and Validation of Numerical Method

Because the investigation and the development of aerodynamic database of jet interaction were conducted from CFD simulations, evaluation process of uncertainty between CFD results and physical results is needed. So, the wind tunnel test has been conducted on a sub-scale model representing a missile with continuous type side-jet in the wind tunnels. Test model was designed to simulate jet flow for four defined jet directions:F0, F1, F3, F5. Compressed air gas was supplied to the jet nozzle from reservoir for generating various chamber pressure conditions. Five components(Cy, Cz, Cl, Cm, Cn) balance was used to measure aerodynamic coefficients during the test. Jet interaction aerodynamic coefficients were obtained from differences between jet-on and jet-off tests.

For the validation of the numerical methods, additional CFD simulations were performed at the wind tunnel test conditions. All simulations for the investigation were conducted using the lumped hot gas model ($\gamma_j = 1.24$) for jet flow. The cold gas model ($\gamma_j = 1.4$) was used for the validation simulations at the wind tunnel test conditions.

3.5.1 Jet interaction similitude parameter

Test conditions were designed to simulate various flow conditions in the CFD simulation cases. But there is difficulties in simulating jet flow conditions in the wind tunnel with compressed air gas. In order to obtain identical aerodynamic coefficients for a wind tunnel model and its scaled up vehicle, the surface pressure coefficient (C_p) should be the same at each point on the body. For this

purpose two jet interaction scaling parameters are widely used. One is the pressure ratio and the other is the jet to free-stream momentum parameter ratio (MPR), as defined in Eq. 3.6 and Eq. 3.7.

$$\mathrm{PR} = \frac{P_j}{P_\infty} \tag{3.6}$$

$$\mathrm{MPR} = \frac{\gamma_j P_j M_j^2}{\gamma_\infty P_\infty M_\infty^2} \left(\frac{A_j}{A_b} \right) \tag{3.7}$$

R. Chamberlain [16] explained that the MPR, defined as the ratio of momentum flow out of the jet to the free-stream momentum flow, is the most important parameter to achieving similitude in jet interaction. Holding the MPR as constant ensures that the flow blockage due to the jet exhaust, the wrap-around shock strength, and the low pressure wake characteristics remain similar. So, MPR was selected as a simulation parameter to match actual flight conditions. Table 3.1 specifies the test MPR conditions corresponding Mach number and altitude.

Table 3.1: MPR conditions for wind tunnel test

Mach \ Altitude	H1	H2	H3
3.0	0.34	1.02	3.05
3.6	0.24	0.71	2.12

3.5.2 Jet-off cases

The jet interaction aerodynamic coefficients are obtained from the difference of aerodynamic coefficients with and without jet flow. Therefore, the accuracy of the numerical simulation for jet-off cases was evaluated at first. Figures 3.5 – 3.7 show comparison of the experimental and the simulation data for jet-off state at M = 3.0 and $\phi = 0^o - 45^o$. Each aerodynamic coefficient is normalized to the maximum values of each coefficient in the wind tunnel test. The predicted aerodynamic coefficients at the roll angle of 0 degree are in good agreement with the experimental value, and it can be seen that the error increases as the roll angle increases. The largest difference is 5% in pitching moment at the roll angle 45 degrees, which, in addition to being well within wind tunnel uncertainties, is not a significant error range.

3.5.3 Jet-on cases

The axial distribution of pressure coefficients from the simulation is compared with the experimental value in Fig. 3.8 – 3.12. In the wind tunnel test, the longitudinal pressure distribution was measured only along nozzle N1, so the pressure distribution along the centerline of nozzle N1 was compared for various missile roll angle and jet direction conditions. A very satisfactory match between the computational and experimental values is obtained. It is shown that the simulation captures well the shock induced separation points and the recirculation regions. The features of the longitudinal profiles are typical: 1) a rise in pressure in ahead of the jet nozzle where the separation shock (λ shock) forms owing to the boundary layer separation; 2) a second higher pressure rise

indicating the main jet bow shock; 3) the nozzle exit pressure is off-scale; and 4) a low pressure region behind the jet that asymptotes toward the jet-off case pressure far downstream of the nozzle [33].

The typical jet interaction force and moment coefficients are compared with numerical simulation results in Fig. 3.13, where the jet interaction effects versus MPR at $M = 3.0$, $\alpha_t = 0°$, $\phi = 0°$, and jet direction index F1 are displayed. The error bar of the wind tunnel test data in the figure shows the uncertainties of measurements. The jet interaction normal force and moment coefficients of the simulations are in agreement with the experimental data with less than 8% error range at MPR = 3.05. The jet interaction effects for hot gas and cold gas simulation results show the same behavior along the MPR change and the difference is relatively small. The result shows that the MPR is a suitable similitude parameter to describe jet interaction effects. This is consistent with a previous study that reported the requirement of constant MPR during scaling attempts to ensure similar jet flow characteristics [16].

Figures 3.14 and 3.15 show a comparison of jet interaction normal force and pitching moment response surfaces between cold gas CFD simulations results and wind tunnel test data at $M = 3.0$ and MPR = 1.02. The trends of the overall jet interaction with respect to the change of angle of attack and roll angle are qualitatively the same. The differences increase in accordance with the angle of attack. This appears to be the effect of the strong interaction between the jet flow and cross flow of the missile at large angle of attack. It can be seen that the difference between wind tunnel test and simulation results is large in the jet direction F3 and F5. It is believed that this is due to the high uncertainty of the wind tunnel test data in asymmetric jet injection condition

and the less accurate prediction of the jet interaction between two jets under multiple jet injection condition. The uncertainty level of the constructed jet interaction data was evaluated from the differences between the cold gas CFD simulation results and the wind tunnel test data. The root mean square (RMS) of the force coefficient differences was less than 0.1, while that of the moment coefficient differences was less than 0.5. The maximum error of the change of the center of pressure (ΔX_{cp}) owing to the jet interaction was measured as less than 1 caliber.

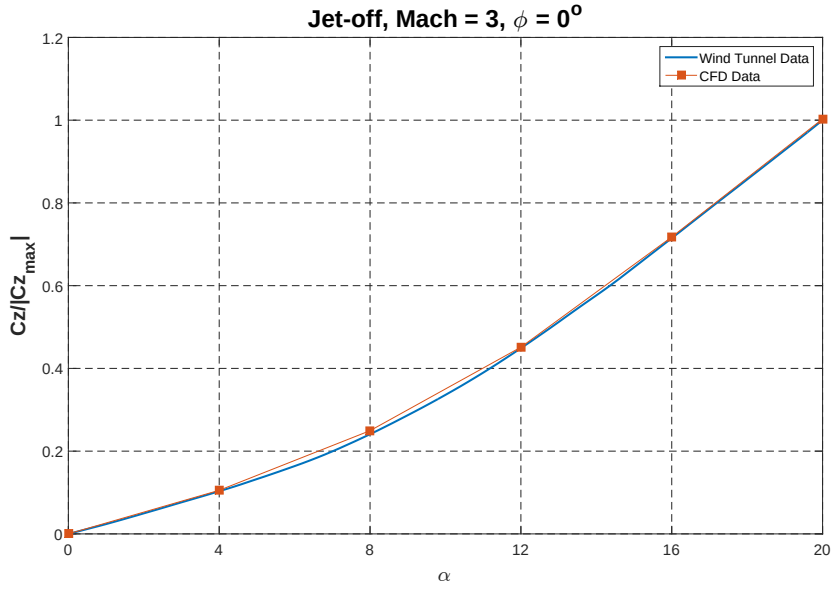

(a) Cz

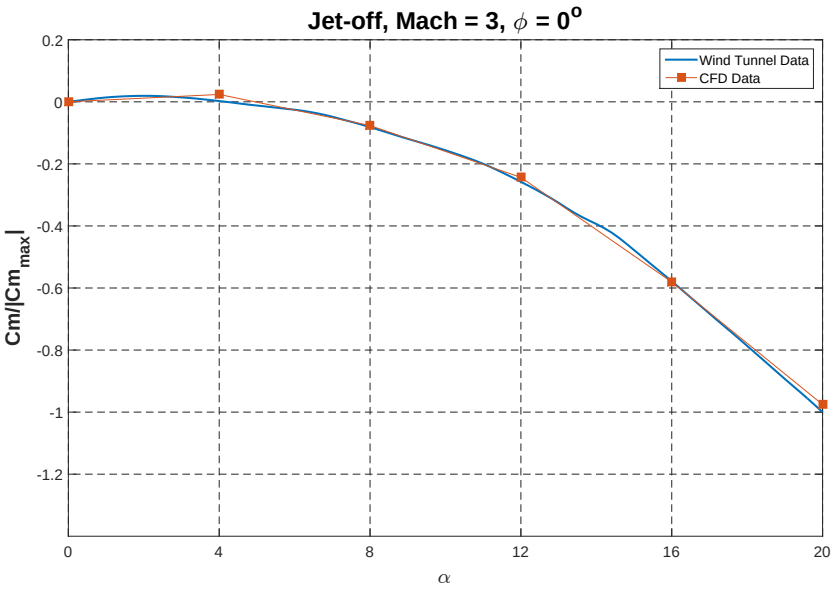

(b) Cm

Figure 3.5: Comparison of jet-off aerodynamic coefficients, M = 3.0 and $\phi = 0^o$

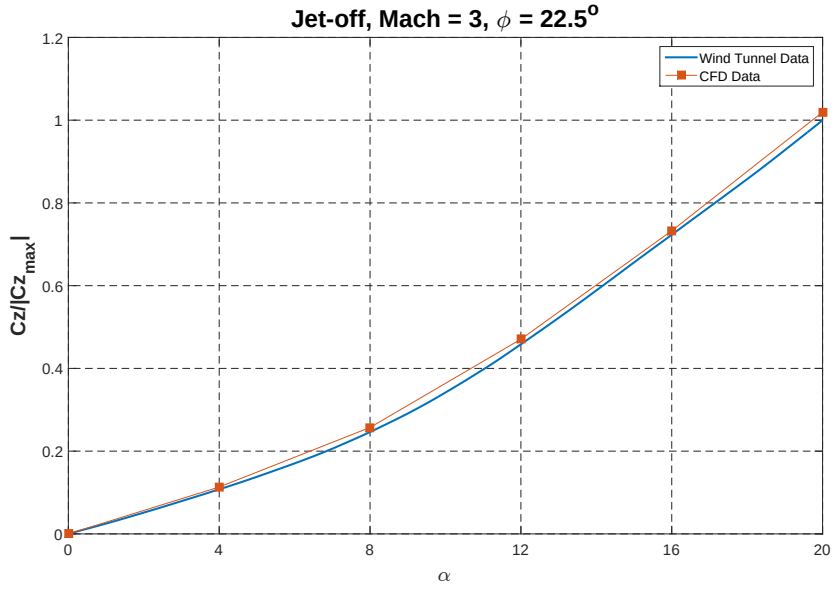

(a) Cz

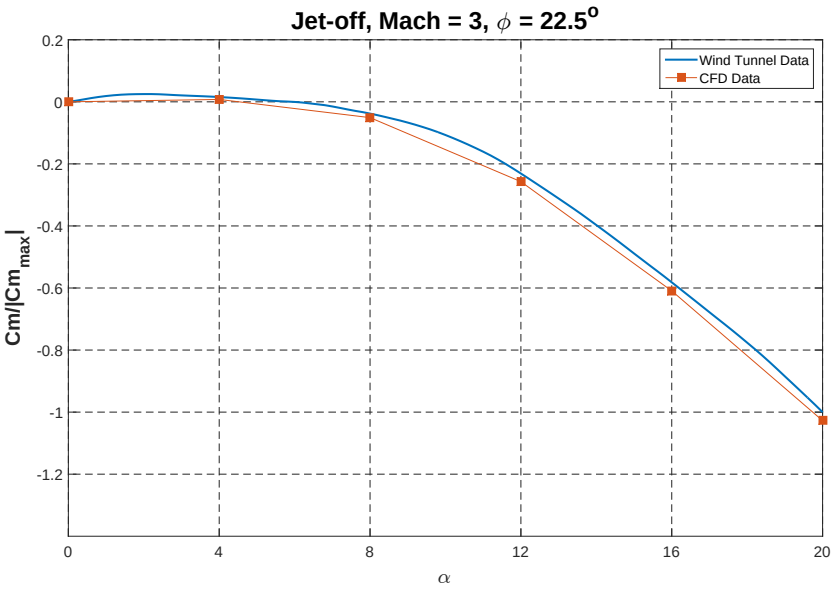

(b) Cm

Figure 3.6: Comparison of jet-off aerodynamic coefficients, M = 3.0 and ϕ = 22.5^o

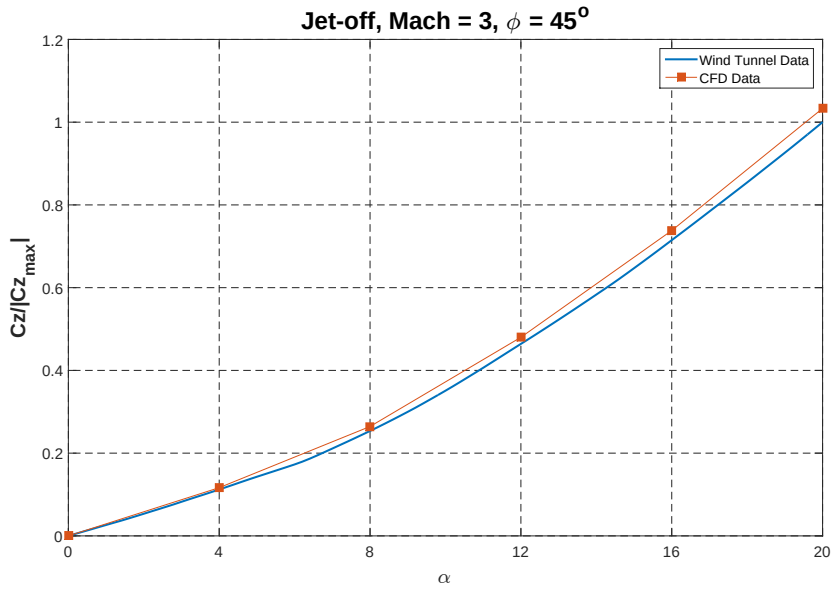

(a) Cz

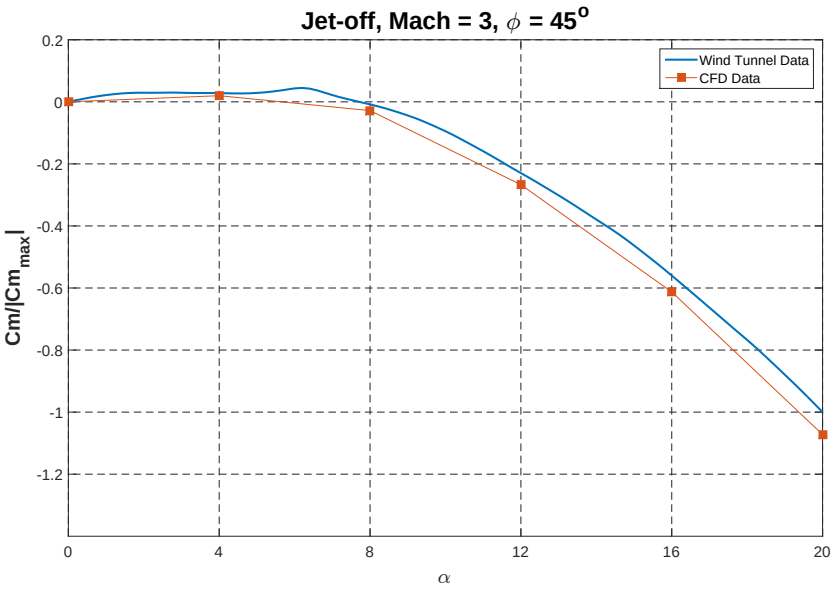

(b) Cm

Figure 3.7: Comparison of jet-off aerodynamic coefficients, M = 3.0 and $\phi = 45^o$

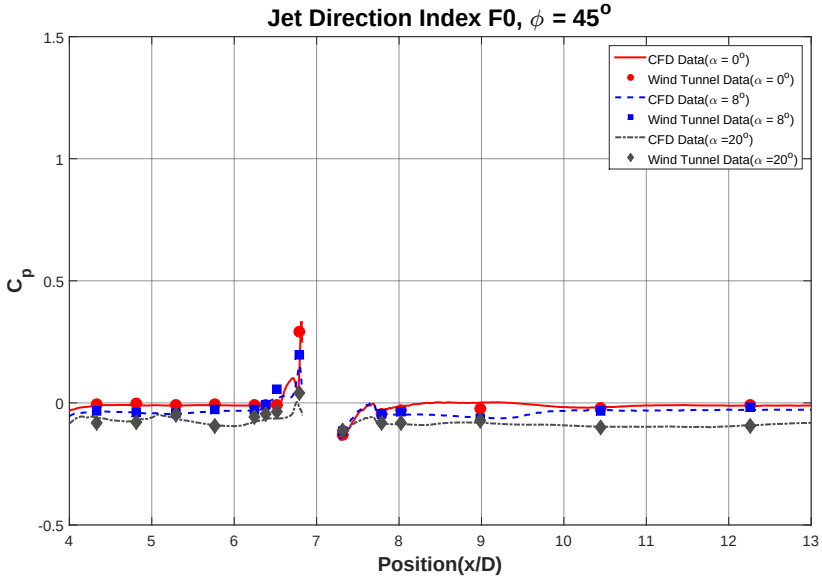

(a) $\phi = 0^o$

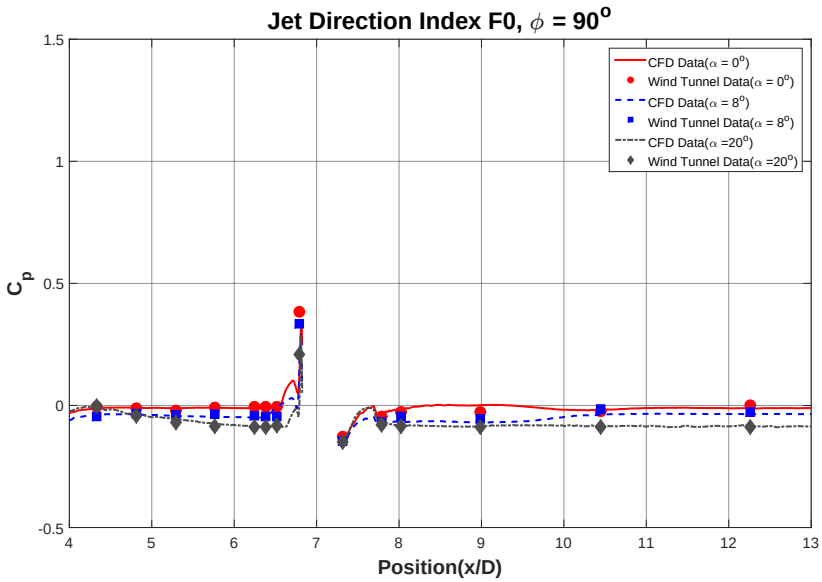

(b) $\phi = 180^o$

Figure 3.8: Comparison of surface pressure distribution, F0, M = 3.0 and MPR = 1.02

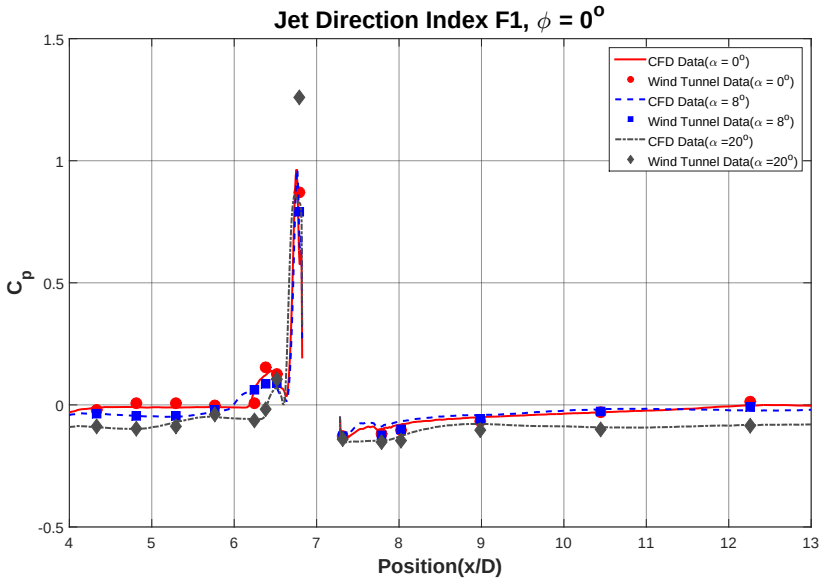

(a) $\phi = 0^o$

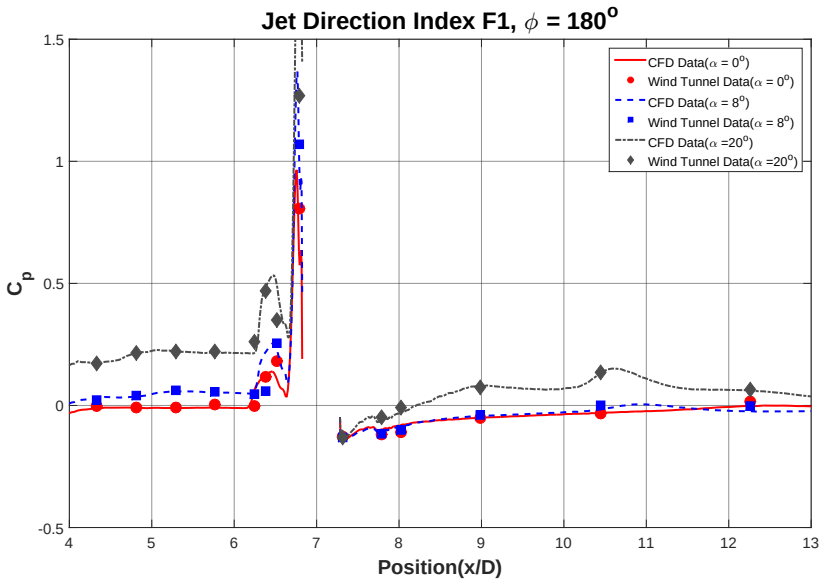

(b) $\phi = 180^o$

Figure 3.9: Comparison of surface pressure distribution, F1, M = 3.0 and MPR = 1.02

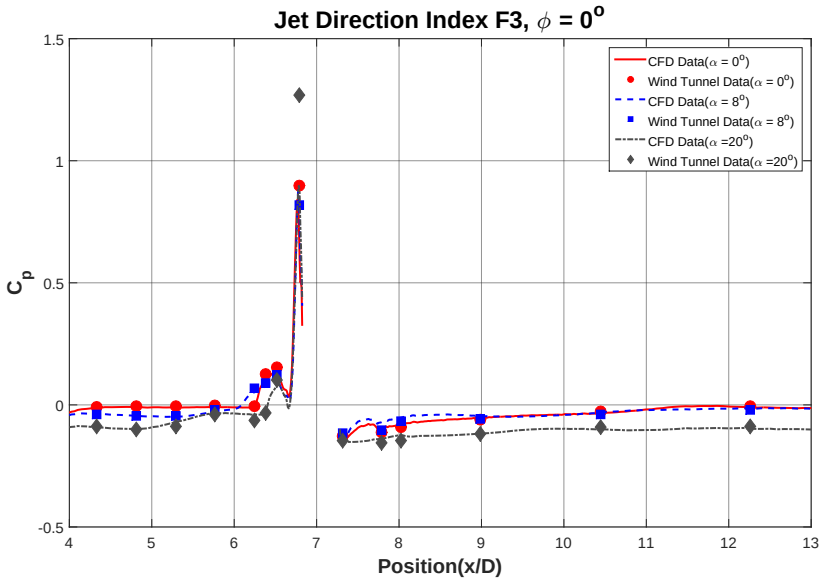

(a) $\phi = 0^o$

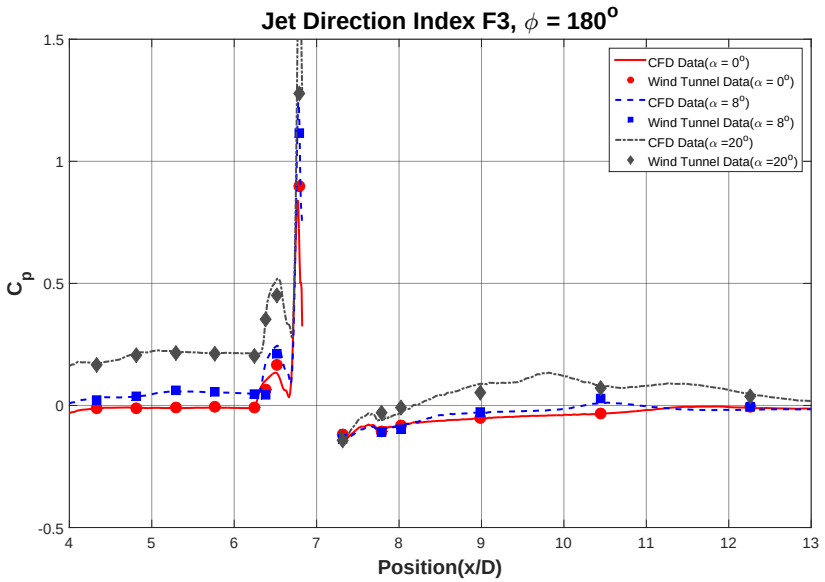

(b) $\phi = 180^o$

Figure 3.10: Comparison of surface pressure distribution, F3, M=3.0 and MPR=1.02

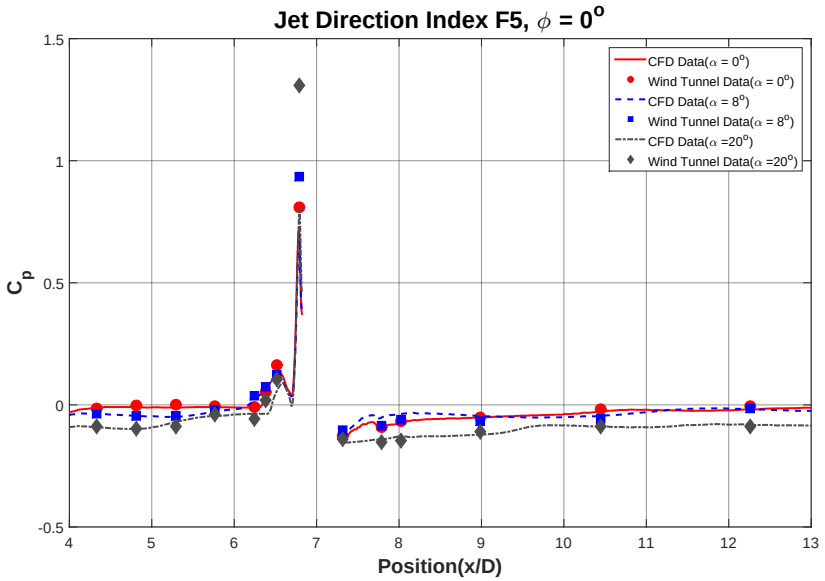

(a) $\phi = 0^o$

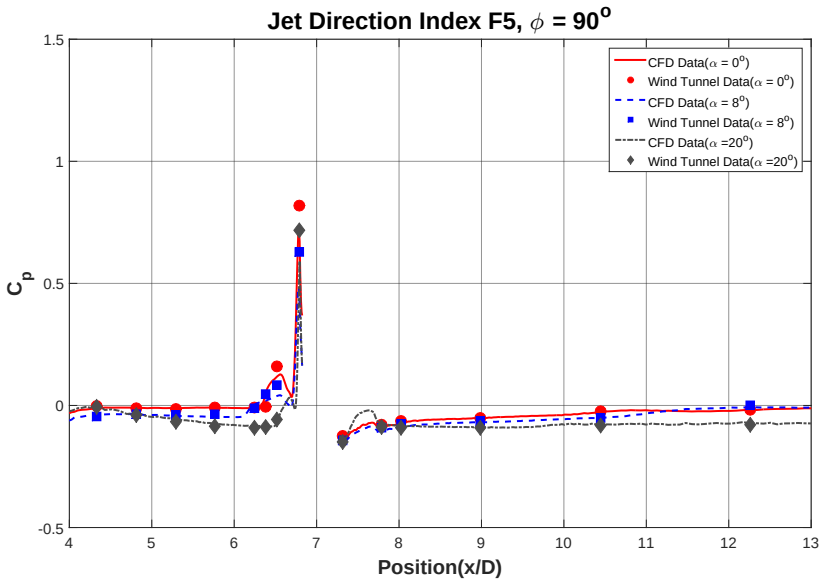

(b) $\phi = 180^o$

Figure 3.11: Comparison of surface pressure distribution, F5, M = 3.0 and MPR = 1.02

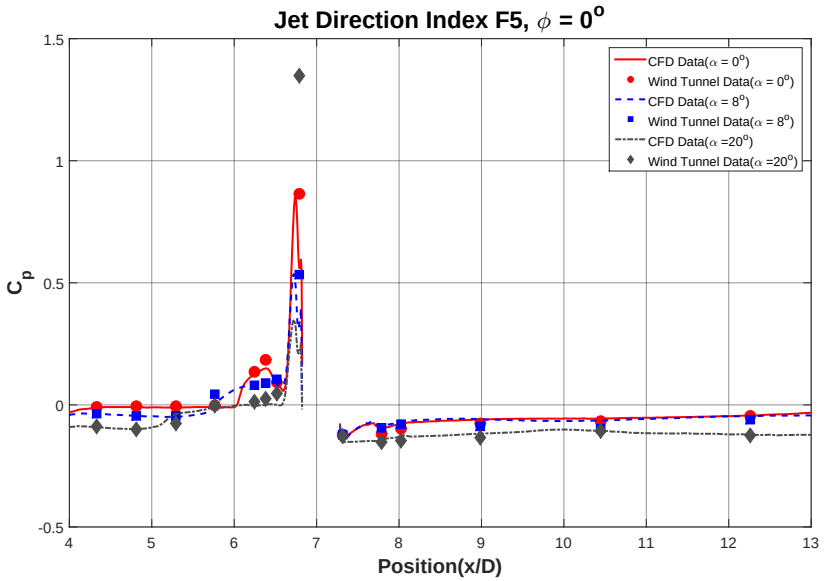

(a) $\phi = 0^o$

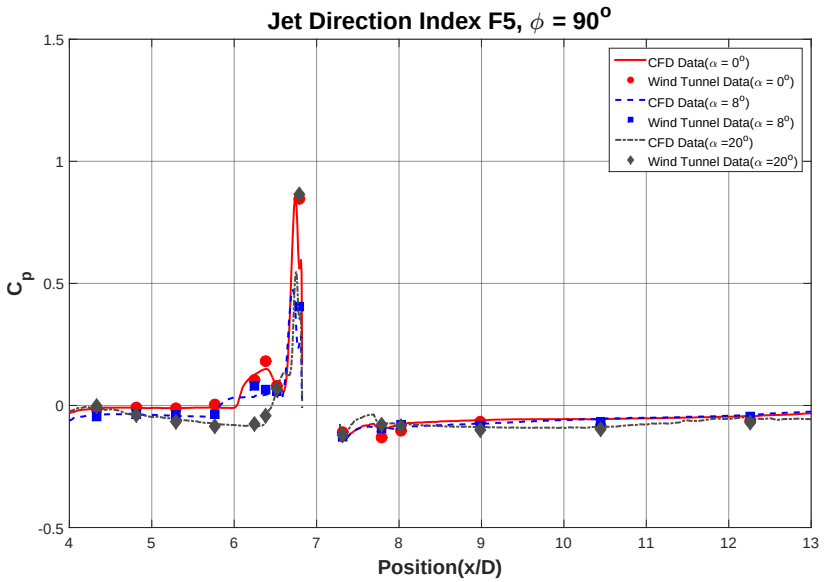

(b) $\phi = 180^o$

Figure 3.12: Comparison of surface pressure distribution, F5, M = 3.0 and MPR = 3.05

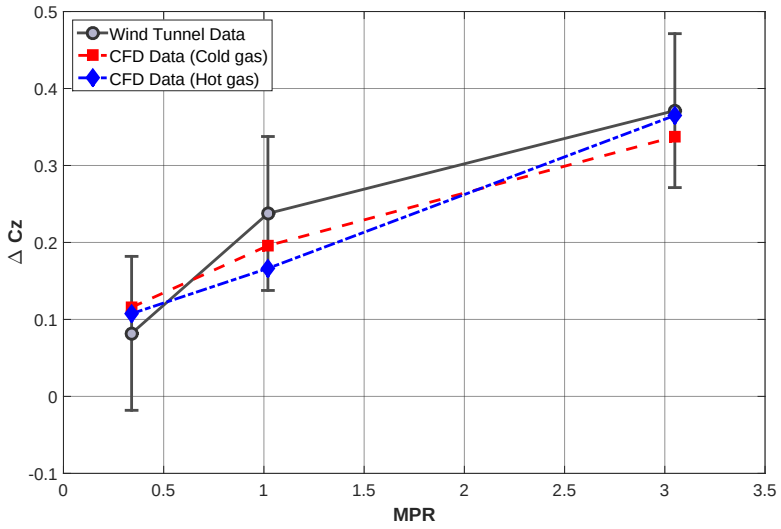

(a) ΔCz

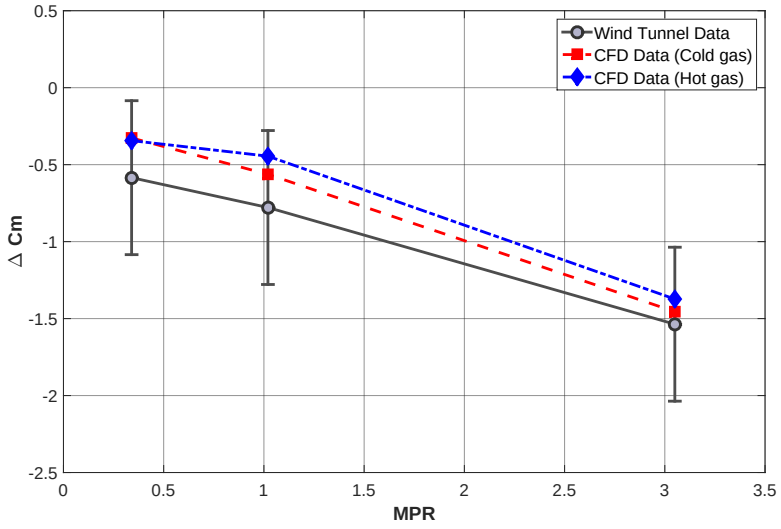

(b) ΔCm

Figure 3.13: Comparison of jet interaction aerodynamic coefficients for jet direction F1, M = 3.0, $\alpha_t = 0^o$ and $\phi = 0^o$

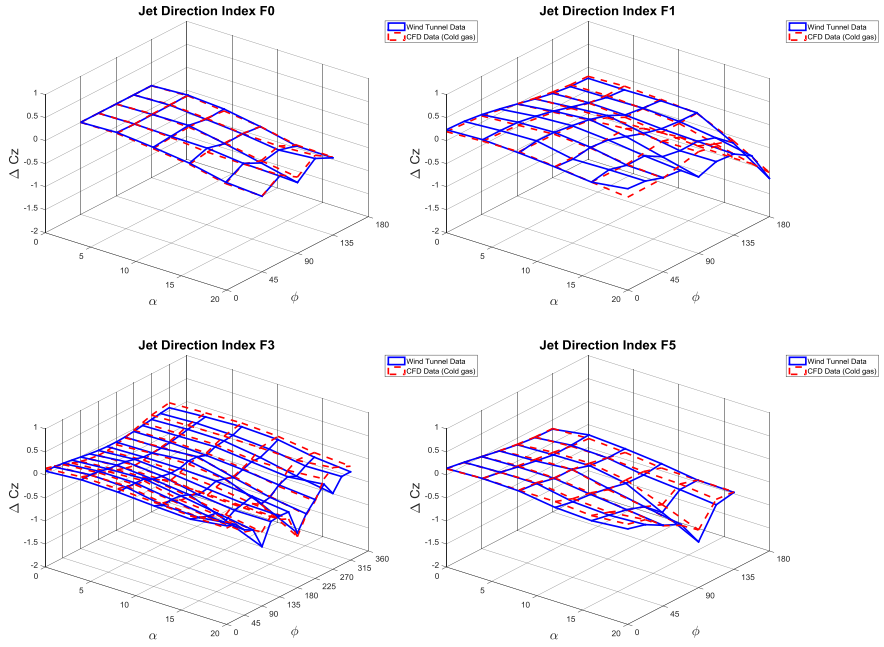

Figure 3.14: Jet interaction normal force coefficients for defined jet directions at M = 3.0 and MPR = 1.02

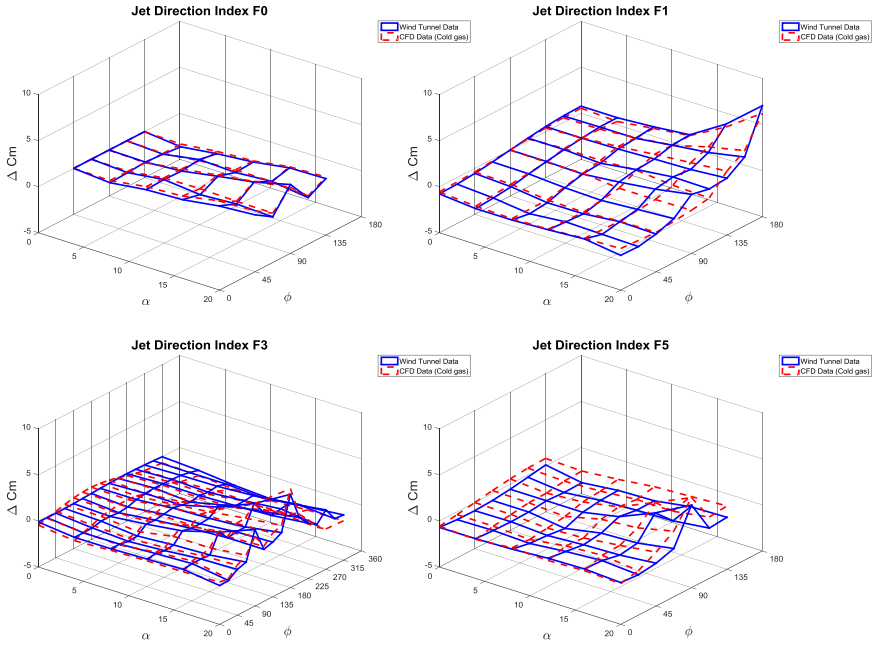

Figure 3.15: Jet interaction pitching moment coefficients for defined jet directions at M = 3.0 and MPR = 1.02

3.6 Investigation of Jet Interaction for Continuous Type Side-jet

3.6.1 Simulation results of continuous type side-jet

Numerical simulation was conducted for four jet direction conditions at various free-stream flow conditions. The qualitative features of jet interaction flow for the jet directions (F0, F1, F3, F5) at M = 3.0, MPR = 1.02 and $\alpha_t = 0^o$ is presented in terms of Mach number distribution in Fig. 3.16. The Mach contours at the side view and at the cross section of the nozzle center are compared for different jet direction conditions. The bow shock generated by obstruction of the jet changes all flow fields behind the side jet thruster. For the jet direction F0 case, jet interaction occurs symmetrically because the side jet turns on all thrusters in two orthogonal planes with the same strength. A slight asymmetry of the jet plume is caused by the orientation of nozzle throat opening device which is defined in Fig. 3.4. For the jet direction F1 case, a large jet interaction is observed at the fully opened thruster. Similar jet interaction flow characteristics according to jet thruster states are captured for the jet direction F3 and F5 cases. Figure 3.17 show the Mach contour under MPR = 3.05 condition. The qualitative flow change due to the jet injection is similar to the previous MPR = 1.02 condition, and the intensity of the obstruction by the jet is increased.

Figure 3.18 shows the contour of surface pressure coefficient in x-y plane for the jet directions (F0, F1, F3, F5) at M = 3.0, MPR = 1.02 and $\alpha_t = 0^o$. The distribution of surface pressure coefficient at MPR = 3.05 is shown in Fig. 3.19. The high pressure region in front of the nozzle exit and extensive low

pressure region behind the nozzle are observed. Each nozzle has a different jet strength according to their jet conditions and the high pressure regions moves forward as the strength of the jet increases. For jet direction F0, asymmetric pressure distribution in the circumferential direction due to the orientation of nozzle throat opening device. For jet direction F3 and F5, shock interaction occur at the point where the shock waves generated in two nozzle that are 90 degrees apart in the circumferential direction meet, resulting in different pressure distributions.

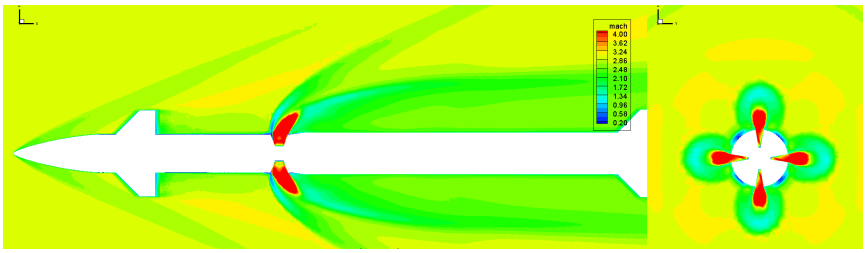

(a) Jet Direction F0

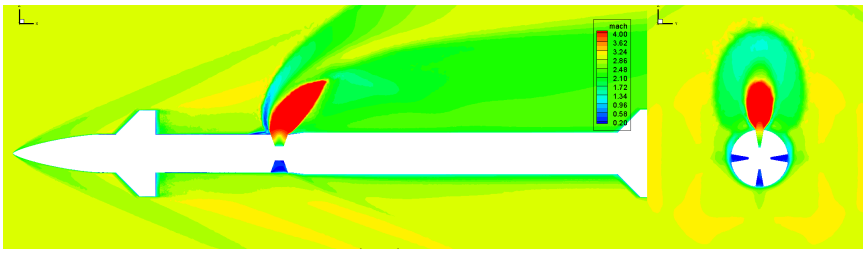

(b) Jet Direction F1

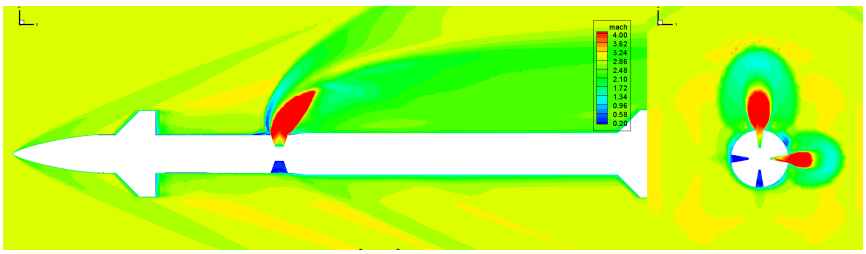

(c) Jet Direction F3

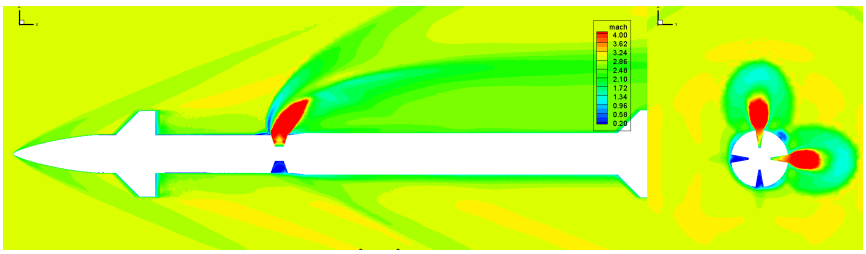

(d) Jet Direction F5

Figure 3.16: Mach contour of continuous type side-jet simulation results (M = 3.0, MPR = 1.02, $\alpha_t = 0^o$ and $\phi = 0^o$)

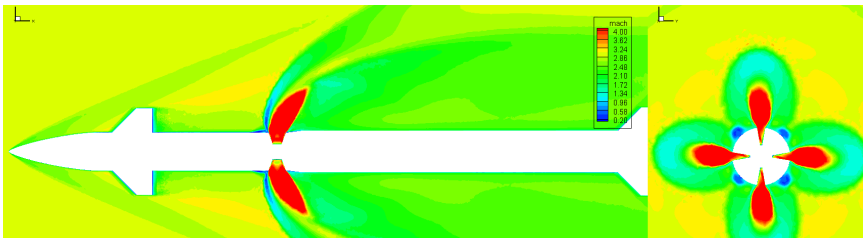

(a) Jet Direction F0

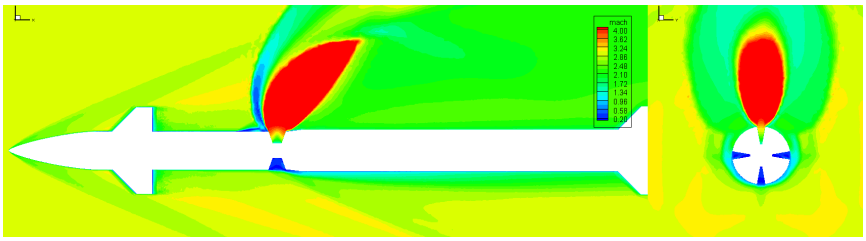

(b) Jet Direction F1

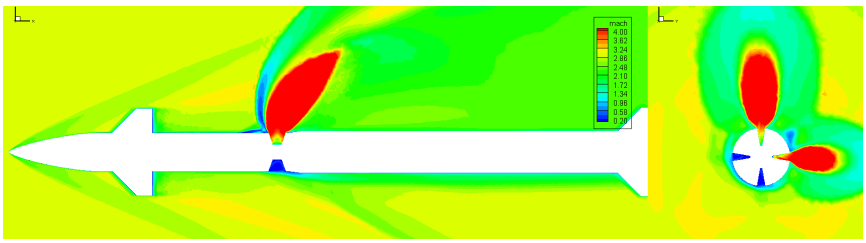

(c) Jet Direction F3

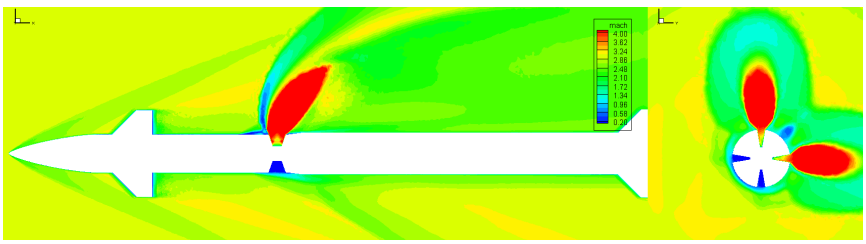

(d) Jet Direction F5

Figure 3.17: Mach contour of continuous type side-jet simulation results (M = 3.0, MPR = 3.05, $\alpha_t = 0^o$ and $\phi = 0^o$)

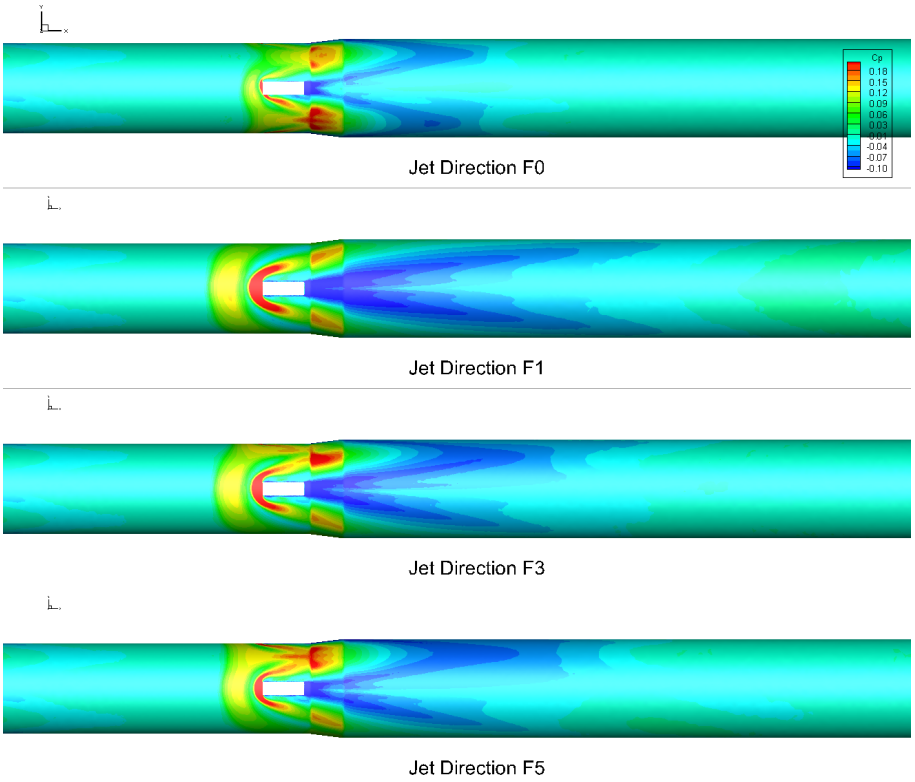

Figure 3.18: Surface pressure coefficient contour for different jet directions (M = 3.0, MPR = 1.02, $\alpha_t = 0^o$ and $\phi = 0^o$)

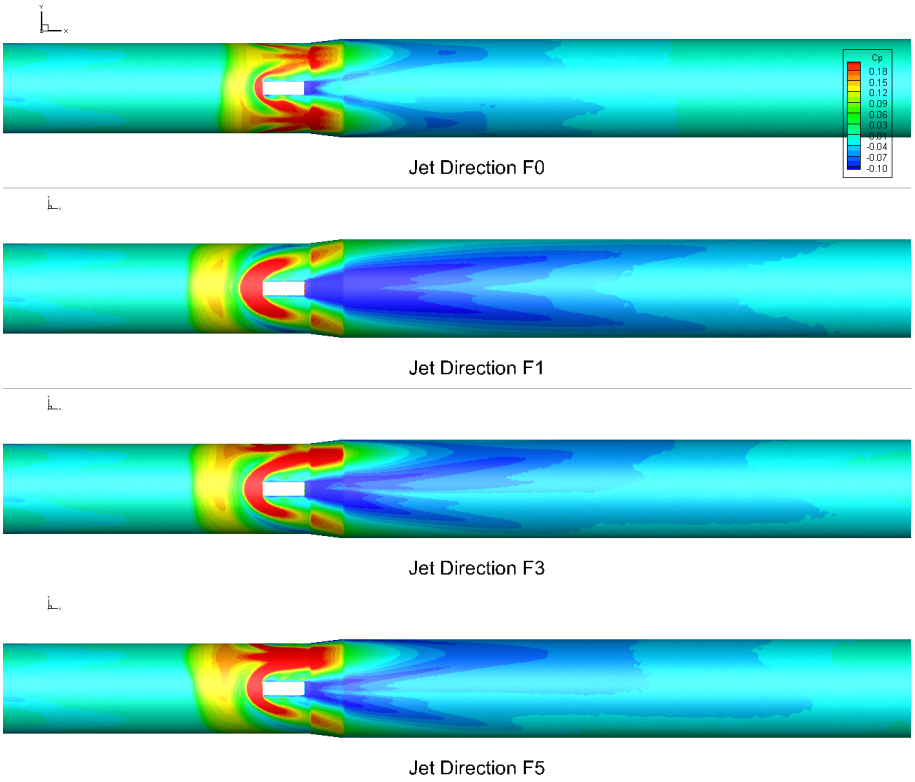

Figure 3.19: Surface pressure coefficient contour for different jet directions (M = 3.0, MPR = 3.05, $\alpha_t = 0^o$ and $\phi = 0^o$)

3.6.2 Flow Features of Jet Interaction for Continuous Type side-jet

Shock structure

The main shock features that characterize the supersonic jet interaction flow field is shown in Mach number contours on the $x-z$ plane of the computational domain in Fig. 3.20(a). The result of simulation at jet direction F1, M = 3.0, $\alpha_t = 0^o$, and $\phi = 0^o$ is displayed. The highly underexpanded supersonic jet exhausting into the supersonic cross flow produces an inclined barrel shock which terminates in a Mach disk. The barrel shock acts as a blunt body obstruction to the incoming flow thus forming a detached bow shock. A fully developed turbulent boundary is formed at the upstream of jet and, as it approaches the adverse pressure gradient created by the bow shock wave, it separates from the incoming flow. The separated boundary layer induces another shock wave, identified as the induced separation shock. Figure 3.20(b) shows the isometric view of density gradient around the vehicle, and the three-dimensional shape of the shock wave can be seen. Different from the case of the jet injection on the flat plate [34], the bow shock and the separation shock wave are formed in the form of wrapping around the body. Corresponding the longitudinal surface pressure coefficients C_p along the centerline containing nozzle N1 are shown in Fig. 3.9(a). The first increase in pressure is due to the separation induced shock and the second pressure rise represents bow shock due to barrel shock.

The momentum of free-stream causes the jet plume to trail downstream and to lose its axial symmetry. Looking at the interior volume of the barrel shock, a large expansion fan is present with its boundaries defined by a recom-

pression shock that ends with a Mach disk. Figure 3.21 shows the simulated shadowgraph of jet interaction flow field at F1, M = 3.0, $\alpha_t = 0^o$, and $\phi = 0^o$. The shadowgraph contour show that the separation shock and the bow shock caused by jet injection are captured well. Figure 3.22 shows an isometric view of the iso-surface around the jet nozzle exit with streamlines. The iso-surface of Mach number represents shape of the barrel shock induced by jet expansion. The barrel shock wave is shaped to have a narrow width according to the shape of the nozzle exit, and is bent downward by the free-stream. It is evident that the barrel shock acts as an obstacle to the external flow and causes a flow separation at upstream of the jet.

Vortical structure

The Q-criterion was employed for the vortical structure identification, which represents the local balance between shear strain rate and vorticity magnitude. It defines vortices as areas where the vorticity magnitude is greater than the magnitude of rate of strain as follows

$$Q = \frac{1}{2}\left(\|\Omega\|^2 - \|S\|^2\right) > 0, \tag{3.8}$$

where Ω is the vorticity tensor and S is the rate of strain tensor [35, 36] .

The jet interaction flow field and its vortical structures is provided by the isometric view of Q-criterion, as shown in Fig. 3.23(a). The result of simulation at jet direction F1, M = 3.0, $\alpha_t = 0^o$, and $\phi = 0^o$ is displayed. This figure illustrates four types of vortical structures: (1) a pair of counter-rotating vortices whose axis is aligned with the downstream direction; (2) the horseshoe vortex of upstream of the jet originated from boundary layer separation; (3) the trail-

ing lower vortices behind the jet; (4) the trailing vortices stemming from the separation region that are formed in far downstream. These vortical structures of the jet interaction flow field is similar to the case of the crossflow over a flat plate [34, 37] except for the wrapping around effect of horseshoe vortices [38]. Unlike the flow over a flat plate, it can be seen that the separated flow ahead of the jet spreads laterally and downwards to the bottom of the body indicating the path of the horseshoe vortices.

Figure 3.23(b) shows the vorticity magnitude contour on the cross plane ($y - z$ pane) of the body. It is evident that the counter-rotating vortices and the horseshoe vortices are strong vortical sources of the jet interaction flow field. Entrainment of crossflow of free-stream appears to be clearly enhanced as the jet is deformed and as vortex rollup results in the formation of counter-rotating vortices [39]. These counter-rotating vortices are strong enough to reach far back of the body. The horseshoe vortices originated from boundary layer separation form and move away from the centerline of the jet. The horseshoe vortices move along the sideway of body surface.

The lower trailing vortices are formed from the flow separation of free-stream as it moves away from the jet as barrel shock expands around the nozzle and as it moves back to the center when the barrel shock detaches from the surface. These vortices remain attached to the solid surface as it entrains fluid from the surrounding boundary layer. The trailing vortices are formed boy the recirculating fluid close to the plane of symmetry, and it follows the leading edge of the barrel shock away from the solid surface.

For the single jet injection case F1, it can be seen that the vortical structure become very complicated as the angle of attack increases in Fig 3.25. The

horseshoe vortex are detached from the body and the body vortices originated from cross flow are interact with vortices formed from the jet. At the angle of 20 degrees, canard vortices and body vortices are merged with the vortices generated by the jet. When the crossflow component of the free-stream is blown in the direction of jet injection, the strong counter-rotating vortices impinges on the windward body surface. Therefore, strong jet interaction occurs at the jet injection into the windward side.

Figures 3.24, 3.26 and 3.27 show the vortical structure for multiple jet injection conditions of the continuous type side-jet (F0, F3, and F5). The four types of vortical structures are formed at each jet injection nozzle with different strength according to their own jet magnitude and they are interact with canard vortices and body vortices depending on the attitude angle of the missile. The largest jet interference on the body occurs when the jet is injected in the windward direction.

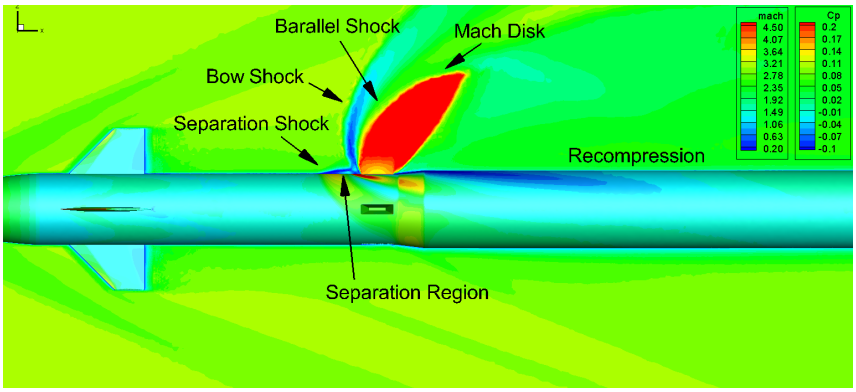

(a) Mach number and surface pressure coefficient contour

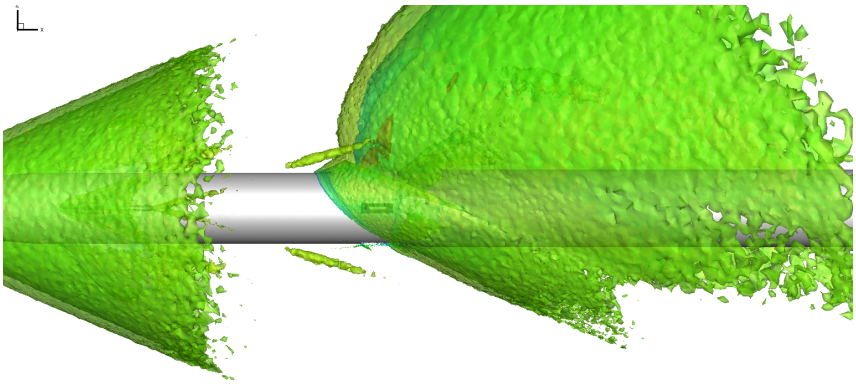

(b) Density gradient isosurface

Figure 3.20: Shock structure of jet interaction (F1, M = 3.0, MPR = 1.02, $\alpha_t = 0^o$ and $\phi = 0^o$)

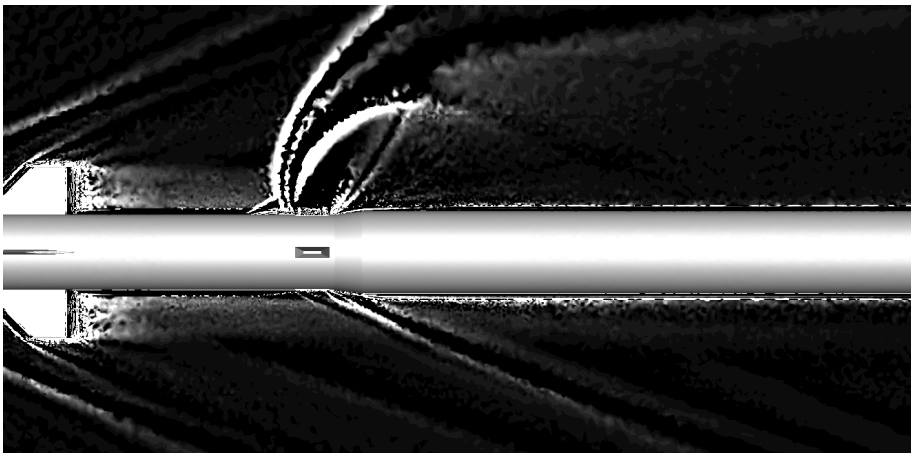

Figure 3.21: Simulated shadowgraph of jet interaction flow field (F1, M = 3.0 and MPR = 1.02)

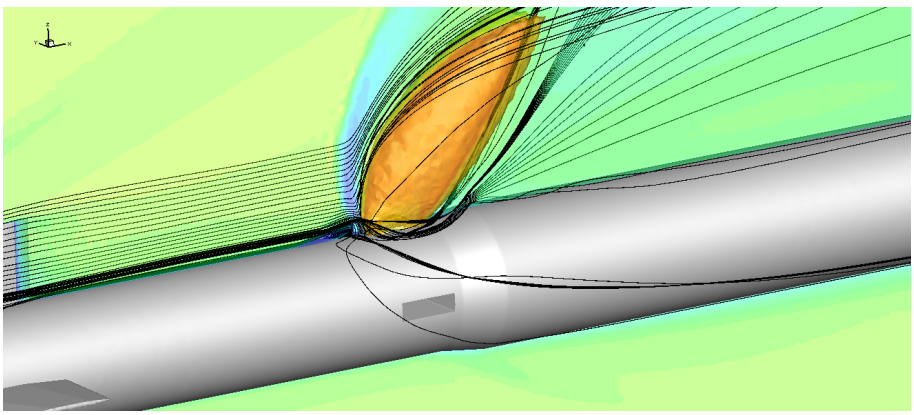

Figure 3.22: Isometric view of Mach 3.4 iso-surface with streamlines (F1, M = 3.0 and MPR = 1.02)

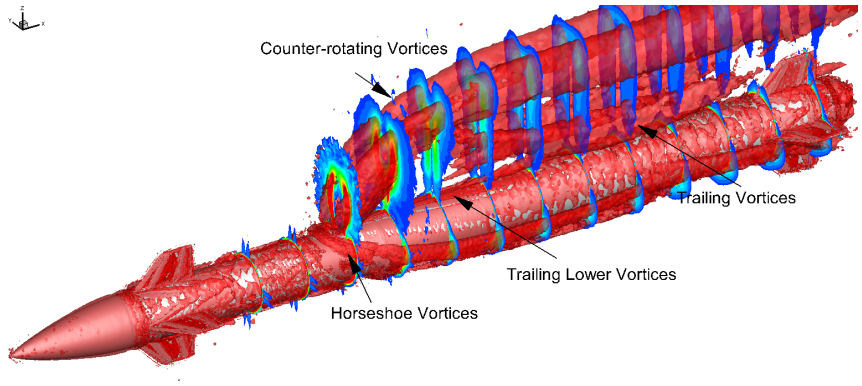

(a) Isometric view of Q-criterion

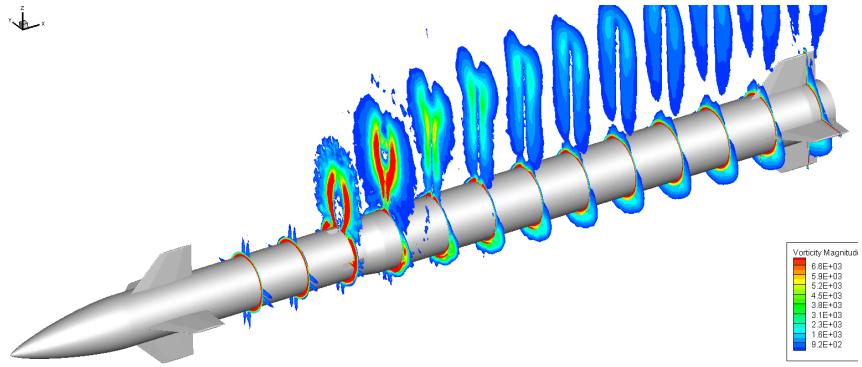

(b) Vorticity magnitude in the $y-z$ plane

Figure 3.23: Vortical structure of jet interaction (F1, M = 3.0, MPR = 1.02, $\alpha_t = 0^o$ and $\phi = 0^o$)

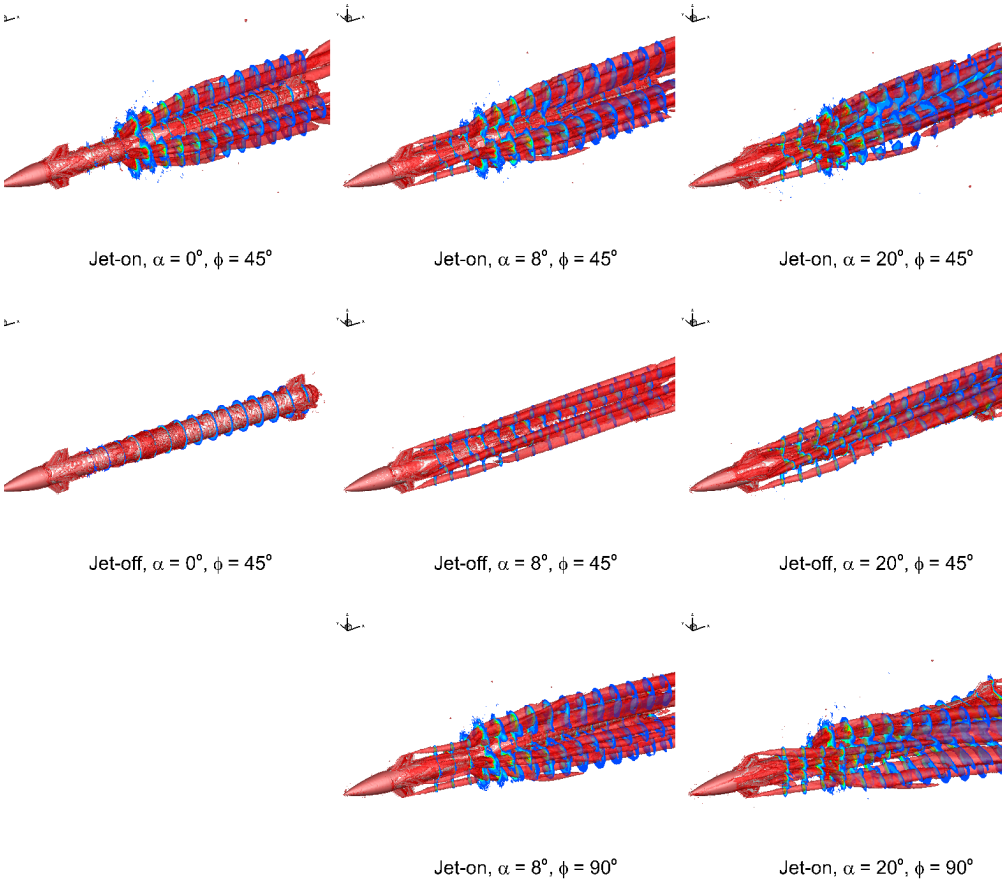

Figure 3.24: Comparison of Q-criterion iso-surface for various flow conditions(F0, M=3.0 and MPR = 1.02)

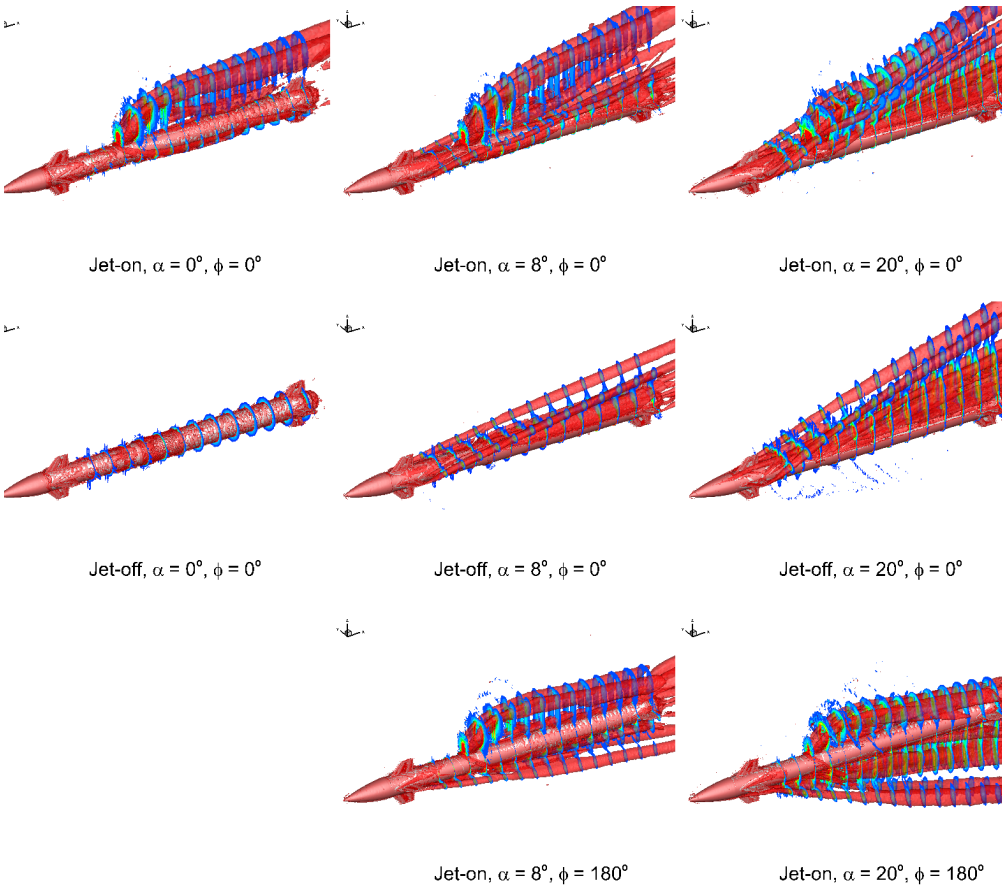

Figure 3.25: Comparison of Q-criterion iso-surface for various flow conditions(F1, M=3.0 and MPR = 1.02)

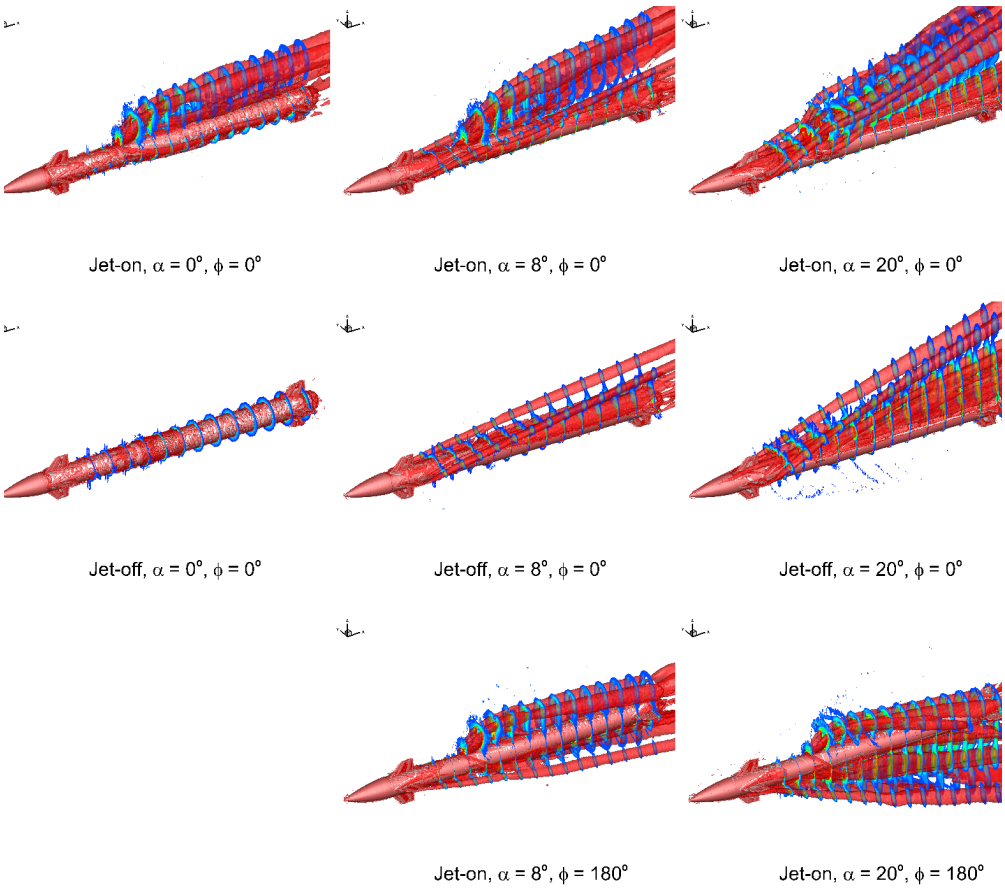

Figure 3.26: Comparison of Q-criterion iso-surface for various flow conditions(F3, M=3.0 and MPR = 1.02)

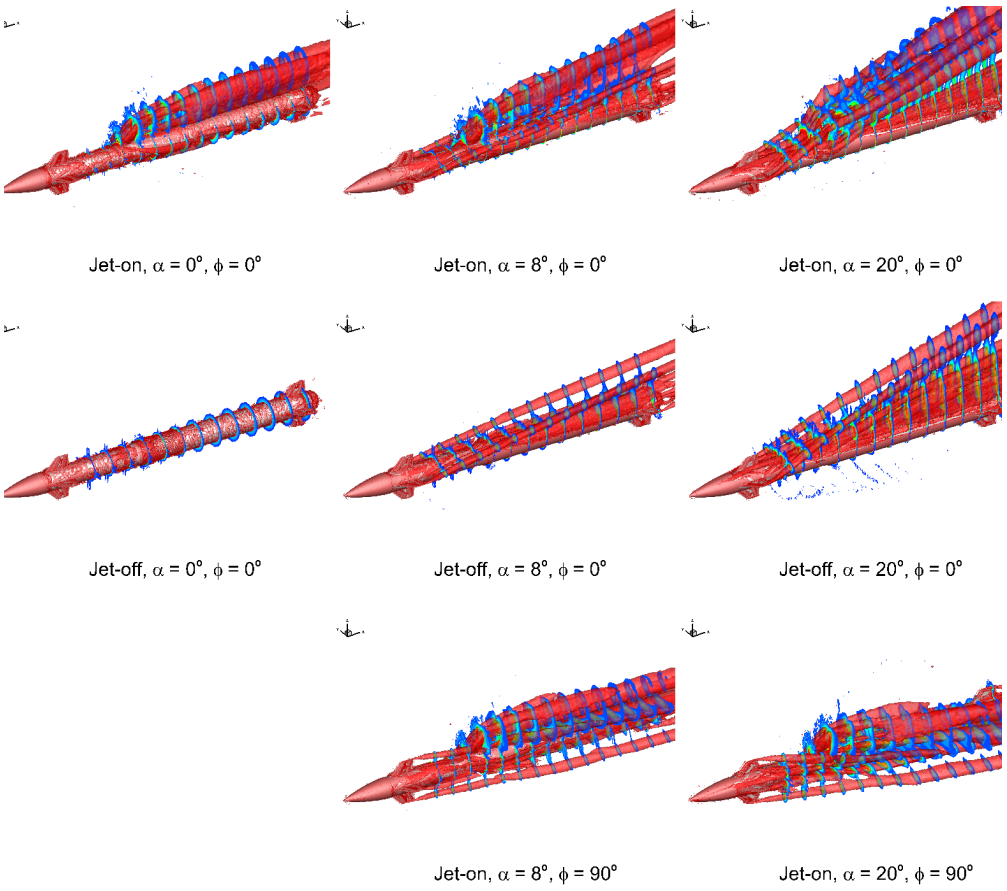

Figure 3.27: Comparison of Q-criterion iso-surface for various flow conditions(F5, M=3.0 and MPR = 1.02)

3.6.3 Effect of jet interaction parameters

The effects of the angle of attack and the roll angle on jet interaction normal forces and pitching moments for the various jet directions are shown as a surface plot in Fig. 3.28. All jet interference aerodynamic coefficients are measured in the aerodynamic axis system. The peak jet interference for each jet direction case occurs when the main thruster, the largest opened nozzle, is located in the windward direction. It is clear from the Figure that with the increase in angle of attack, the jet interference has increased. The maximum jet interference is observed in the jet direction F1 at $\phi = 180^o$. The change of jet interaction effects along the roll angle in the jet direction F0 case is small because all nozzles are symmetrically opened. The jet interaction acts on unfavorable direction because they diminish normal forces and increase pitching moments at the center of gravity.

Figure 3.29 shows the changes of side force and yawing moment coefficients due to jet interaction. The asymmetrical side forces and yawing moments are generated according to the angle of attack and flow bank angle in the jet directions F1 – F3. But the magnitude of jet interference side forces and yawing moments are small compared to normal forces and pitching moments.

To evaluate the asymmetry effect of the jet, a numerical simulation was carried out for the jet direction $\theta_j = 67.5^o$ with the same flow conditions. The results are shown in Fig. 3.30. The peak jet interference occurs at a roll angle of $\phi = 90^o$ when the main thruster is located in the windward direction. The interaction effect for the jet direction $\theta_j = 67.5^o$ and F3 can be replaced reciprocally because they show the same jet interaction characteristics at a phase-shifted roll angle. These results are rationalized by the symmetry of the

jet nozzle and it supports the neglect of the orientation of the nozzle throat opening device.

From the investigation of jet interaction with various roll angles, jet interference aerodynamic coefficients for jet directions F0, F1 and F5 repeat in the flow roll angle with the period of $\pi/2$, π and π respectively. These periodicities in roll angle come from mirror symmetry of jet flow on the cross sectional plane. A significant number of cases for constructing a 6-DOF aerodynamic database of jet interference can be reduced for by using this characteristic.

Figure 3.31 presents the results obtained at differing MPR conditions for the jet direction F0 at Mach number = 3.0. The free-stream Mach number effect on jet interference at MPR = 1.02 is shown in Fig. 3.32. We observe that when MPR increases, the jet interaction forces are increased due to a larger obstruction of jet flow. This is because increased jet momentum at a high MPR condition causes a larger separated low pressure region behind of jet flow. The differences of jet interaction effect between M = 3.0 and M = 3.6 are small at a low angle of attack. At a high angle of attack ($\alpha_t > 14^o$), as Mach number increased, the jet interaction forces decrease. When the Mach number increases, the pressure in the recirculation region increases. As a result, the induced jet interaction force decreases when the Mach number increases. This effect is distinct at a high angle of attack because a large amount of normal forces are generated on the body. These trends are consistent with the previous results from comparison of simulation with wind tunnel test.

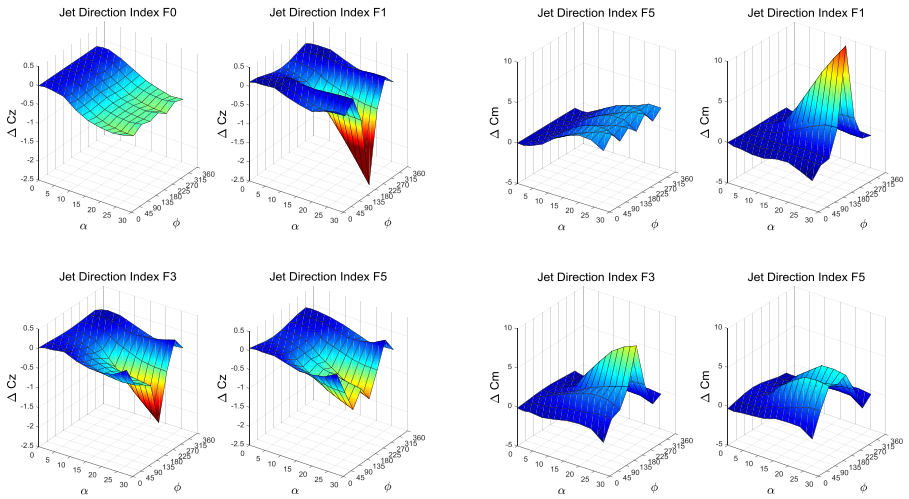

(a) ΔCz (b) ΔCm

Figure 3.28: Jet interaction normal force and pitching moment coefficients (M = 3.0 and MPR = 1.02)

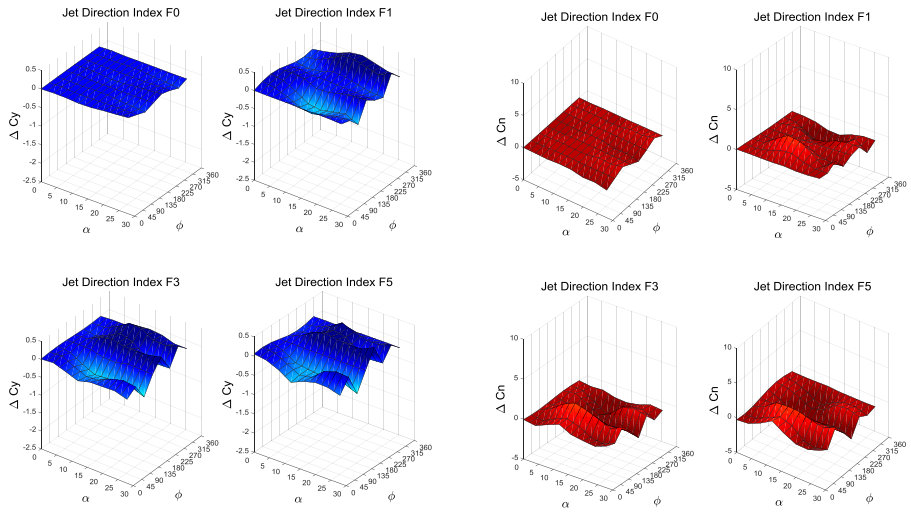

(a) ΔCy (b) ΔCn

Figure 3.29: Jet interaction side force and yawing moment coefficients (M = 3.0 and MPR = 1.02)

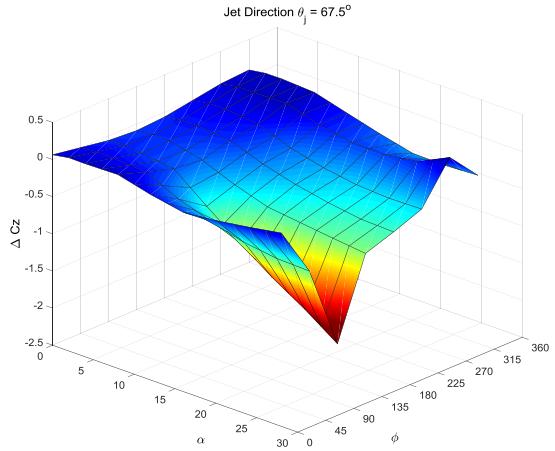

Figure 3.30: Jet interaction normal force coefficient for the jet direction $\theta_j = 67.5^o$ at M = 3.0 and MPR = 1.02

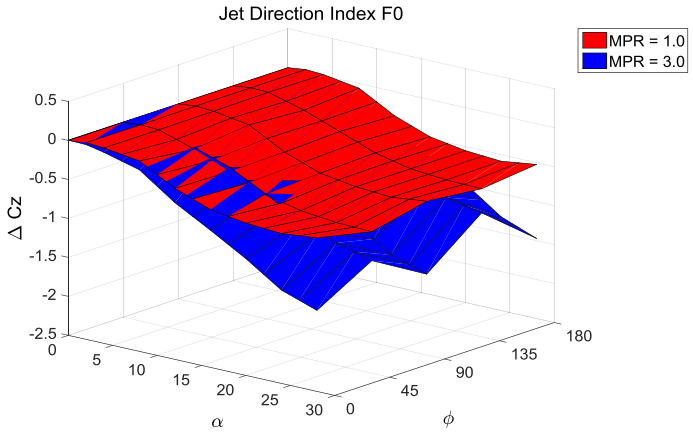

Figure 3.31: Effect of MPR on jet interaction force coefficient (F0 and M = 3.0)

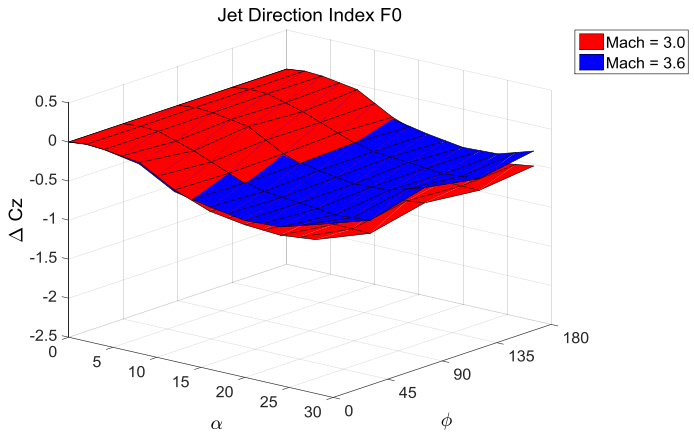

Figure 3.32: Effect of free-stream Mach number on jet interaction force coefficient (F0 and MPR = 1.02)

Chapter 4

Surrogate Modeling of Jet Interaction Aerodynamic Database for Continuous Type side-jet

4.1 Jet interaction aerodynamic database of continuous type side-jet

In the missile development stage, the aerodynamic database has to be developed to provide aerodynamic data that are used to develop the guidance, navigation and control(GN&C) systems and to simulate the trajectory of the vehicle. For the continuous type side-jet thruster controlled missile, the jet interaction aerodynamic database is needed as well as nominal aerodynamic database.

The modeling approach of aerodynamics for the missile is to use an incremental forms as shown in Eq.4.1. The each term is isolated and evaluated separately, then combined by linear superposition to produce the final data. Although this approach has the disadvantage of neglecting coupling effects between the terms, it can simplify the model and reduce the number of experiments and simulations [40]. Aerodynamic coefficients of zero deflection C_{w0} and the increment terms of control surface deflections $\Delta C_{w_{\delta_p,\delta_y,\delta_r}}$ were developed from wind tunnel test data and computational simulation results. Additional

aerodynamic data due to jet interaction($\Delta C_{w_{JI}}$) were constructed by CFD simulation data with a certain level of confidence.

$$C_w = C_{w0} + \Delta C_{w_{\delta p}} + \Delta C_{w_{\delta y}} + \Delta C_{w_{\delta r}} + \Delta C_{w_{JI}} \tag{4.1}$$
$$where, C_w = C_x, C_y, C_z, C_l, C_m, C_n$$

Recall that the incremental aerodynamic data of jet interaction are function of many parameters including flight Mach number, altitude, angle of attack, roll angle of missile, magnitude of jet forces and desired jet direction as shown in Eq.3.3. Considering all operation regions of side-jet thruster, large amount of aerodynamic data are needed in modeling of jet interaction aerodynamic database.

4.2 Defined Jet Direction Conditions

The aerodynamic database of jet interaction, which can be described by two parameters, i.e., jet thrust scale and jet direction, should cover all possible operating regions. Considering the side-jet operation range, the database was constructed for jet directions from 0° to 360° in increments of 22.5° and jet thrust scale range from 0 to 1 in increments of 0.5. However, a large number of numerical simulations or experiments is required to fill these data space. Thus, a defined jet direction strategy was introduced to reduce the simulation cases. The idea of this approach is that a limited set of jet firing combinations can represent all other jet conditions using vehicle symmetry assumptions. The selected seven jet directions for 0°, 22.5°, and 45° from F0 to F6 are shown in Fig. 4.1, and their nozzle thrust states are shown in Table 4.1. A detailed

method of extending the jet direction from 0° to 360° using seven defined jet direction using mirror symmetry is described in Appendix. A. The numerical simulation was conducted for these seven defined jet conditions. Then, jet interaction effects of other jet direction conditions were reproduced from the results of defined jet directions. There were asymmetrical sources that violate the symmetry assumptions because of the different orientation of nozzle switching devices. However, we concluded that the effect of asymmetry is negligible based on previous numerical investigations.

Table 4.1: Defined jet direction conditions and nozzle thrust states

Thrust angle	$F_{\max}/T_{\max}$	Scale	Thrust[%]				Jet direction index
θ_j[deg]	[0 - 1]	$F_d/F_{\max}$	N1	N2	N3	N4	
		1	100	0	0	0	F1
0^o	1.0	0.5	62.5	12.5	12.5	12.5	F2
		0	25	25	25	25	F0
		1	70.7	29.3	0	0	F3
22.5^o	0.765	0.5	62.5	12.5	12.5	12.5	F4
		0	25	25	25	25	F0
		1	50	50	0	0	F5
45^o	0.707	0.5	37.5	37.5	12.5	12.5	F6
		0	25	25	25	25	F0

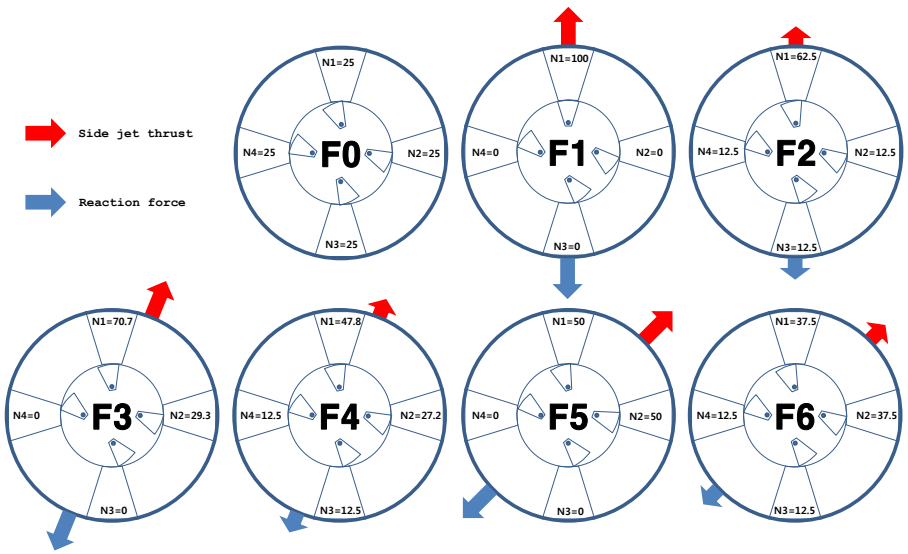

Figure 4.1: Defined jet directions(Rear View)

4.3 Jet interaction modeling strategy

Modeling the jet interaction aerodynamic database of the missile with continuous type side-jet controller requires a large data space. Table 4.2 lists the requiring design space of jet interaction aerodynamic database. Even with the discrete range of angle of attack and roll angle, it demands about 90,000 data points. It is nearly impossible to fill in all areas of the design space, especially with the time and resource constraints attached to any experimental or numerical simulation.

In this study, the defined jet direction method in Section 4.2 was applied to reduce the number of requiring data space. Table 4.3 shows reduced design space of jet interaction aerodynamic database with this method. An all of possible jet firing combinations are combined into the seven jet directions, resulting in a 90% reduction of overall design space. This allows constructing aerodynamic database with numerical simulations. However, this approach is not a practical in the initial stage of system development, since it still requires large amount of time and computational resources. As an alternatives, a surrogate modeling method, using appropriate sampling and interpolation methods, was applied in the construction of jet interaction aerodynamic database with a reduction of the number of computational simulations. These collective modeling procedures are shown in Fig. 4.2.

Table 4.2: Requiring full design space of jet interaction aerodynamic database

Parameter	Ranges	Number of parameter
Mach	M1, M2, M3, M4, M5	5
Altitude	H1, H2, H3	3
α	$0^0 \sim 28^0$ with increment of 4^o	8
ϕ	$0^0 \sim 337.5^0$ with increment of 22.5^o	16
$\|F\|$	0.0, 0.5, 1.0	3
θ_j	$0^0 \sim 337.5^0$ with increment of 22.5^o	16
	Total number of data	92160

Table 4.3: Reduced design space of jet interaction aerodynamic database

Parameter	Ranges	Number of parameter
Mach	M1, M2, M3, M4, M5	5
Altitude	H1, H2, H3	3
α	$0^0 \sim 28^0$ with increment of 4^o	8
ϕ ,$\|F\|$, θ_j	F0, F1, F2, F3, F4, F5, F6	73
	Total number of data	8760

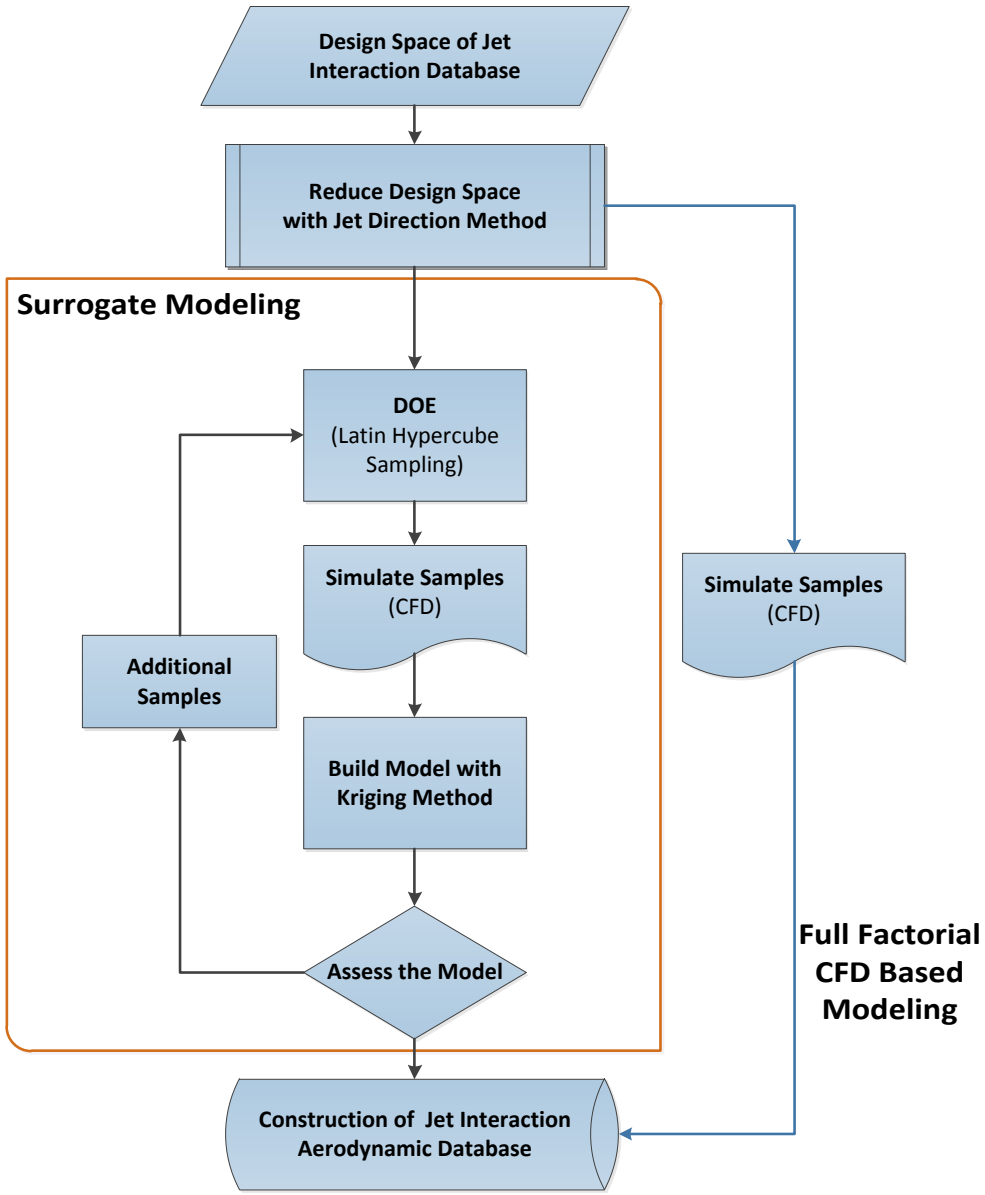

Figure 4.2: Modeling procedure of jet interaction aerodynamic database

4.4 CFD-Based Modeling of Jet Interaction

4.4.1 Numerical simulation for jet interaction modeling

Extensive CFD simulations were performed at the previously defined jet direction conditions. Five free-stream Mach numbers in the supersonic region and three altitude conditions in the stratosphere were selected to fill the database space. The jet to free-stream momentum parameter ratio (MPR) was used as a similitude parameter of jet flow for the experiments and analysis. Table 4.4 specifies the simulation Mach numbers, altitude, and corresponding MPR conditions. The aerodynamic database covers an angle of attack range from 0^o to 28^o and roll angle range from 0° to 360°. To reduce the simulation cases, the conditions involving the least roll angles at each defined jet direction by using symmetry relations were selected from Table 4.5 for the simulation. The simulations were conducted for jet-off and jet-on states at these flow conditions.

Table 4.4: MPR conditions for simulation Mach numbers and altitudes

Altitude \ Mach	M1	M2	M3	M4	M5
H1	0.53	0.34	0.24	0.15	0.12
H2	1.59	1.02	0.71	0.45	0.37
H3	4.76	3.05	2.12	1.36	1.10

Table 4.5: Roll angle conditions at defined jet directions

Jet direction index	Missile roll angle
F0	$0^o - 90°$ in interval of 22.5°
F1	$0^o - 180°$ in interval of 22.5°
F2	$0^o - 180°$ in interval of 22.5°
F3	$0^o - 337.5°$ in interval of 22.5°
F4	$0^o - 337.5°$ in interval of 22.5°
F5	$0^o - 135°$ in interval of 22.5°, 315°, and 337.5°
F6	$0^o - 135°$ in interval of 22.5°, 315°, and 337.5°

4.4.2 CFD-based jet interaction modeling results

For the construction of the jet interaction aerodynamic database, six components of aerodynamic coefficients were obtained from the CFD simulations. The jet interaction effects were calculated as the difference between the aerodynamic coefficients with and without jet flow. The bow shock, which is generated by the jet obstruction, changes all flow fields behind the side-jet thruster, and complex vortical structures are formed along the jet plume. As a result, the aerodynamic coefficients of the missile are changed. For each jet direction condition, the jet interaction occurs at jet firing nozzle planes with different strengths depending on the jet thrust of each nozzle.

The numerical simulation results provide a finite set of data points within the data space of the aerodynamic database. The data space that has not been covered by the simulations is filled with modeling data using symmetry

relations. Roll angles at each jet direction condition are extended to the range of $0° - 360°$. Then, the data for other jet direction conditions are extended by the results of the seven defined jet direction conditions. An example of a constructed aerodynamic database of jet interaction is shown in Figs. 4.3 and 4.4. The jet interaction normal force and pitching moment coefficients along the change of angle of attack and roll angle are plotted at $M = 3.0$ and MPR $= 1.02$. The jet interference aerodynamic coefficients are represented in the aerodynamic axis system. The moment coefficients are measured at the center of gravity of the missile, which is located behind the jet thruster. The peak jet interference at each jet direction case occurs when the main thruster, which is the largest opened nozzle, is located in the windward direction. The jet interference increases with an increase in angle of attack. The maximum jet interference is observed in the jet direction F1 at $\phi = 180^o$. The jet interaction acts in an unfavorable direction because it diminishes the normal forces and increases the pitching moments at the center of gravity. With this modeling strategy, the jet interaction aerodynamic database was developed from CFD simulations. The uncertainty level in the constructed database was evaluated through comparison with the wind tunnel test data.

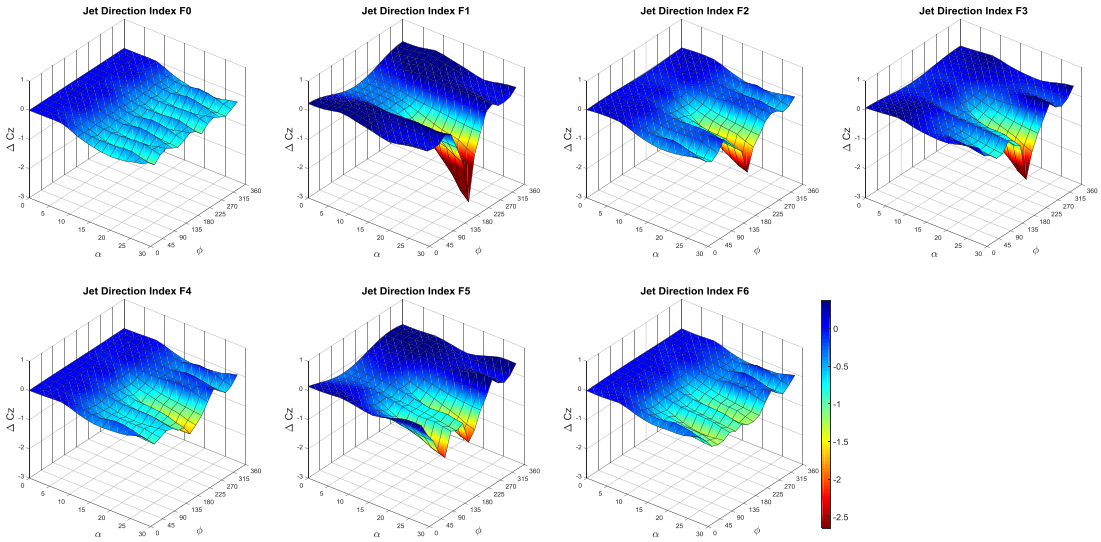

Figure 4.3: Jet interaction normal force coefficient for defined jet directions at $M = 3.0$, MPR $= 1.02$

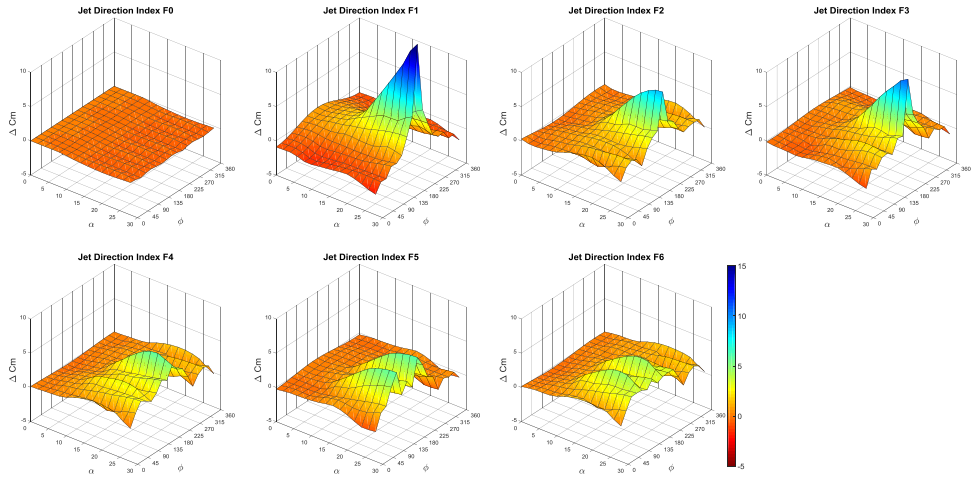

Figure 4.4: Jet interaction pitching moment coefficient for defined jet directions at $M = 3.0$, MPR $= 1.02$

4.5 Surrogate Modeling Method

Surrogate model can statistically approximate the relationship between a set of design variables and their responses, resulting in reducing the resource required for design, search and optimizations. Surrogate modeling is generally divided into two phases: 1) choosing an approximate experimental design in the region of interests, 2) constructing an approximation model with the obtained sample data [41].

A surrogate modeling using effective sampling and interpolation methods can reduce the number of simulations required to construct an aerodynamic database to a specified accuracy [18]. This approach was applied to the construction of the jet interaction aerodynamic database for the usage of interim approximated data. Since this design problem is based on deterministic computational data, modern design and analysis of computer experiment type methods were selected [42]. In this study, the Latin hypercube sampling (LHS) method was used to sample the training data, and the Kriging method was selected as an approximation model for the surrogate modeling.

4.5.1 Design of experiments

For the deterministic computer simulations, the modern Design of Experiments(DOE) methods such as orthogonal arrays and Latin Hypercube Designs with space filling manner are preferable to the classical DOE techniques since assumptions in classical DOE related to experimental error and non repeatability are not valid [43] [44]. In this study, Latin Hypercube Design method was used to select the sample data for surrogate modeling.

McKay et al introduced Latin Hypercube Sampling, or Latin Hypercube Design(LHD) [45]. This method demonstrates more accurate than random sampling and stratified sampling to estimate the means, variances and distribution functions of an output. Latin Hypercube Design samples can be obtained using following technique. If X denotes the $n \times d$ matrix in which we want to build sampling plan of n points in d dimension. The range of each design variable is divided into n intervals, and one observation on the input variable is made in each interval using random sampling. One of the observations on x_1 is randomly selected, matched with a randomly selected observations on x_2, and so on through x_d. These collectively constitute a design alternative X_1. One of the remaining observations on x_1 is then matched at random with one of the remaining observations on x_2, and so on, to get X_2. A similar procedure is followed for $X_3, \ldots, X_n$, which exhausts all observations and results in n LHD sample points.

4.5.2 Kriging predictor

The formulation of the Kriging model is presented here [46, 47, 47]. It was implemented using the DACE toolbox developed by Lophaven et al. [48]. Kriging models a responses as a combination of a regression function $f(\boldsymbol{x})$ and a Gaussian process Z.

$$Y(\boldsymbol{x}) = f(\boldsymbol{x}) + Z(\boldsymbol{x}). \tag{4.2}$$

The stocahstic part Z in Eq. 4.2 is assumed to be a zero-mean Gaussian process with a covariance function $\sigma^2\Psi$ defined by a process variance σ^2 and a correlation matrix Ψ.

Consider a set of n samples, $X = \left\{\boldsymbol{x}^1, \ldots, \boldsymbol{x}^n\right\}$ in d dimensions and associated function values, $\boldsymbol{y} = \left\{y^1, \ldots, y^n\right\}$. For ordinary Kriging, the regression part is equal to $\mathbf{1}\mu$, where $\mathbf{1}$ is a $n \times 1$ vector, and the stochastic process is mostly defined by the $n \times n$ correlation matrix Ψ as

$$\Psi = \begin{pmatrix} \psi(\boldsymbol{x}_1, \boldsymbol{x}_1) & \ldots & \psi(\boldsymbol{x}_1, \boldsymbol{x}_n) \\ \vdots & \ddots & \vdots \\ \psi(\boldsymbol{x}_n, \boldsymbol{x}_1) & \ldots & \psi(\boldsymbol{x}_n, \boldsymbol{x}_n) \end{pmatrix}. \tag{4.3}$$

The correlation function ψ is parameterized by hyperparameters θ. Among various correlation functions, a Gaussian correlation function is defined as follows:

$$\psi(\boldsymbol{x}, \boldsymbol{x}') = \exp\left(-\sum_{i=1}^{d} \theta_i |x_i - x_i'|^2\right). \tag{4.4}$$

A set of hyperparameter θ are identified by maximum likelihood estimation (MLE). In this study, the following likelihood method was used. The log of the marginal likelihood is given by,

$$\ln(\mathcal{L}) = -\frac{n}{2}\ln(2\pi) - \frac{n}{2}\ln(\sigma^2) - \frac{1}{2}\ln|\Psi| - \frac{1}{2\sigma^2}(\boldsymbol{y} - \mathbf{1}\mu)^{\mathsf{T}}\Psi^{-1}(\boldsymbol{y} - \mathbf{1}\mu). \tag{4.5}$$

The MLE of parameters can be obtained by the annihilation of the first derivatives of $\ln\mathcal{L}$ with respect to the parameters. The obtained MLE of μ and σ, i.e., $\hat{\mu} = (\mathbf{1}^{\mathsf{T}}\Psi^{-1}\boldsymbol{y})/(\mathbf{1}^{\mathsf{T}}\Psi^{-1}\mathbf{1})$ and $\hat{\sigma}^2 = \frac{1}{n}(\boldsymbol{y}-\mathbf{1}\mu)^{\mathsf{T}}\Psi^{-1}(\boldsymbol{y}-\mathbf{1}\mu)$, can be substituted back into Eq. 4.5 to give a concentrated log-likelihood

$$\ln(\mathcal{L}) \approx -\frac{n}{2}\ln(\hat{\sigma}^2) - \frac{1}{2}\ln|\Psi| \tag{4.6}$$

after leaving out constant terms. The concentrated log-likelihood function in Eq. 4.6 is nonlinear in θ. Thus, finding the MLE of θ is a problem of unconstrained nonlinear optimization and a global optimization scheme such as a genetic algorithm can be used.

The prediction of a new output $\hat{y}$ at a new input $\boldsymbol{x}$ should be consistent with the observed data and therefore with the correlation parameters. As a result, the new prediction can be found with the maximization of the likelihood of the sample and the prediction, given correlation parameters. To achieve this, the augmented output $\widetilde{\boldsymbol{y}} = [\boldsymbol{y}^\intercal, \hat{y}]^\intercal$ should be realizations of the same multivariate Gaussian distribution such that $Y(\boldsymbol{x}) \sim \mathcal{N}(\mu\mathbf{1}, \sigma^2\widetilde{\Psi})$ for ordinary Kriging. The augmented correlation matrix can be constructed:

$$\widetilde{\Psi} = \begin{pmatrix} \Psi & \psi \\ \psi^\intercal & 1 \end{pmatrix}. \tag{4.7}$$

The log-likelihood of the augmented data is

$$\ln(\mathcal{L}) = -\frac{n+1}{2}\ln(2\pi) - \frac{n+1}{2}\ln(\hat{\sigma}^2) - \frac{1}{2}\ln|\widetilde{\Psi}| - \frac{(\widetilde{\boldsymbol{y}} - \mathbf{1}\hat{\mu})^\intercal \widetilde{\Psi}^{-1}(\widetilde{\boldsymbol{y}} - \mathbf{1}\hat{\mu})}{2\hat{\sigma}^2}, \tag{4.8}$$

which reduces to the following log-likelihood function

$$\ln(\mathcal{L}) \approx -\frac{1}{2}\ln|\widetilde{\Psi}| - \frac{(\widetilde{\boldsymbol{y}} - \mathbf{1}\hat{\mu})^\intercal \widetilde{\Psi}^{-1}(\widetilde{\boldsymbol{y}} - \mathbf{1}\hat{\mu})}{2\hat{\sigma}^2}, \tag{4.9}$$

after the cancellation of terms that do not contain $\hat{y}$. Substituting in expressions for $\widetilde{\boldsymbol{y}}$ and $\widetilde{\Psi}$ gives

$$\ln(\mathcal{L}) \approx -\frac{1}{2\hat{\sigma}^2} \begin{pmatrix} \boldsymbol{y} - \mathbf{1}\hat{\mu} \\ \hat{y} - \hat{\mu} \end{pmatrix}^\intercal \begin{pmatrix} \Psi & \psi \\ \psi^\intercal & 1 \end{pmatrix}^{-1} \begin{pmatrix} \boldsymbol{y} - \mathbf{1}\hat{\mu} \\ \hat{y} - \hat{\mu} \end{pmatrix}. \tag{4.10}$$

Note that $\hat{\mu}$ and $\hat{\sigma}^2$ are treated as known since they are estimated previously. With the help of the partitioned inverse method, $\widetilde{\Psi}^{-1}$ can be expressed in terms

of Ψ and ψ as follows

$$\widetilde{\Psi}^{-1} = \begin{pmatrix} \Psi^{-1} + \Psi^{-1}\psi(1-\psi^{\intercal}\Psi^{-1}\psi)^{-1}\psi^{\intercal}\Psi^{-1} & -\Psi^{-1}\psi(1-\psi^{\intercal}\Psi^{-}1\psi)^{-1} \\ -(1-\psi^{\intercal}\Psi^{-1}\psi)^{-}1\psi^{\intercal}\Psi^{-1} & (1-\psi^{\intercal}\Psi^{-1}\psi)^{-1} \end{pmatrix}. \tag{4.11}$$

This can be substituted into Eq.4.10 and terms without $\hat{y}$ removed to give

$$\ln(\mathcal{L}) \approx -\left(\frac{1}{2\hat{\sigma}^2(1-\psi^{\intercal}\Psi^{-1}\psi)}\right)(\hat{y}-\hat{\mu})^2 + \left(\frac{\psi^{\intercal}\Psi^{-1}(\boldsymbol{y}-\mathbf{1}\hat{\mu})}{\hat{\sigma}^2(1-\psi^{\intercal}\Psi^{-1}\psi)}\right)(\hat{y}-\hat{\mu}). \tag{4.12}$$

The MLE of $\hat{y}$ can be found with the derivative of $\ln(\mathcal{L})$ as shown below,

$$\hat{y}(\boldsymbol{x}) = \hat{\mu} + \psi^{\intercal}\Psi^{-1}(\boldsymbol{y}-\mathbf{1}\hat{\mu}). \tag{4.13}$$

4.6 Surrogate Modeling of Jet Interaction

4.6.1 Jet interaction modeling and evaluation

The construction of the jet interaction aerodynamic database modeling problem is defined by a response y of the jet interaction aerodynamic coefficients $\Delta C_{w_{JI}}$ with an input x of six jet interaction parameters in Eq. 4.14. The surrogate model, $\widetilde{f}$, can be found through Kriging modeling of the CFD simulation results at the sampled data x for each aerodynamic coefficient.

$$\begin{aligned} \text{Input} \quad x: \quad & M, H, \alpha_t, \phi, |F|, \theta_j \in \mathbb{R}^6 \\ \text{Output} \quad y: \quad & \Delta C_{w_{JI}} \in \mathbb{R}^6 \quad where, w = x, y, z, l, m, n \\ & y = \underbrace{f(x)}_{\text{CFD}} \Longrightarrow \hat{y} = \underbrace{\widetilde{f}(x)}_{\text{surrogate}} \end{aligned} \tag{4.14}$$

This design problem can be rearranged at the reduced design space in Table.4.3.

$$\begin{aligned} \text{Input} \quad x: \quad & M, H, \alpha_t, \phi^i \in \mathbb{R}^4 \\ \text{Output} \quad y: \quad & \Delta C_{w_{JI}} \in \mathbb{R}^4 \\ \text{at given } i^{th} \text{ case} & \begin{cases} \hat{y}_1^i = \widetilde{g}_1^i(x) \\ \quad \vdots \\ \hat{y}_6^i = \widetilde{g}_6^i(x) \end{cases} \end{aligned} \tag{4.15}$$

The size of the problem was reduced from six models with seven dimensions to 6×7 models with four dimensions. The surrogate model, $\widetilde{g}$, at each i^{th} jet direction case can be obtained by the Kriging method. In this design problem, five different sampling points were chosen for the LHS method. The quality of the constructed surrogate model was evaluated through a model testing process. Two measurement values were used for the model test, the root mean squared error (RMSE) and the correlation coefficient R^2, which are defined as

$$\text{RMSE} = \sqrt{\frac{\sum_{i=1}^{n_t}(y_i - \hat{y}_i)}{n_t}}, \tag{4.16}$$

$$R^2 = 1 - \text{SSE/SST} = 1 - \frac{\sum_{i=1}^{n_t}(y_i - \hat{y}_i)^2}{\sum_{i=1}^{n_t}(y_i - \bar{y_i})^2} \tag{4.17}$$

where n_t is size of test data. The R^2 value requires a large number n_t, which is not practical in a general surrogate model evaluation. However, this value is selected as a supplemental measurement in this study because it can satisfactorily indicate the goodness of the model, and a sufficiently large number of data are gathered from the CFD-based modeling.

4.6.2 Surrogate modeling of jet interaction results

The surrogate modeling and its evaluation were performed respectively at each jet direction condition and aerodynamic coefficient component with varying sample size. The RMSE was calculated with an additional 50 sample points, and R^2 was calculated for the rest of data points except the data used for the modeling.

The modeling test results are shown in Figs. 4.5 – 4.12 for jet direction F0, F1, F3 ,and F5. It can be observed that the convergence characteristics of the RMSE and R^2 are different for each model and the force coefficients achieve faster RMSE convergence than the moment coefficients. The R^2 values of the normal force and pitching moment coefficients converge faster than those of the side force and yawing moment coefficients. These results imply that the nonlinearity of the side force and yawing moment coefficients are considerably higher. The results of the axial force and rolling moment coefficients are not presented here because their jet interaction contribution is small compared with the nominal state aerodynamic coefficients. The general error converges when the number of samples was increased from 50 to 250. The convergence criteria were selected based on the previous uncertainty assessment of the computational simulations where the RMSE was less than 0.1 for the force coefficients and was less than 0.5 for the moment coefficients. With these criteria, the sampling points were determined for each jet direction condition. Table 4.6 shows the final model test results for each case, listing the number of sample points, their minimum and maximum RMSE, and minimum R^2. The average of minimum R^2 is approximately 0.81, which indicates a surrogate with reasonable predictive capabilities [46].

Table 4.6: Final results for the surrogate model of the jet interaction

Jet direction index	F0	F1	F2	F3	F4	F5	F6
Sample points	200	250	250	250	200	250	250
Min. RMSE	0.0174	0.0522	0.0760	0.1000	0.0975	0.0718	0.0779
Max. RMSE	0.3985	0.4633	0.4965	0.4901	0.4820	0.4834	0.4634
Min. R^2	0.8018	0.8465	0.8507	0.7826	0.7923	0.8289	0.8082

The contour plot of the constructed surrogate models with 250 samples at jet direction F5 is shown in Figs. 4.13 – 4.18. It can be observed that the surrogate model satisfactorily captures the nonlinear behavior of the response surfaces in all of the design space. A set of 1,650 sampling points was used to design the surrogate model at the seven jet direction conditions, and a set of 350 sampling points was selected for the model evaluation. It is approximately 22% of the full factorial sampling data, which imply a significant reduction of the computations in constructing the jet interaction aerodynamic database.

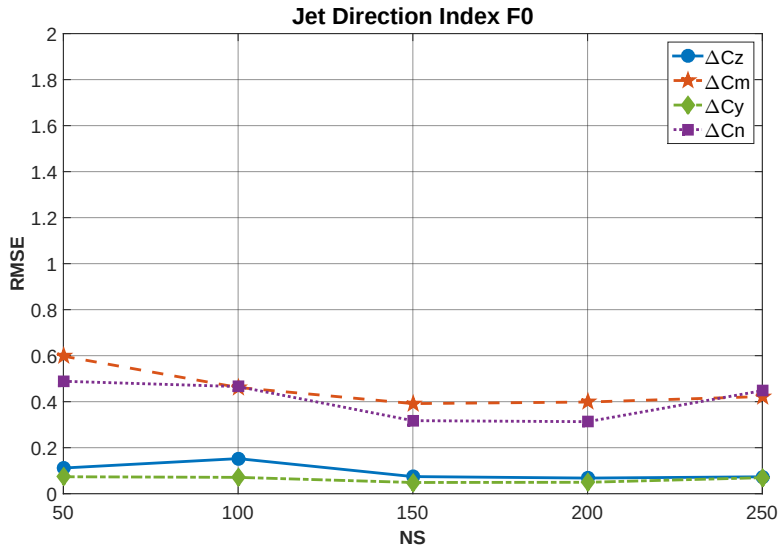

Figure 4.5: Evolution of RMSE with sampling size(F0)

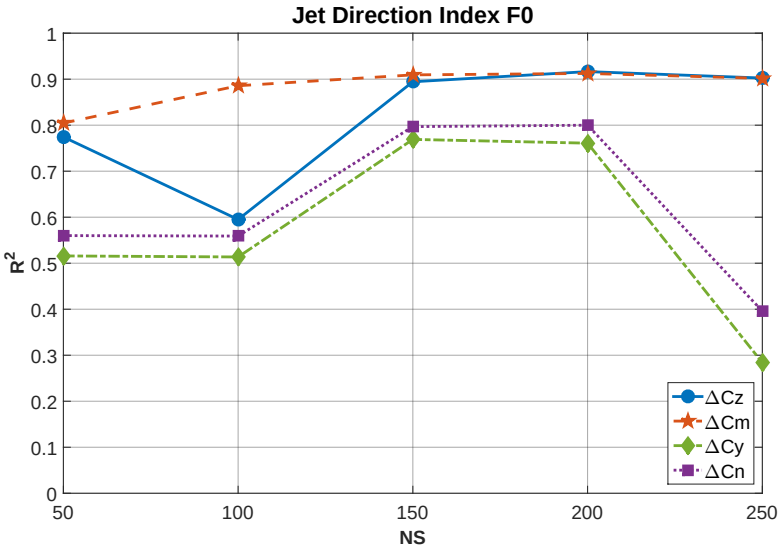

Figure 4.6: Evolution of R^2 with sampling size(F0)

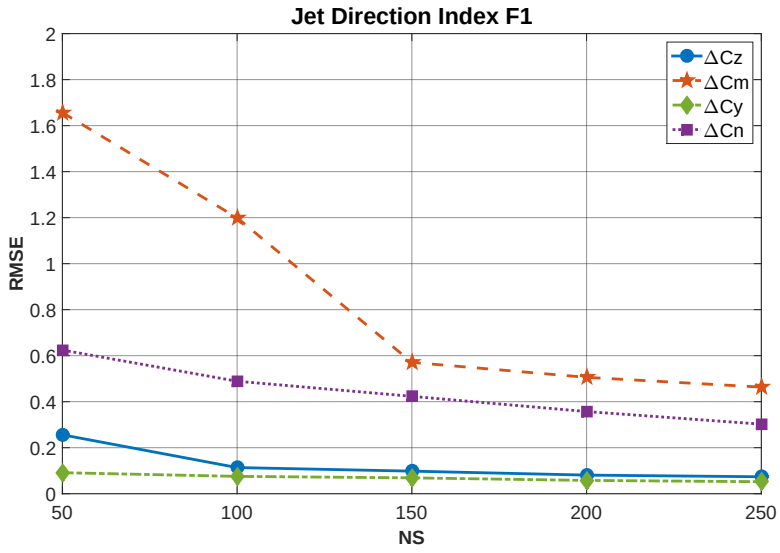

Figure 4.7: Evolution of RMSE with sampling size(F1)

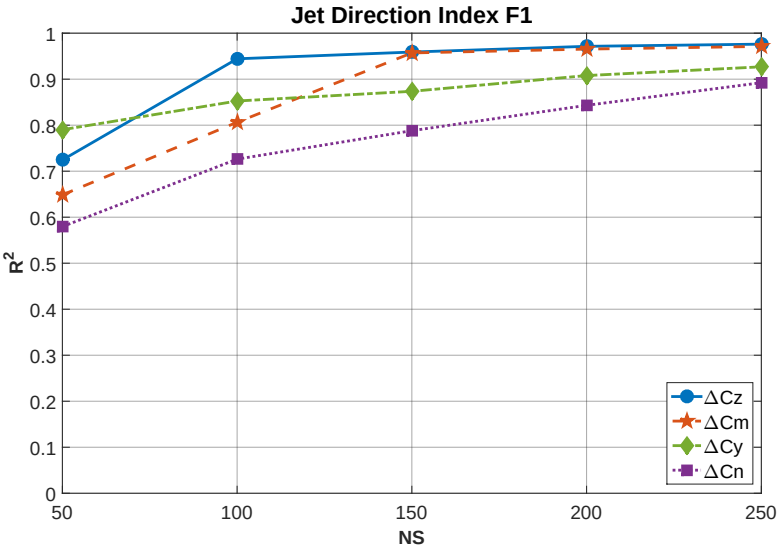

Figure 4.8: Evolution of R^2 with sampling size(F1)

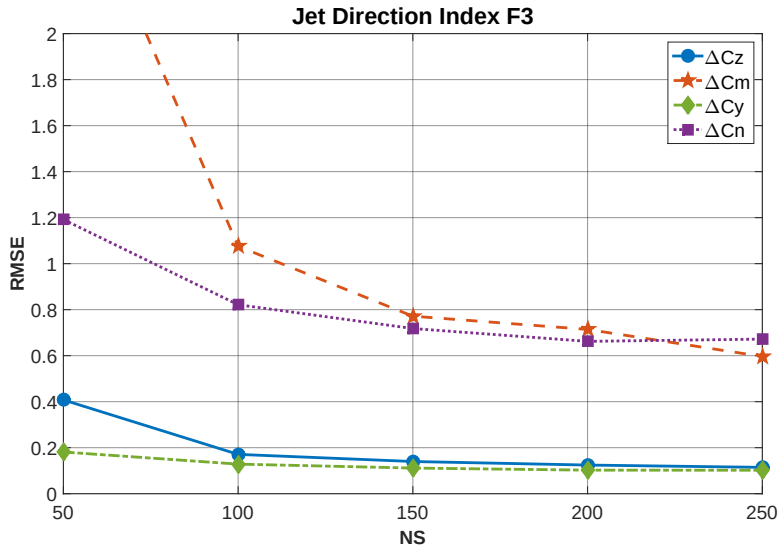

Figure 4.9: Evolution of RMSE with sampling size(F3)

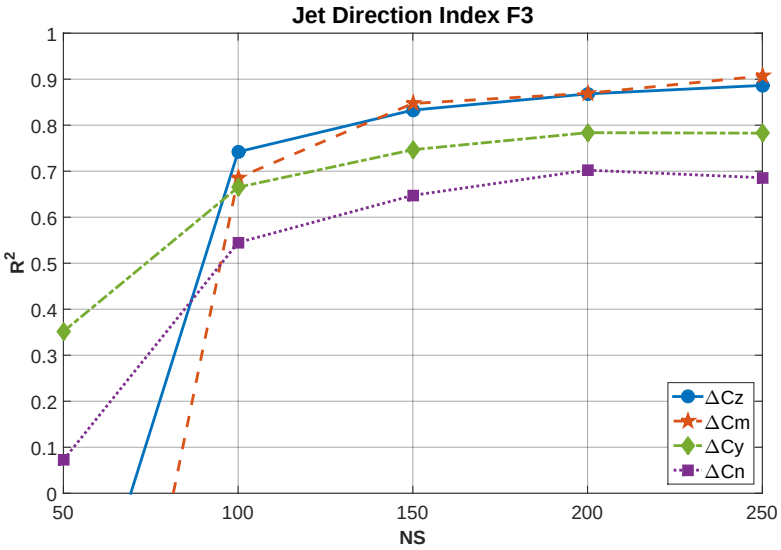

Figure 4.10: Evolution of R^2 with sampling size(F3)

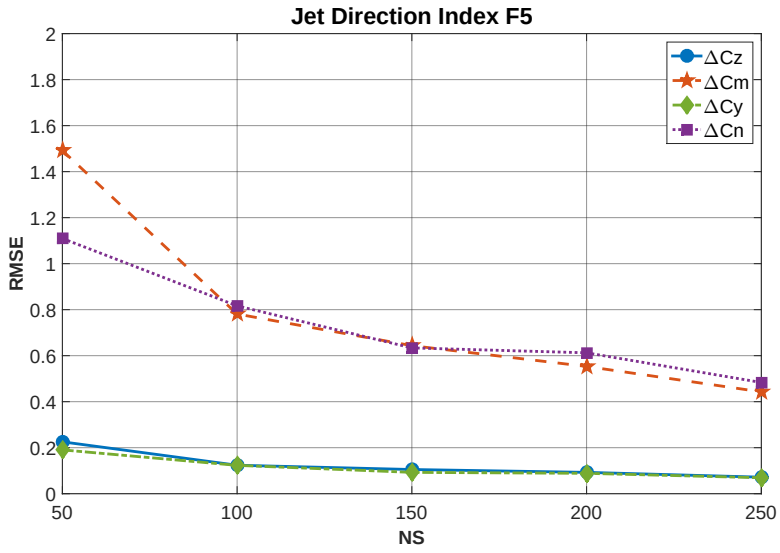

Figure 4.11: Evolution of RMSE with sampling size(F5)

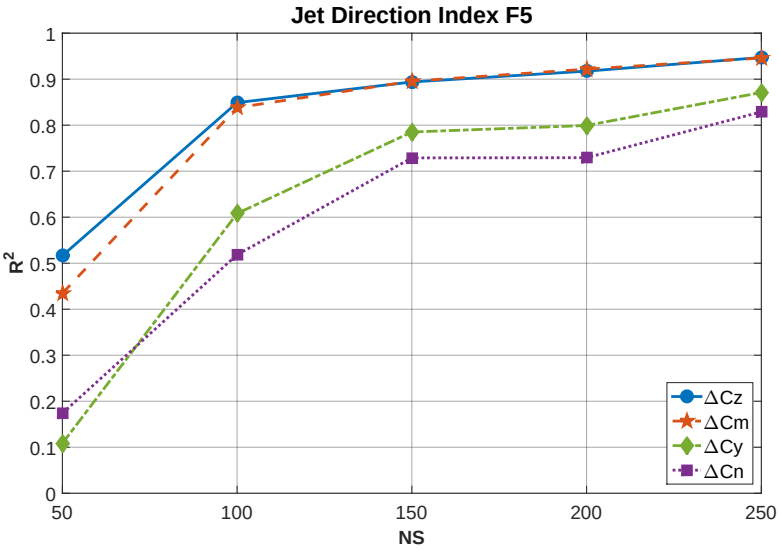

Figure 4.12: Evolution of R^2 with sampling size(F5)

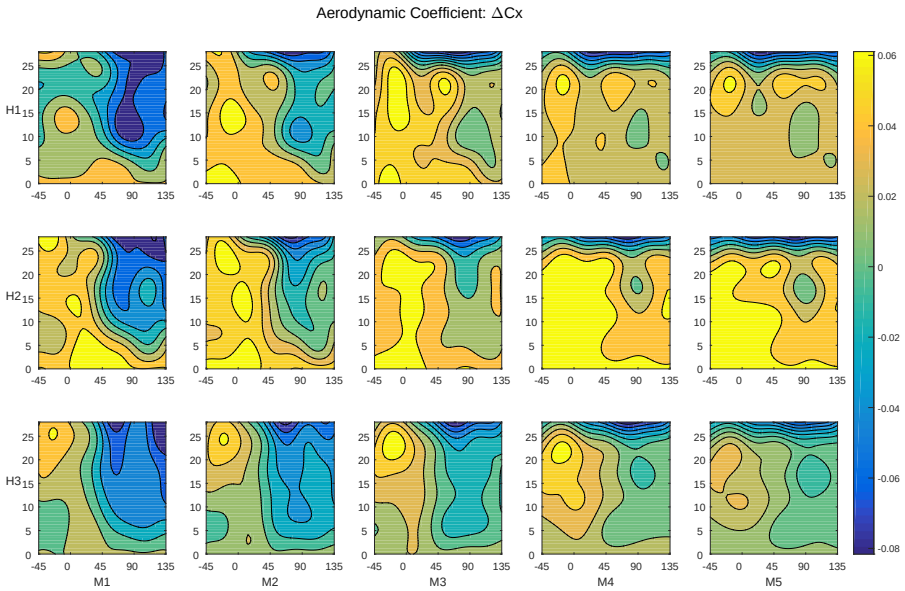

Figure 4.13: Surrogate modeling results with 250 samples at jet direction F5: ΔCx

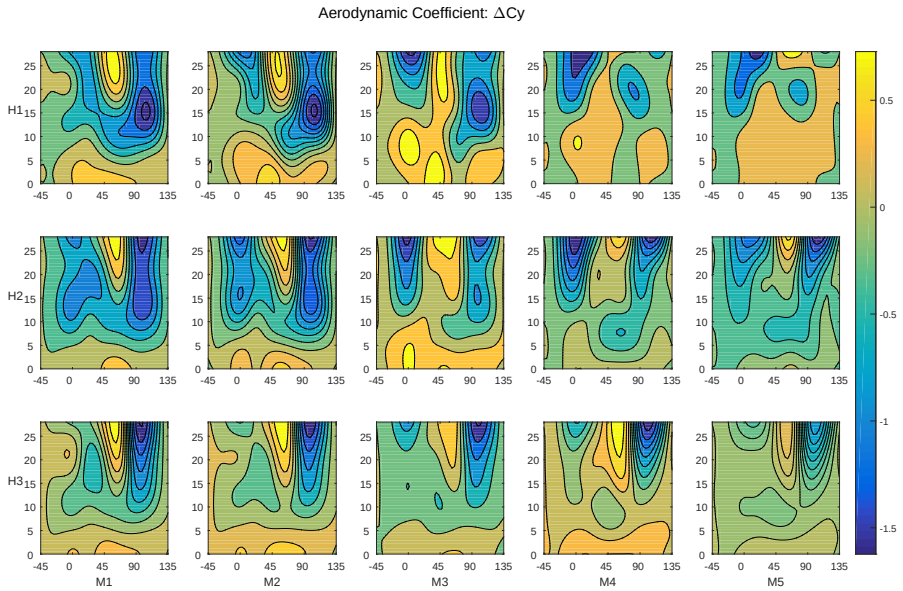

Figure 4.14: Surrogate modeling results with 250 samples at jet direction F5: ΔCy

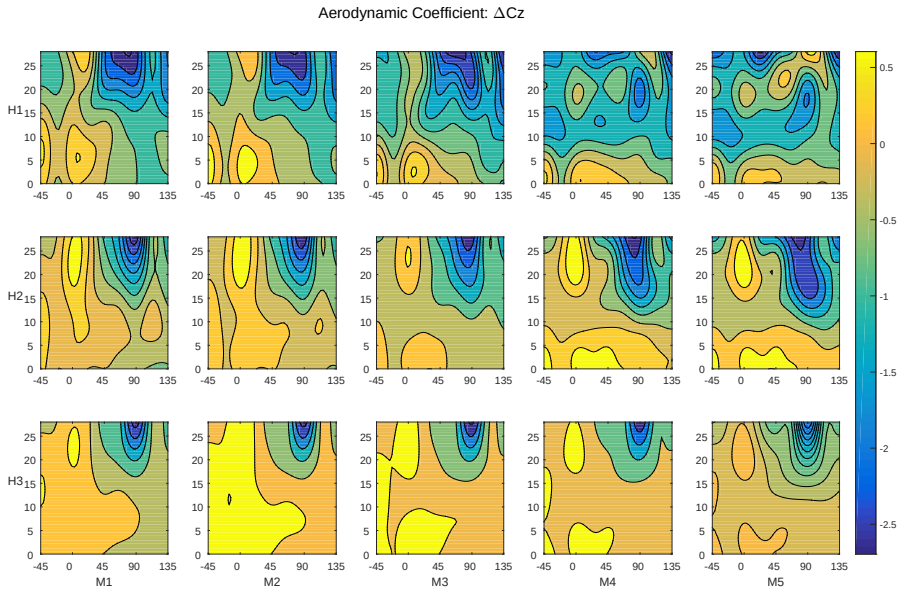

Figure 4.15: Surrogate modeling results with 250 samples at jet direction F5: ΔCz

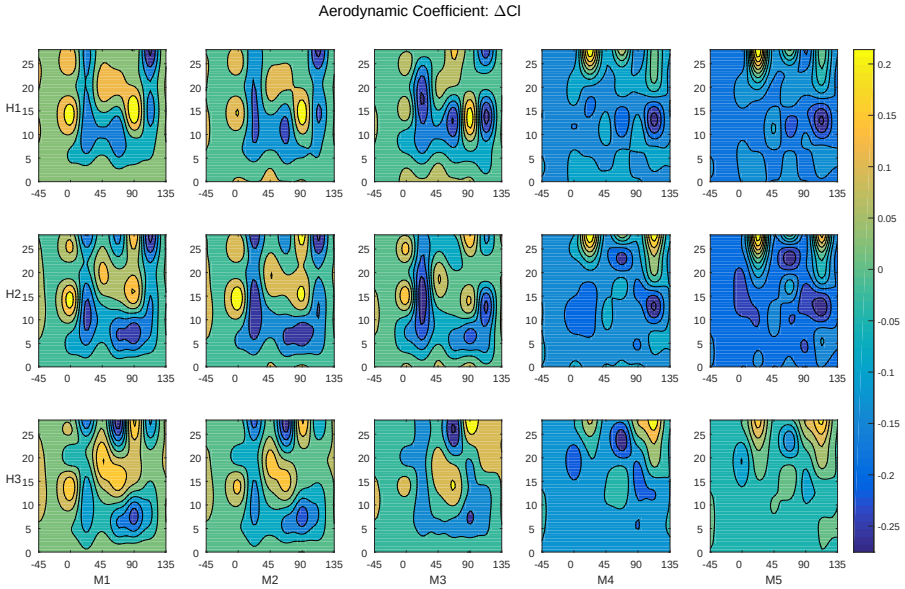

Figure 4.16: Surrogate modeling results with 250 samples at jet direction F5: ΔCl

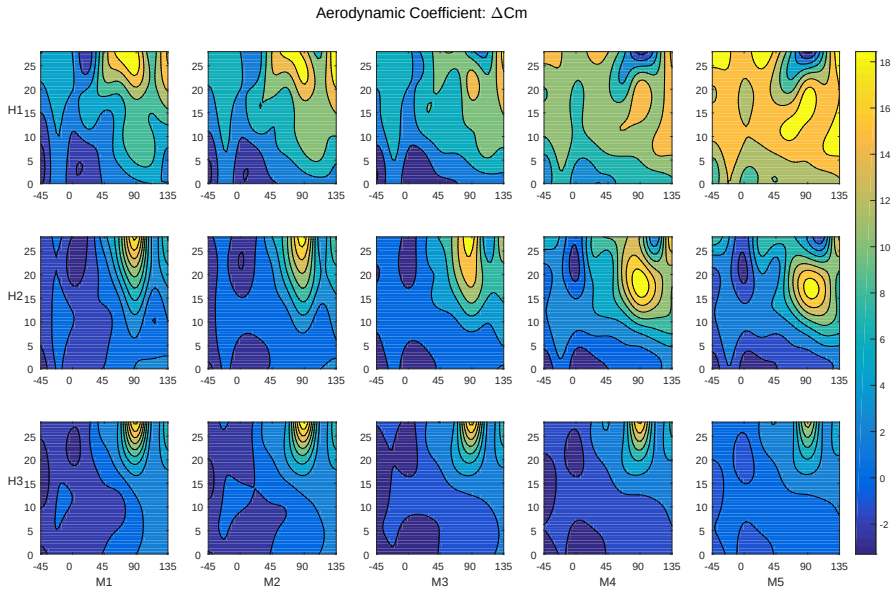

Figure 4.17: Surrogate modeling results with 250 samples at jet direction F5: ΔCm

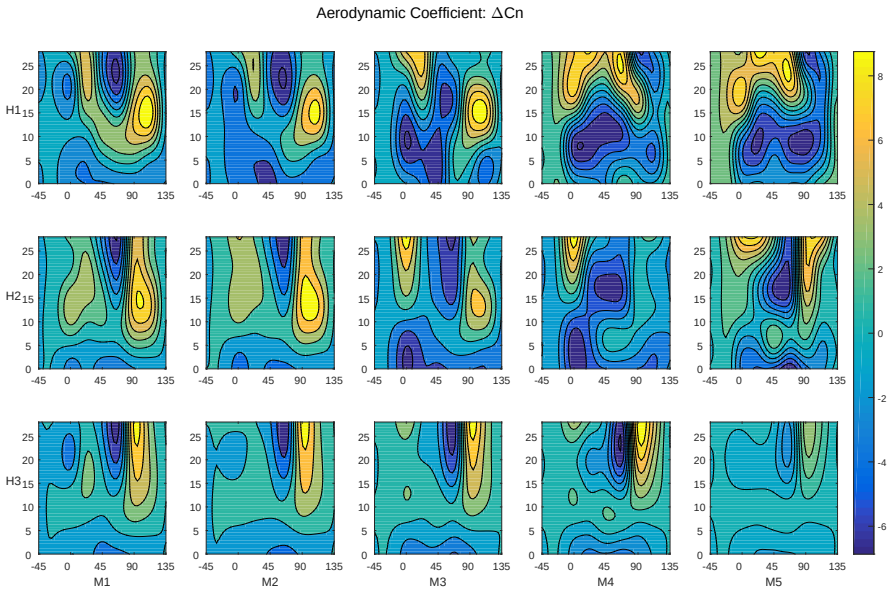

Figure 4.18: Surrogate modeling results with 250 samples at jet direction F5: ΔCn

Chapter 5

Assessment of Jet Interaction Modeling Results

Post-flight data analysis is essential activities to validate aerodynamic model and to get more accurate mathematical models for the purpose of simulation, stability analysis, and control system design and simulation [49]. The programmed flight test was successfully conducted for the missile system in this study. One of the major objectives of the flight test was to check the performance of the continuous type side-jet during the mission. A post-flight test analysis was performed to evaluate the jet interaction aerodynamic database with the measurement data from the test.

5.1 Post Flight Analysis for Jet Interaction Database Identification

The general procedure of the post-flight analysis for identification of the jet interaction model is illustrated in Fig. 5.1. Measured linear and angular accelerations are used to reconstruct flight-derived aerodynamic coefficients. Velocity and attitude angle of the vehicle are used to look up the 6-DoF aerodynamic database in the flight conditions. Then, the flight-derived aerodynamic

coefficients are compared with those interpolated from the 6-DoF model. The side-jet thrust and operating direction are calculated from the control angle of each side-jet nozzle. They can be used to evaluate the assessment of the jet interaction aerodynamic database. The aerodynamic coefficients from the measured data are computed through the following equations of motion:

$$\begin{aligned} C_x &= (m \times a_x)/(qS_{ref}) \\ C_y &= (m \times a_y - T_y)/(qS_{ref}) \\ C_z &= (m \times a_z - T_z)/(qS_{ref}) \end{aligned} \tag{5.1}$$

$$\begin{aligned} C_l &= \{I_{xx}\dot{p} - (I_{yy} - I_{zz})qr\}/(qS_{ref}L_{ref}) \\ C_m &= \{I_{yy}\dot{q} - (I_{zz} - I_{xx})pr - T_z(x_{sj} - x_{cg})\}/(qS_{ref}L_{ref}) \\ C_n &= \{I_{zz}\dot{r} - (I_{xx} - I_{yy})pq - T_y(x_{sj} - x_{cg})\}/(qS_{ref}L_{ref}) \end{aligned} \tag{5.2}$$

Where q is the dynamic pressure, S_{ref} is the reference area, L_{ref} is the reference length and x_{sj} is the side-jet location. Measured acceleration data are converted to the body-axis coordinate at the center of gravity [50]. Atmospheric properties and wind data are measured from a radiosonde sensor during the flight test and they supplement the post flight analysis.

The flight test analysis to evaluate jet interaction was performed during the operation of side-jet. The side-jet direction and jet force magnitude while jet thrusters were firing are shown in Figs. 5.2 and 5.3. Zero jet force magnitude means an idle state of side-jet. The jet thrust is modeled through the ground test and corrected at flight environments for the post flight analysis.

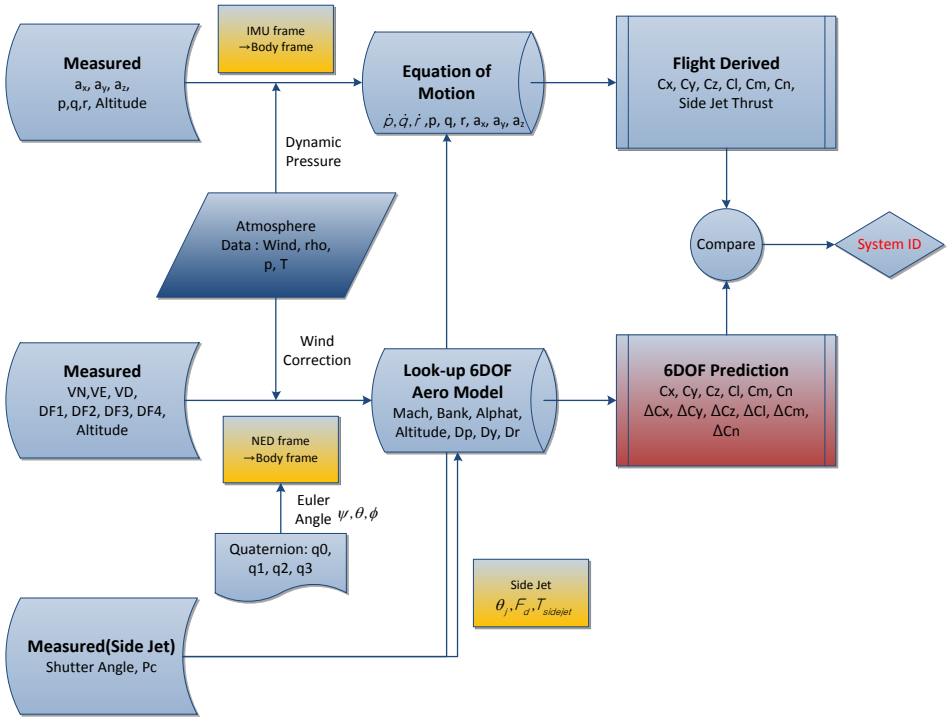

Figure 5.1: Schematic of the procedure for aerodynamic model identifications

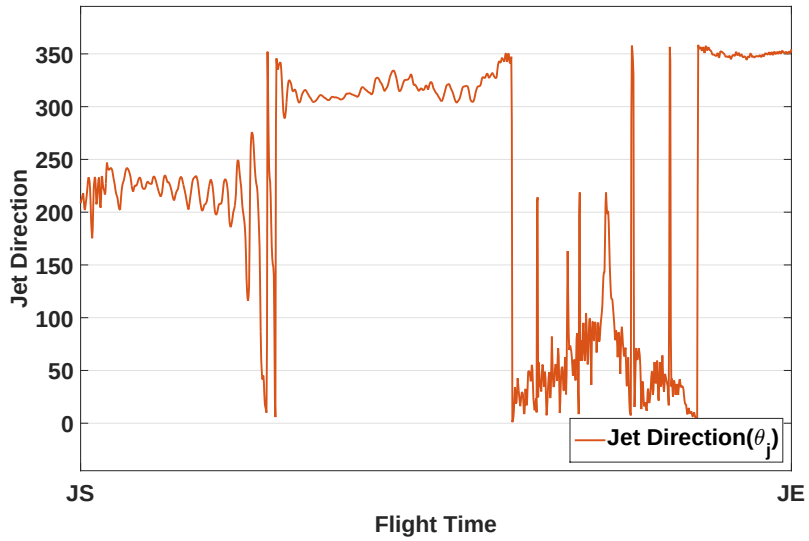

Figure 5.2: Change of jet direction θ_j during the flight test

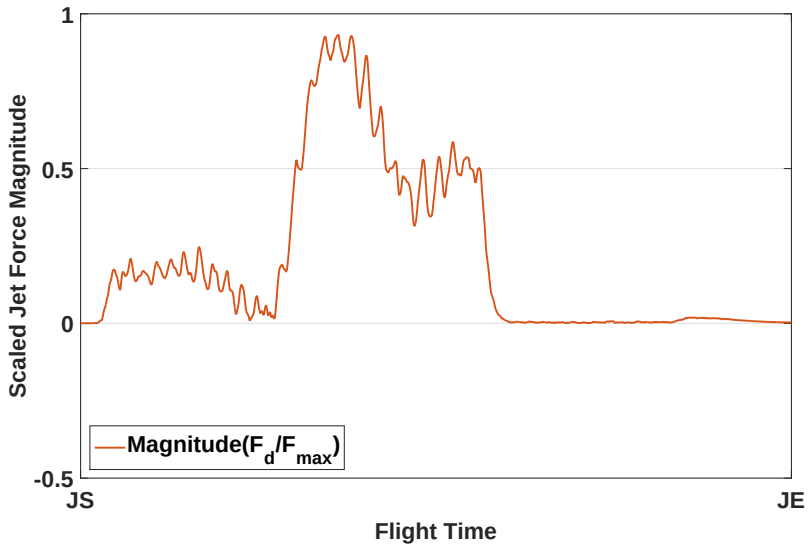

Figure 5.3: Change of jet force magnitude during the flight test

5.2 Assessment of Jet Interaction Database

The flight reconstructed force and moment coefficients from the post-flight analysis were compared to the aerodynamic database during the side-jet operation. The flight conditions were derived from the measurements: Mach number is about 3.0, total angle of attack is between 0° and 20°, roll angle is between 270° and 315°, and altitude is between H2 and H3.

Figures 5.4 and 5.5 show a comparison of the normal and side force coefficients from the flight-reconstructed data and the aerodynamic database as well as the jet interaction. The gray regions in the plot indicate the uncertainty level of the jet interaction aerodynamic coefficients. The two constructed jet interaction aerodynamic databases, the CFD-based model and the surrogate model, are compared as well. It is shown that the both databases exhibit very similar behavior with respect to the flight envelope. Because the measured acceleration contains jet force, the contribution of side-jet thrust was extracted in the flight-derived aerodynamic force estimations. The jet interaction effects were calculated from the jet interaction aerodynamic database and added to the resultant aerodynamic coefficients. The aerodynamic coefficients agree closely with the flight-derived data, which also means that the jet interaction database satisfactorily predicts the jet interaction effects. The approximate order of magnitude of discrepancy in the force coefficient was less than 10% in the analysis.

Figures 5.6 and 5.7 show a comparison of the pitching and yawing moment coefficients at the center of gravity between the flight-derived data and aerodynamic database during the jet thruster operation period in the flight test. The overall trends of the pitching and yawing moment changes in the aero-

dynamic database agree closely with the flight test results. For the conditions at which the side-jet was operated at $\theta_j = 225°$, significant differences exist between the database and the reconstructed pitching moment values. These differences could be because of the fact that the inaccuracy increases at high angle of attack conditions owing to the strong jet interaction between the jet flow and body cross flow; thus, the uncertainty was increased in the prediction of moments from the flight test. However, the differences in change of the center of pressure (ΔXcp) were less than 1 caliber. The total jet interaction forces $(\Delta Cy^2 + \Delta Cz^2)^{1/2}$ are compared with the side-jet thrust coefficient in Fig. 5.8. From this figure it can be seen that the jet interaction effect is remarkable and it is even larger than the side-jet thrust at some operating conditions. Additionally, to see the clearer contrast between the two jet interaction databases, the approximated database is plotted against to the actual CFD-based database in Figs. 5.9 – 5.12. It is shown that the surrogate model is a good match with the CFD-based model. The modeling error of the moment coefficients in the surrogate model is larger than that of the force coefficients.

From the post-flight analysis, the jet interaction aerodynamic database constructed with CFD simulations was successfully evaluated at the flight conditions. It satisfactorily represents the behavior of the jet interaction effects within a reasonable error level. The results show that the change of aerodynamic coefficients owing to jet interaction has a significant impact on aerodynamic data.

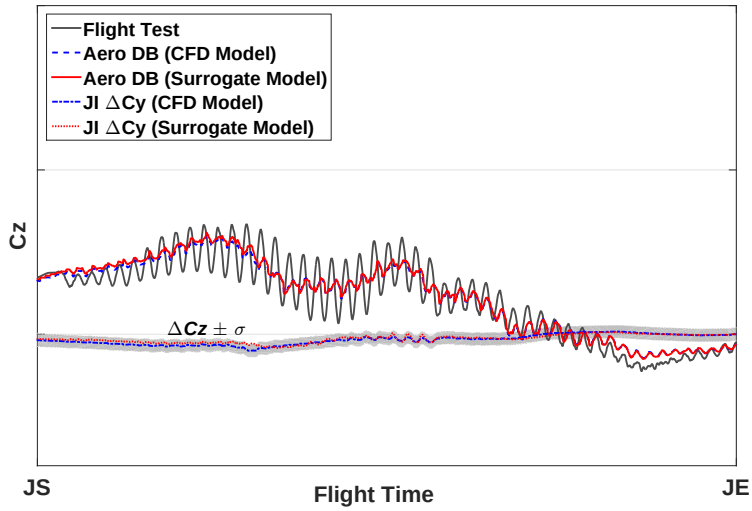

Figure 5.4: Comparison of normal force coefficient during the flight test

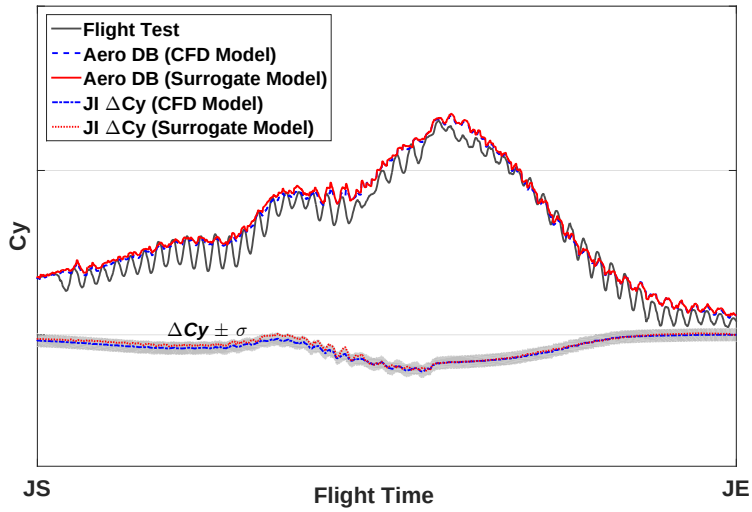

Figure 5.5: Comparison of side force coefficient during the flight test

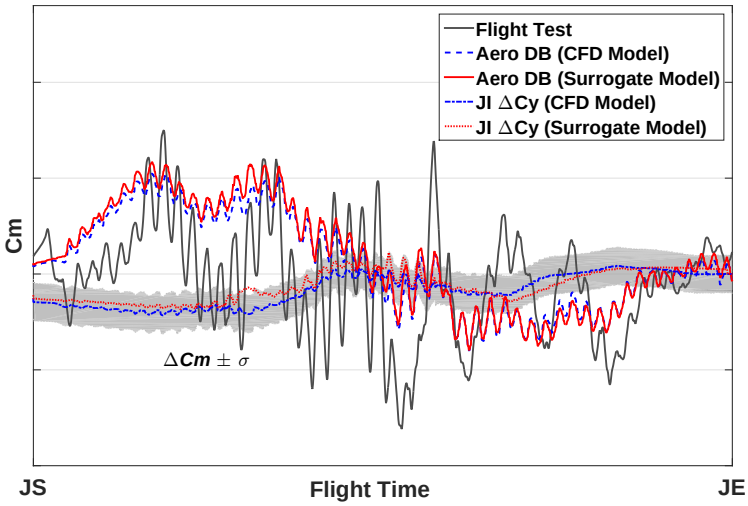

Figure 5.6: Comparison of pitching moment coefficient during the flight test

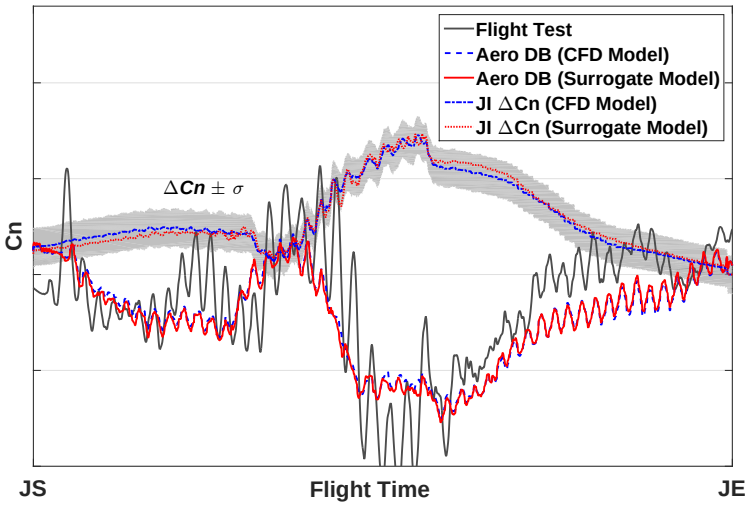

Figure 5.7: Comparison of yawing moment coefficient during the flight test

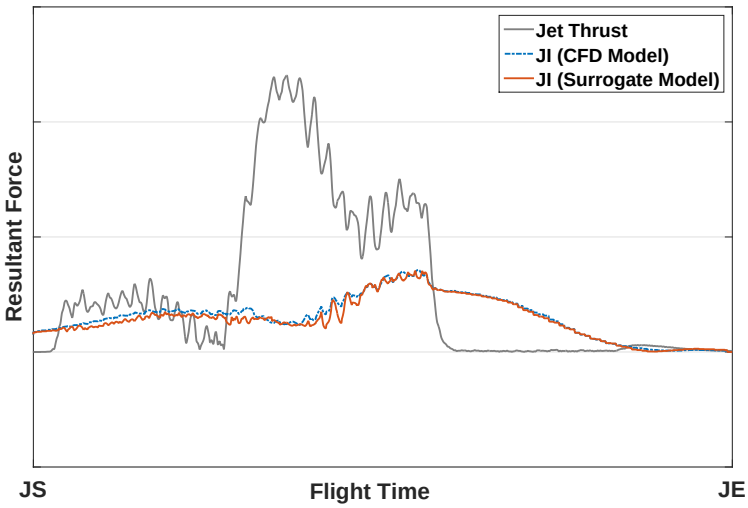

Figure 5.8: Comparison of jet interaction effect with the side-jet thrust

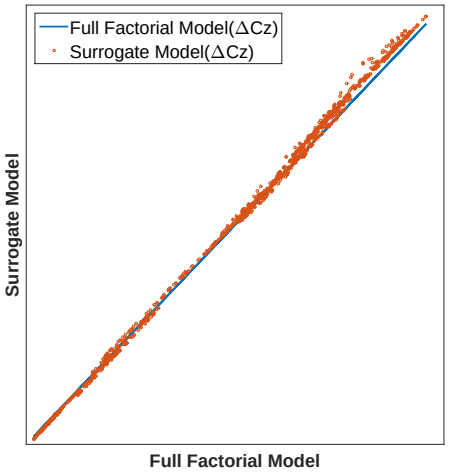

Figure 5.9: Comparison of two jet interaction databases during the flight test: ΔC_z

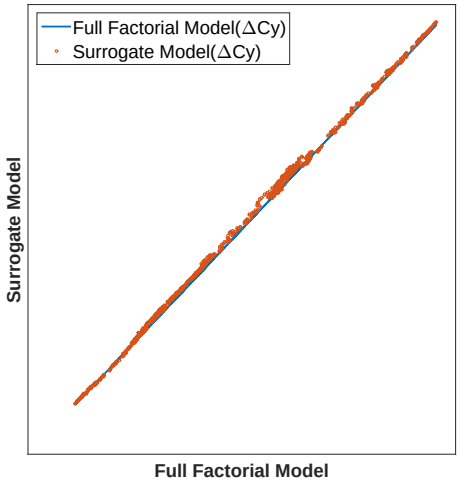

Figure 5.10: Comparison of two jet interaction databases during the flight test: ΔC_y

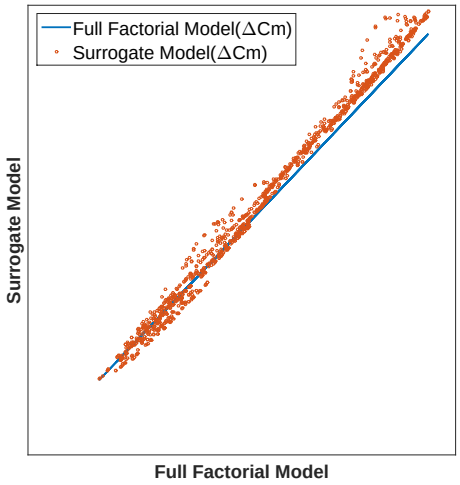

Figure 5.11: Comparison of two jet interaction databases during the flight test: ΔC_m

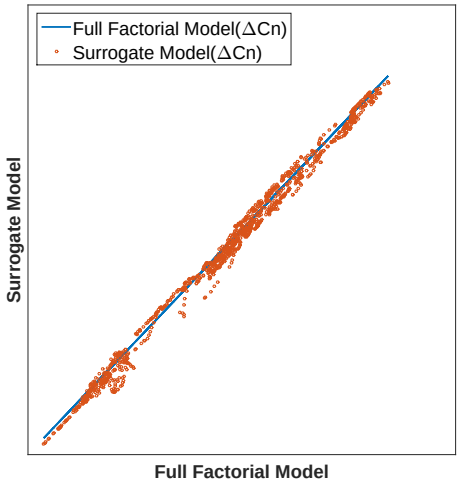

Figure 5.12: Comparison of two jet interaction databases during the flight test: ΔC_n

Chapter 6

Conclusion

An extensive numerical simulation was conducted for a supersonic missile equipped with a continuous type side-jet thruster, to gain an understanding of complex jet interaction phenomena and to obtain aerodynamic jet interaction data. The simulation was performed using the unstructured CFD solver. The uncertainty level of the jet interaction simulation data was evaluated from the differences between the cold gas CFD simulation results and the wind tunnel test data. The root mean square (RMS) of the force coefficient differences was less than 0.1, while that of the moment coefficient differences was less than 0.5. The maximum error of the change of the center of pressure (ΔX_{cp}) owing to the jet interaction was measured as less than 1 caliber.

The detailed flow structures of jet interaction such as shock induced separation of boundary layer, barrel shock of jet flow and the separation wake region, are captured well. From the continuous type side-jet simulations for the various flow and jet conditions, the maximum jet interference conditions were found and jet interaction characteristics were investigated. The side jet direction with nozzle combinations for continuous side-jet thrusters was adopted to analyze jet interaction.

The construction of the jet interaction aerodynamic database for missiles

with continuous type side-jet thrusters was performed using CFD simulation. Three-dimensional jet flow simulation was conducted using the unstructured CFD solver for the database modeling. All jet interaction effects were accounted for as incremental terms of the basic aerodynamic database. The design space of the database was reduced by 90% through an efficient modeling strategy of the defined jet direction.

Two modeling approaches were used to construct the jet interaction aerodynamic database. One was the CFD-based modeling with the full factorial sampling and the other was the surrogate modeling with Kriging methods. Approximately 22% data of the CFD-based model were selected for the surrogate modeling and evaluation.

The accuracy of the two resulting aerodynamic databases was assessed through the identification of jet interaction effects from the flight test results. Despite some discrepancy in moment coefficients, the overall aerodynamic coefficients as well as the jet interaction effect agreed closely with the flight-derived data. For the force coefficients, the difference between the flight data and the database was less than 10%. This result confirms that a reasonable aerodynamic database of jet interaction can be constructed for the continuous type side-jet thruster-controlled missile using only CFD data. The surrogate model was found to have a reasonable performance compared with the CFD-based model within acceptable uncertainty levels. The use of surrogate modeling to build the jet interaction aerodynamic database drastically reduced the number of computations with a successful approximation of the complex jet interaction behavior. It is expected that the surrogate modeling method will play a significant role in jet interaction analysis in the early stage of the system development

cycle. Additional efforts will be exerted to improve the constructed jet interaction aerodynamic database through a post-flight test analysis of subsequent planned flight tests.

In this study, one surrogate modeling method is applied to construct jet interaction aerodynamic database, and further efforts to model by using GEK (Gradient Enhanced Kriging) method or adaptive sampling method should be performed to improve modeling efficiency as future research. In addition, studies on effective model evaluation methods such as cross validation and relative error should be carried out.

Appendix A

Extension Rules of Jet Directions

The seven jet directions for $\theta_j = 0°$, $22.5°$, and $45°$ are selected to reduce the number of simulations for constructing the jet interaction aerodynamic database. The minimum roll angle conditions are chosen for each jet direction by using symmetry relation; F0($\phi_1 - \phi_5$), F1($\phi_1 - \phi_9$), F2($\phi_1 - \phi_9$), F3($\phi_1 - \phi_{16}$), F4($\phi_1 - \phi_{16}$), F5($\phi_1 - \phi_9$), and F6($\phi_1 - \phi_9$). Figure A.1 shows the selected roll angle conditions at the seven jet directions and a total of 73 combinations are derived. The remaining jet conditions, $\theta_j = 67.5° - 337.5°$, can be extended by the mirror symmetry relationship shown in Table A.1.

Table A.1: Extension rules of jet interaction

θ_j [deg]	$F_{\max}/T_{\max}$	ϕ [deg] (interval of 22.5°)	sources
0°	1.0	0° – 180°	(F1, $\phi_1 - \phi_9$)
0°	1.0	202.5° – 337.5°	(F1, $\phi_1 - \phi_9$), mirrored
0°	0.5	0° – 180°	(F2, $\phi_1 - \phi_9$)
0°	0.5	202.5° – 337.5°	(F2, $\phi_1 - \phi_9$), mirrored
22.5°	1.0	0° – 337.5°	(F3, $\phi_1 - \phi_{16}$)
22.5°	0.5	0° – 337.5°	(F4, $\phi_1 - \phi_{16}$)

Table A.1: Extension rules of jet interaction

θ_j [deg]	$F_{\max}/T_{\max}$	ϕ [deg] (interval of 22.5°)	sources
45°	1.0	45° − 135°	(F5, $\phi_1 - \phi_9$)
45°	1.0	22.5°, 157.5° − 360°	(F5, $\phi_1 - \phi_9$), mirrored
45°	0.5	45° − 135°	(F6, $\phi_1 - \phi_9$)
45°	0.5	22.5°, 157.5° − 360°	(F6, $\phi_1 - \phi_9$), mirrored
67.5°	1.0	0° − 337.5°	(F3, $\phi_1 - \phi_{16}$), mirrored
67.5°	0.5	0° − 337.5°	(F4, $\phi_1 - \phi_{16}$), mirrored
90°	1.0	0° − 337.5°	(F1, $\phi_1 - \phi_9$), mirrored
90°	0.5	0° − 337.5°	(F2, $\phi_1 - \phi_9$), mirrored
112.5°	1.0	0° − 337.5°	(F3, $\phi_1 - \phi_{16}$), mirrored
112.5°	0.5	0° − 337.5°	(F4, $\phi_1 - \phi_{16}$), mirrored
135°	1.0	0° − 337.5°	(F5, $\phi_1 - \phi_9$), mirrored
135°	0.5	0° − 337.5°	(F6, $\phi_1 - \phi_9$), mirrored
157.5°	1.0	0° − 337.5°	(F3, $\phi_1 - \phi_{16}$), mirrored
157.5°	0.5	0° − 337.5°	(F4, $\phi_1 - \phi_{16}$), mirrored
180°	1.0	0° − 337.5°	(F1, $\phi_1 - \phi_9$), mirrored
180°	0.5	0° − 337.5°	(F2, $\phi_1 - \phi_9$), mirrored
202.5°	1.0	0° − 337.5°	(F3, $\phi_1 - \phi_{16}$), mirrored
202.5°	0.5	0° − 337.5°	(F4, $\phi_1 - \phi_{16}$), mirrored
225°	1.0	0° − 337.5°	(F5, $\phi_1 - \phi_9$), mirrored
225°	0.5	0° − 337.5°	(F6, $\phi_1 - \phi_9$), mirrored
247.5°	1.0	0° − 337.5°	(F3, $\phi_1 - \phi_{16}$), mirrored
247.5°	0.5	0° − 337.5°	(F4, $\phi_1 - \phi_{16}$), mirrored

Table A.1: Extension rules of jet interaction

θ_j [deg]	$F_{\max}/T_{\max}$	ϕ [deg] (interval of 22.5°)	sources
270°	1.0	$0° - 337.5°$	(F1, $\phi_1 - \phi_9$), mirrored
270°	0.5	$0° - 337.5°$	(F2, $\phi_1 - \phi_9$), mirrored
292.5°	1.0	$0° - 337.5°$	(F3, $\phi_1 - \phi_{16}$), mirrored
292.5°	0.5	$0° - 337.5°$	(F4, $\phi_1 - \phi_{16}$), mirrored
315°	1.0	$0° - 337.5°$	(F5, $\phi_1 - \phi_9$), mirrored
315°	0.5	$0° - 337.5°$	(F6, $\phi_1 - \phi_9$), mirrored
337.5°	1.0	$0° - 337.5°$	(F3, $\phi_1 - \phi_{16}$), mirrored
337.5°	0.5	$0° - 337.5°$	(F4, $\phi_1 - \phi_{16}$), mirrored
All	0.0	$0° - 337.5°$	(F0, $\phi_1 - \phi_5$), mirrored

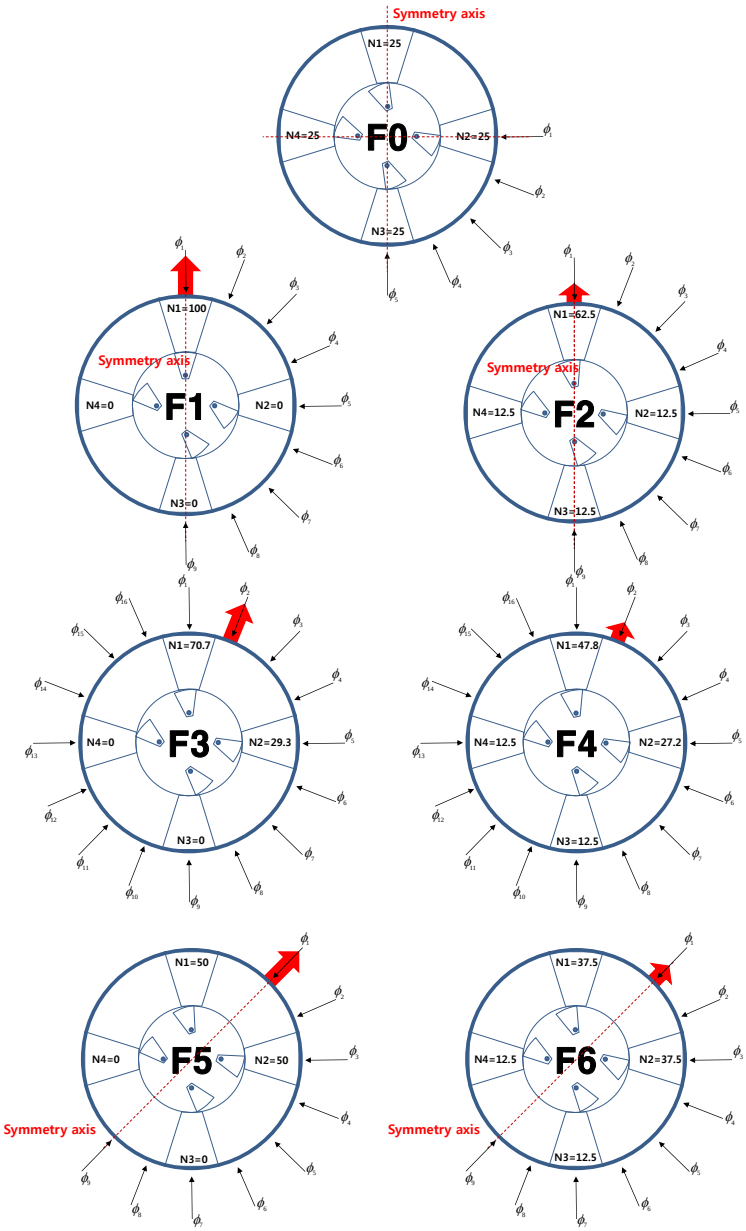

Figure A.1: Roll angle conditions by symmetry relation

Bibliography

[1] P. Champigny and R. Lacau, "Lateral jet control for tactical missiles," *Tiré à part- Office national d'études et de recherches aerospatiales*, 1994.

[2] L. A. Cassel, "Applying jet interaction technology," *Journal of Spacecraft and Rockets*, vol. 40, no. 4, pp. 523–537, 2003.

[3] E. L. Fleeman, *Tactical Missile Design*. AIAA, 2006.

[4] R. Hirokawa, K. Sato, and S. Manabe, "Autopilot design for a missile with reaction-jet using coefficient diagram method," *AIAA Guidance, Navigation, and Control Conference and Exhibit*, no. August, pp. 1–8, 2001.

[5] K. Bibb, G. Brauckmann, E. Walker, and P. Robinson, "Development of the orion crew module static aerodynamic database, part i: Hypersonic," in *29th AIAA Applied Aerodynamics Conference*, p. 3506, 2011.

[6] J. Hanke, "Assessment of computational-fluid-dynamics-based response surface database for ares i supersonic ascent aerodynamics," *Journal of Spacecraft and Rockets*, vol. 49, no. 4, pp. 632–643, 2012.

[7] M. Tomac and A. Rizzi, "Creation of aerodynamic database for the x-31," in *48th AIAA Aerospace Sciences Meeting Including the New Horizons Forum and Aerospace Exposition*, p. 501, 2010.

[8] F. Sourgen, T. Gauthier, F. Leopold, B. Sauerwein, and R. Meuer, "Substitution of hot-gas lateral jets by cold-gas jets in supersonic flows," *Journal of Spacecraft and Rockets*, vol. 48, no. 1, pp. 81–92, 2011.

[9] B. Stahl, H. Emunds, and A. Gülhan, "Experimental investigation of hot and cold side jet interaction with a supersonic cross-flow," *Aerospace Science and Technology*, vol. 13, no. 8, pp. 488–496, 2009.

[10] R. Chamberlain, A. Dang, and D. McClure, "Effect of exhaust chemistry on reaction jet control," in *37th Aerospace Sciences Meeting and Exhibit*, p. 806, 1999.

[11] F. Seiler, P. Gnemmi, H. Ende, M. Schwenzer, and R. Meuer, "Jet interaction at supersonic cross flow conditions," *Shock Waves*, vol. 13, no. 1, pp. 13–23, 2003.

[12] G. Aswin and D. Chakraborty, "Numerical simulation of transverse side jet interaction with supersonic free stream," *Aerospace Science and Technology*, vol. 14, no. 5, pp. 295–301, 2010.

[13] B.-Y. Min, J.-W. Lee, and Y.-H. Byun, "Numerical investigation of the shock interaction effect on the lateral jet controlled missile," *Aerospace science and technology*, vol. 10, no. 5, pp. 385–393, 2006.

[14] M. Kurita, T. Inoue, and Y. Nakamura, "Aerodynamic interaction due to side jet from a blunted cone in hypersonic flow," in *18th Applied Aerodynamics Conference*, p. 4518, 2000.

[15] B. Srivastava and B. Srivastava, "Lateral jet control of a supersonic missile-cfd predictions and comparison to force and moment measurements," in *35th Aerospace Sciences Meeting and Exhibit*, p. 639, 1997.

[16] R. Chamberlain, D. McClure, and A. Dang, "Cfd analysis of lateral jet interaction phenomena for the thaad interceptor," in *38th AIAA Aerospace Sciences Meeting*, pp. 10–13, 2000.

[17] N. V. Queipo, R. T. Haftka, W. Shyy, T. Goel, R. Vaidyanathan, and P. K. Tucker, "Surrogate-based analysis and optimization," *Progress in aerospace sciences*, vol. 41, no. 1, pp. 1–28, 2005.

[18] T. Mackman, C. Allen, M. Ghoreyshi, and K. Badcock, "Comparison of adaptive sampling methods for generation of surrogate aerodynamic models," *AIAA journal*, vol. 51, no. 4, pp. 797–808, 2013.

[19] Y. Kuya, K. Takeda, X. Zhang, and A. I. J. Forrester, "Multifidelity surrogate modeling of experimental and computational aerodynamic data sets," *AIAA journal*, vol. 49, no. 2, pp. 289–298, 2011.

[20] J. Blazek, *Computational fluid dynamics: principles and applications*. Butterworth-Heinemann, 2015.

[21] R. P. Fedkiw, B. Merriman, and S. Osher, "High accuracy numerical methods for thermally perfect gas flows with chemistry," *Journal of Computational Physics*, vol. 132, no. 2, pp. 175–190, 1997.

[22] P. Eliasson, *EDGE: A Navier-Stokes solver for unstructured grids*. FOI, 2001.

[23] P. L. Roe, "Approximate riemann solvers, parameter vectors, and difference schemes," *Journal of computational physics*, vol. 43, no. 2, pp. 357–372, 1981.

[24] S. K. Godunov and V. S. Ryabenkii, *Difference schemes: an introduction to the underlying theory*, vol. 19. Elsevier, 1987.

[25] A. Harten, P. D. Lax, and B. Van Leer, "On upstream differencing and godunov-type schemes for hyperbolic conservation laws," in *Upwind and High-Resolution Schemes*, pp. 53–79, Springer, 1997.

[26] A. Harten and J. M. Hyman, "Self adjusting grid methods for one-dimensional hyperbolic conservation laws," *Journal of computational Physics*, vol. 50, no. 2, pp. 235–269, 1983.

[27] T. Barth and D. Jespersen, "The design and application of upwind schemes on unstructured meshes," in *27th Aerospace sciences meeting*, p. 366, 1989.

[28] A. Jameson, W. Schmidt, and E. Turkel, "Numerical solution of the euler equations by finite volume methods using runge kutta time stepping schemes," in *14th fluid and plasma dynamics conference*, p. 1259, 1981.

[29] F. R. Menter, "Two-equation eddy-viscosity turbulence models for engineering applications," *AIAA journal*, vol. 32, no. 8, pp. 1598–1605, 1994.

[30] F. Menter and C. Rumsey, "Assessment of two-equation turbulence models for transonic flows," in *Fluid Dynamics Conference*, p. 2343, 1994.

[31] D. C. Wilcox, "Reassessment of the scale-determining equation for advanced turbulence models," *AIAA journal*, vol. 26, no. 11, pp. 1299–1310, 1988.

[32] L. A. Cassel, "Applying Jet Interaction Technology," *Journal of Spacecraft and Rockets*, vol. 40, no. 4, 2003.

[33] J. DeSpirito, "Turbulence model effects on cold-gas lateral jet interaction in a supersonic crossflow," *Journal of Spacecraft and Rockets*, vol. 52, no. 3, pp. 836–852, 2015.

[34] V. Viti, R. Neel, and J. A. Schetz, "Detailed flow physics of the supersonic jet interaction flow field," *Physics of Fluids*, vol. 21, no. 4, p. 046101, 2009.

[35] J. Jeong and F. Hussain, "On the identification of a vortex," *Journal of fluid mechanics*, vol. 285, pp. 69–94, 1995.

[36] J. C. Hunt, A. A. Wray, and P. Moin, "Eddies, streams, and convergence zones in turbulent flows," 1988.

[37] A. Ben-Yakar, M. Mungal, and R. Hanson, "Time evolution and mixing characteristics of hydrogen and ethylene transverse jets in supersonic crossflows," *Physics of Fluids*, vol. 18, no. 2, p. 026101, 2006.

[38] J.-M. Zhang, Y. Cui, J. Cui, and H.-S. Sou, "Numerical investigation of lateral jets over a body of revolution in supersonic cross-flow," *Journal of Propulsion and Power*, vol. 28, no. 1, pp. 33–46, 2012.

[39] L. Cortelezzi and A. R. Karagozian, "On the formation of the counter-rotating vortex pair in transverse jets," *Journal of Fluid Mechanics*, vol. 446, pp. 347–373, 2001.

[40] D. Chan, E. Walker, P. Robinson, and T. Wilson, "Modeling powered aerodynamics for the orion launch abort vehicle aerodynamic database (invited)," in *29th AIAA Applied Aerodynamics Conference, Honolulu, HI*, pp. 27–30, 2011.

[41] Y. Kuya, K. Takeda, and X. Zhang, "Optimal surrogate modelling approaches for combining experimental and computational fluid dynamics data sets," in *AIAA Paper 2009-2216*, 2009.

[42] T. W. Simpson, J. Poplinski, P. N. Koch, and J. K. Allen, "Metamodels for computer-based engineering design: survey and recommendations," *Engineering with computers*, vol. 17, no. 2, pp. 129–150, 2001.

[43] T. W. Simpson, J. Poplinski, P. N. Koch, and J. K. Allen, "Metamodels for computer-based engineering design: survey and recommendations," *Engineering with computers*, vol. 17, no. 2, pp. 129–150, 2001.

[44] A. Giunta, S. Wojtkiewicz, and M. Eldred, "Overview of modern design of experiments methods for computational simulations," in *41st Aerospace Sciences Meeting and Exhibit*, p. 649, 2003.

[45] M. D. McKay, R. J. Beckman, and W. J. Conover, "A comparison of three methods for selecting values of input variables in the analysis of output from a computer code," *Technometrics*, vol. 42, no. 1, pp. 55–61, 2000.

[46] A. Forrester, A. Sobester, and A. Keane, *Engineering design via surrogate modelling: a practical guide*. John Wiley & Sons, 2008.

[47] A. I. Forrester and A. J. Keane, "Recent advances in surrogate-based optimization," *Progress in Aerospace Sciences*, vol. 45, no. 1, pp. 50–79, 2009.

[48] S. N. Lophaven, H. B. Nielsen, and J. Søndergaard, "DACE-A Matlab Kriging toolbox, version 2.0," tech. rep., 2002.

[49] A. Vitale, F. Corraro, G. De Matteis, and N. de Divitiis, *Identification from flight data of the aerodynamics of an experimental re-entry vehicle*. InTech, 2012.

[50] R. Jategaonkar, R. Behr, W. Gockel, and C. Zorn, "Data analysis of phoenix reusable launch vehicle demonstrator flight test," *Journal of aircraft*, vol. 43, no. 6, pp. 1732–1737, 2006.

국문초록

연속형 측추력기를 사용하는 유도탄의 초음속 유동에서 제트와 자유류의 상호작용에 의해 발생하는 제트 간섭력(jet interaction)을 전산유체역학을 통한 수치적인 방법을 이용하여 분석하였고, 그 결과를 이용하여 제트 간섭력 데이터베이스(database) 모델링을 수행하였다. 비정렬 격자 기반의 압축성 점성 유동해석 해석자를 이용하여 유동장 해석을 수행하였고, 연속형 측추력기의 제트 간섭력 유동특성 및 자유류 조건, 유도탄의 자세각 변화, 연속형 측추력기의 제트 분사 조건에 따른 제트 간섭력을 분석하였다. 적용된 수치방법은 측추력 제트 간섭력의 수치해석 결과와 풍동시험 결과의 비교를 통하여 검증하였다. 제트 간섭력 데이터베이스의 구축에는 연속형 측추력기의 특성상 많은 계산량이 요구되므로 이를 효율적으로 수행할 수 있는 방법을 모색하였다. 먼저, 일곱개의 제트 운용 조건과 대칭성을 이용하여 설계점을 줄이는 방법을 제안하였으며, 이를 적용하여 수치해석 결과만을 이용한 제트 간섭력 데이터베이스를 구성하였다. 또한 크리깅(Kriging)을 이용한 대체 모델링(surrogate modeling) 방법을 적용하여 보다 적은 계산점으로 효율적으로 제트 간섭력 데이터베이스를 모델링을 수행하였다. 이렇게 구성된 두 제트 간섭력 모델을 비행시험 결과의 비교를 통하여 검증하였으며, 측추력기 운용구간에서 전체 공력계수의 오차가 약 10% 이내로 일치하는 것을 확인하였다. 이러한 분석을 통하여 수치해석 결과만으로 복잡한 제트 간섭력 데이터베이스 모델링이 가능하다는 것을 확인 할 수 있었고, 본 논문의 대체 모델링 방법으로 적정 오차 범위에서 효율적인 데이터베이스 구성이 가능함을 제시하였다.

주요어: 측추력, 연속형 측추력기, 측추력 제어 유도탄, 공력계수 데이터베이스, 공력계수, 제트 간섭력, 전산유체역학, 대체 모델링

학번: 2012-30166